Spring 5-31-2006

Synthesis and characterization of mechanically alloyed aluminum-based compounds as high energy density materials

Xiaoying Zhu

New Jersey Institute of Technology

Recommended Citation

Zhu, Xiaoying, "Synthesis and characterization of mechanically alloyed aluminum-based compounds as high energy density materials" (2006). *Dissertations*. 785.
https://digitalcommons.njit.edu/dissertations/785

ABSTRACT

SYNTHESIS AND CHARACTERIZATION OF MECHANICALLY ALLOYED ALUMINUM-BASED COMPOUNDS AS HIGH ENERGY DENSITY MATERIALS

by
Xiaoying Zhu

A new type of metastable reactive powders for potential use as high energy density materials in propellants, explosives, and pyrotechnics was developed. These powders are intended to replace aluminum typically added to energetic formulations to increase reaction enthalpy and temperature. The new materials are metastable aluminum-based alloys, which enable achievement of substantially reduced ignition temperatures and accelerated bulk burn rates compared to aluminum. Titanium and lithium were used as alloying components. The materials properties and characteristics leading to their enhanced combustion performance were investigated. The powders were prepared using mechanical alloying and characterized using X-Ray Diffraction (XRD), Scanning Electron Microscopy with Energy Dispersive X-ray spectrometer (SEM/EDX), and thermal analysis. Detailed ignition measurements were performed to identify the processes affecting ignition for the prepared metastable powders.

Al–Ti alloys were prepared with compositions ranging from $Al_{0.95}Ti_{0.05}$ to $Al_{0.75}Ti_{0.25}$. Mechanically alloyed powders comprised solid solution of Ti and Al. Upon their heating, a number of subsolidus exothermic transitions were detected and assigned to formation of different modifications of Al_3Ti. For alloys with 20 at-% or less of Ti, an endothermic transition was observed around 1170 K, which was assigned to the formation of aluminum and titanium carbides with the carbon impurities coming from the stearic acid added to the mechanically alloyed powders as a process control agent. Three distinguishable oxidation steps were observed

for the prepared alloys. The products formed at different oxidation stages were quantitatively analyzed by XRD. While Al_2O_3 and TiO_2 were the main oxidation products, the stepwise oxidation was related to phase transitions of the alumina oxide scale. Ignition of mechanically alloyed Al–Ti powders was investigated experimentally for heating rates ranging from $3 \times 10^3 - 2 \times 10^4\, K/s$. It was shown that ignition was triggered by the exothermic formation of a metastable $L1_2$ phase of Al_3Ti . This conclusion was confirmed by additional ignition experiments in which annealed mechanical alloys already containing this transition Al_3Ti phase were used. The annealed alloys did not ignite in the same temperature range as freshly prepared metastable alloys.

Al–Li alloys were synthesized with a fixed bulk composition of $Al_{0.7}Li_{0.3}$. At short milling times, an intermetallic LiAl δ -phase was readily produced. At longer milling times, the LiAl phase disappears and a solid solution of Li in Al (α-phase) formed with as much as 10 at-% of dissolved Li. Continuing milling resulted in the production of a uniform, x-ray amorphous phase. Kinetics of the exothermic processes of metastable relaxation in Al–Li alloys observed in thermal analysis was not found to directly correlate with the ignition kinetics. It was proposed that ignition in the prepared alloys was driven by selective oxidation of Li, with its rate being affected by the phase transformations occurring in the alloy upon its heating and diffusion of oxygen through Al_2O_3 films.

Ignition delays were substantially reduced for both prepared mechanically alloyed powders as compared to pure aluminum. Therefore, the developed materials can replace aluminum as an additive to energetic formulations for a number of practical applications.

SYNTHESIS AND CHARACTERIZATION OF MECHANICALLY ALLOYED ALUMINUM-BASED COMPOUNDS AS HIGH ENERGY DENSITY MATERIALS

by

Xiaoying Zhu

A Dissertation
Submitted to the Faculty of
New Jersey Institute of Technology
in Partial Fulfillment of the Requirements for the Degree of
Doctor of Philosophy in Mechanical Engineering

Department of Mechanical Engineering

May 2006

APPROVAL PAGE

SYNTHESIS AND CHARACTERIZATION OF MECHANICALLY ALLOYED ALUMINUM-BASED COMPOUNDS AS HIGH ENERGY DENSITY MATERIALS

Xiaoying Zhu

Dr. Edward L. Dreizin, Dissertation Advisor — Date
Professor of Mechanical Engineering, NJIT

Dr. Ronald W. Smith, Committee Member — Date
President, Materials Resources International

Dr. Boris Khusid, Committee Member — Date
Professor of Mechanical Engineering, NJIT

Dr. Rajesh N. Dave, Committee Member — Date
Professor of Mechanical Engineering, NJIT

Dr. Mirko Schoenitz, Committee Member — Date
Assistant Research Professor of Mechanical Engineering, NJIT

BIOGRAPHICAL SKETCH

Author: Xiaoying Zhu

Degree: Doctor of Philosophy

Date: May 2006

Undergraduate and Graduate Education:

- Doctor of Philosophy in Mechanical Engineering,
  New Jersey Institute of Technology, Newark, NJ, USA 2006
- Master of Science in Computer Science,
  New Jersey Institute of Technology, Newark, NJ, 2001
- Master of Science in Materials Science,
  Wuhan University of Technology, Wuhan, P. R. China, 1992
- Bachelor of Science in Materials Science,
  Wuhan University of Technology, Wuhan, P. R. China, 1984

Major: Mechanical Engineering

Presentations and Publications:

X. Zhu, M. Schoenitz, and E. L. Dreizin, "Oxidation Behavior of Mechanical Alloyed Al Rich Al–Ti Powders," *Oxidation of Metals*, (under review 2005-2006)

X. Zhu, M. Schoenitz, and E. L. Dreizin, "Mechanical Alloyed Aluminum-Lithium Powders," *Journal of Alloys and Compounds*, (under review 2006)

X. Zhu, M. Schoenitz, and E.L. Dreizin, "Oxidation Processes and Phase Changes in Metastable Al-Ti Mechanical Alloys," *Materials Research Society Proceedings*, vol. 800, pp. AA3.4.1–AA3.4.6, Boston,MA. Dec. 1 - 5, 2003.

X. Zhu, M. Schoenitz, V. K. Hoffmann and E. L. Dreizin, "Reactive Al–Li Powders Prepared by Mechanical Alloying," *Materials Research Society Proceedings*, Boston, MA. Nov. 27 - 31, 2005. (in press).

X. Zhu, M. Schoenitz, and E. L. Dreizin, "Reactions in Nano-composite Al-CuO Thermite Powders Synthesized by Arrested Reactive Milling," , presented in Joint Meeting of the U.S. Section of the Combustion Institute, Philadelphia, PA. March 20-23, 2005

M. Schoenitz, X. Zhu, and E.L. Dreizin, "Carbide Formation in Al-Ti Mechanical Alloys," *Scripta Materialia*, vol. 53, no. 9, pp. 1095–1099, 2005.

M. Schoenitz, X. Zhu, and E.L. Dreizin, "Mechanical Alloys in the Al-rich Part of the Al-Ti Binary System," *Journal of Metastable and Nanocrystalline Materials*, vol. 20-21, pp. 455-461, 2004.

Y. L. Shoshin, M. A. Trunov, X. Zhu, M. Schoenitz and E. L. Dreizin, "Ignition of Aluminum-Rich Al–Ti Mechanical Alloys in Air," *Combustion and Flame*, vol. 144, no. 4, pp. 688–697, 2006.

M. A. Trunov, M. Schoenitz, X. Zhu, and E. L. Dreizin, "Effect of Polymorphic Phase Transformations In Al_2O_3 Film on Oxidation Kinetics of Aluminum Powders," *Combustion and Flame*, vol. 140, no. 4, pp. 310–318, 2005.

To my parents, especially to my father, who passed
away during this period of time. To my parents-in-law,
who are taking care my son with their deepest love
through the whole my PhD program.

ACKNOWLEDGMENT

I would like to express my deepest appreciation to Dr. Edward L. Dreizin, who not only served as my research supervisor, providing valuable and countless resources, insight, and intuition, but also constantly gave me support, encouragement, and reassurance. I acknowledge all the invaluable help from Dr. Mirko Schoenitz who is not only served as my committee member, but also has been a thoughtful co-worker and co-author. Special thanks are given to Drs. Rajesh N. Dave, Ronald W. Smith, and Boris Khusid for active participation in my committee. Truthful thanks are sincerely given to Dr. Ronald Kane and Mrs. Clarisa Gonzalez for their instructions on all formatting issues for this dissertation.

Many of my fellow graduate students in the Energetic Materials Research Laboratory are deserving of recognition for their support. I also wish to thank Dr. Mikhaylo Aleksiyovych Trunov for his inspired suggestions and discussions.

Finally, I would like to thank my husband, Dejiang Jin, who keeps giving me all kinds of support whenever I need it.

TABLE OF CONTENTS

TABLE OF CONTENTS
(Continued)

TABLE OF CONTENTS
(Continued)

TABLE OF CONTENTS
(Continued)

Chapter **Page**

TABLE OF CONTENTS
(Continued)

LIST OF TABLES

LIST OF FIGURES

LIST OF FIGURES
(Continued)

LIST OF FIGURES
(Continued)

Figure **Page**

LIST OF FIGURES
(Continued)

LIST OF FIGURES
(Continued)

CHAPTER 1

INTRODUCTION

1.1 Background

Metal powders are used as additives in propellants, explosives, and pyrotechnics [1–6]. During combustion of metal particles specific phenomena have been observed, such as temperature jumps, oscillatory burning, jetting, and particle disruption. Past research showed that phase transitions occurring in burning metals cause these events [7–13]. Aluminum particles, for example show asymmetric burning, and temperature oscillations during combustion. This is illustrated in Figure 1.1.

This behavior can be explained by the existence of a liquid aluminum-oxygen solid solution at high temperatures as predicted by the Al-O equilibrium phase diagram [14, 15].

The relevance of equilibrium phase relations and phase transitions to combustion has led to the hypothesis that structure and composition of metals can be modified in advance to prepare metastable materials. This could enable one to program phase transitions so that the resulting reactions in particle combustion occur earlier and in a well-controlled fashion.

1.2 Selection of Materials

Aluminum is the most widely used high energy density material (HEDM) for application in propellants for space exploration and military systems, such as missiles and pressure generators [16–20]. It has very high combustion enthalpy, very low cost of manufacture, and is non-toxic. Therefore, the present research focuses on Al-based materials. A number of issues should be addressed to improve aluminum

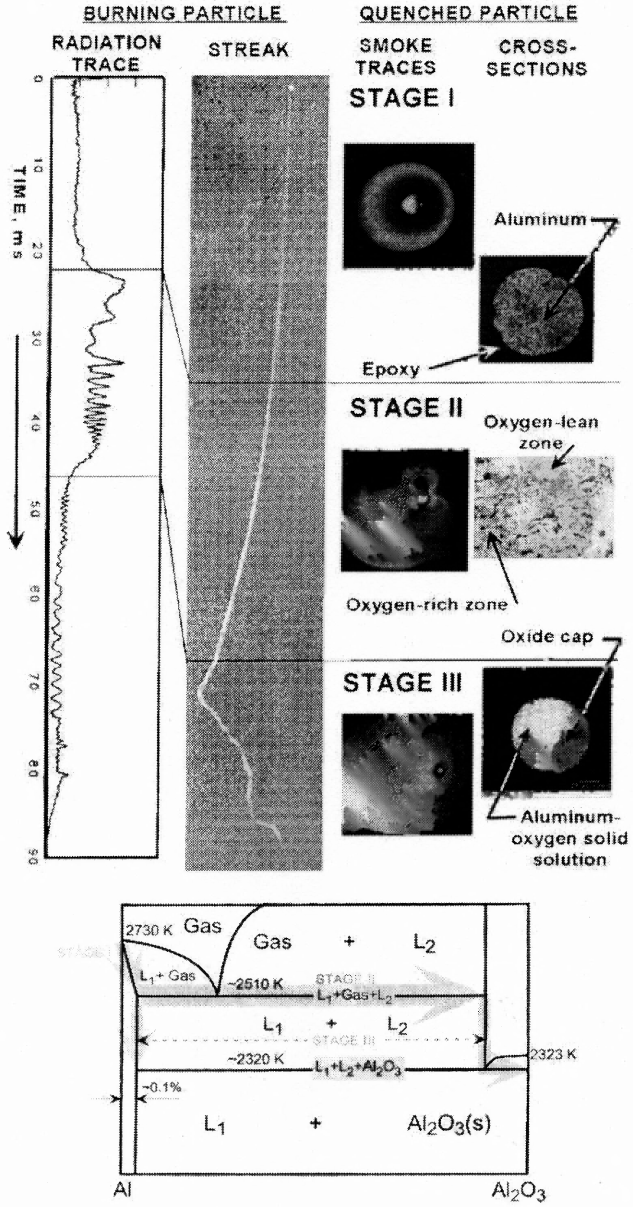

Figure 1.1 Upper: Trace of burning Al particle. Particles quenched at various stages are also shown [13]. Lower: Al-O phase diagram illustrating the path a burning particle follows, and involved invariant points [14, 15].

combustion [21–25]. Mainly due to a passivating surface layer of Al_2O_3 the oxidation is slow and ignition delays are long. Particles coalesce prior to ignition, oxide caps form during combustion, and particles often extinguish before all the metal is oxidized [26–31].

Table 1.1 Properties of Al and Some Alloying Elements

Element	Al	Mg	Li	Ti	Zr
D [g/cm^3]	2.7	1.74	0.535	4.51	6.51
ΔH_{ox} [kJ/g]	-31.05	-24.74	-86.26	-19.61	-12.03

To address these problems, stable and metastable alloys can be used that combine the properties of the components to benefit ignition and combustion. Table 1.1 lists examples of elements used as additives in Al-based alloys.

1.3 Preliminary Results

One of the first intermetallic systems investigated for combustion applications was the binary system Al-Mg. Early combustion experiments using thermodynamically stable, commercial Al-Mg alloys have been reported in the literature [32], however no coherent picture regarding their combustion mechanism has emerged. Higher rates of flame propagation have been observed recently for aerosols of metastable supersaturated solid solutions (mechanical alloys) of Mg in Al, compared to the rates of flame propagation for aluminum and even magnesium aerosols with the same particle size [33]. Rates of pressure rise in constant volume explosion experiments were higher for mechanical alloys than for powder mixtures with identical bulk composition, or for powders of thermodynamically stable alloys [34]. These results are shown in Figure 1.2.

The ignition temperatures of Al-Mg mechanical alloys were found to be much lower than that of pure Al, even at Mg concentrations as low as 5 at-% [35]. The phase changes occurring during heating of the mechanically alloyed supersaturated solid Al–Mg solutions were investigated in Ref [36]. It was found that these mechanical alloys undergo a number of subsolidus phase transitions associated with the formation

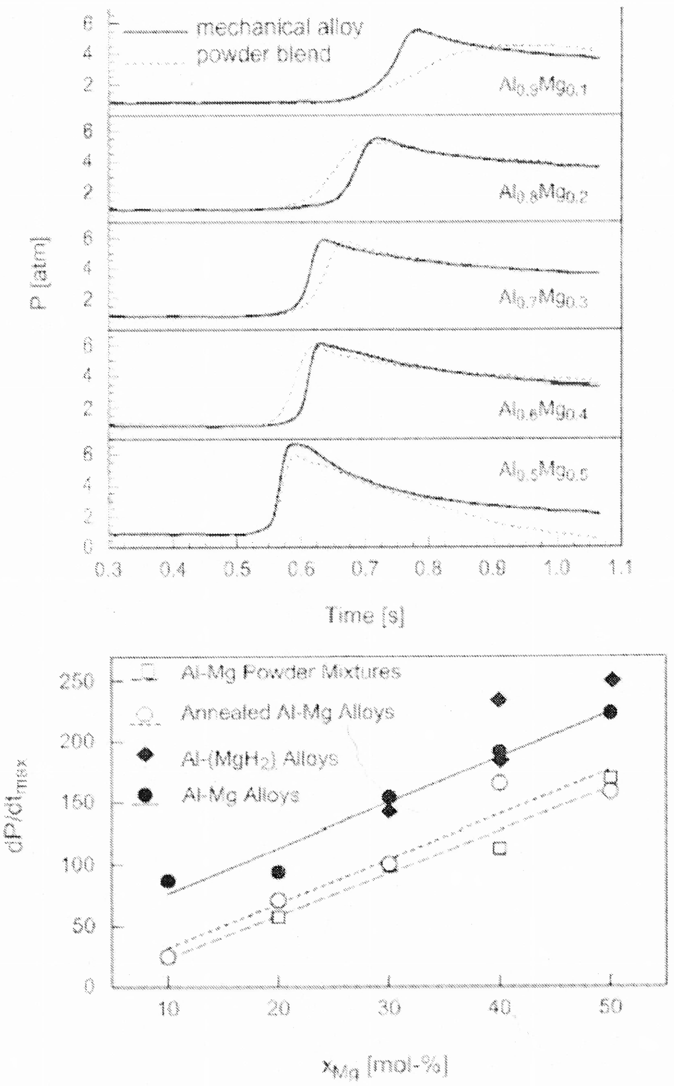

Figure 1.2 Results of combustion tests for various elements and alloys [34].

of equilibrium intermetallic phases (at temperatures below the eutectic melting point of 723 K). Most of these phase transitions are exothermic and could play a role in accelerating ignition of the mechanically alloy particles. The binary system Al-Ti was also investigated. Titanium is of particular interest as a component to increase the density of metallic fuel additives, and thus the specific impulse of the respective propellants. Recent observations suggest that ignition and combustion of aerosols of Al-Ti mechanical alloys are enhanced compared to equilibrium alloys or blends of elemental powders [37].

A detailed characterization of phase relations and the degree of metastability in metastable Al–Ti mechanical alloys is needed to optimize their performance as advanced energetics. This information is also necessary to model processes of combustion of metallic fuel particles, specifically to quantitatively predict ignition behavior as a function of heating rate and of the particles' environment [38].

1.4 Project Objectives

The purpose of the present research is to develop a new class of reactive Al-based alloys. Metastable materials, in which the relaxation reaction could trigger ignition are of particular interest. The work will include synthesis and characterization of mechanical alloys in the Al-based systems with the specific goal to optimize these materials for combustion applications. It is further proposed to address issues leading to the large-scale production of such materials.

In order to relate the relaxation processes in mechanical alloys to ignition and combustion behavior, their metastability must be characterized, and the relaxation processes leading to equilibrium phases must be described. Dependence of the equilibration processes on bulk composition needs to be known in order to design mechanically alloyed powders for specific energetic applications. Because the materials of interest are new, detailed characterization of the produced phases is necessary, in order to understand the relaxation and reaction mechanisms.

This research begins with Al–Ti system, synthesizing, characterizing and establishing phase relations and the degree of metastability in metastable Al–Ti alloys with the specific goal to optimize materials for combustion applications and to address issues arising for large-scale production.

Mechanical alloying requires some kind of process control agent to balance particle fracturing and cold-welding. Organic chemicals such as stearic acid ($CH_3 - (CH_2)_{16} - COOH$) are frequently being used. When this additive gradually deteriorates during prolonged milling, a certain degree of carbon contamination of the mechanical alloy will occur. As part of that specific investigation to describe the effect in Al-Ti system, a systematic study of relationship in between is presented.

Understanding the oxidation mechanisms and kinetics of the alloy powders at elevated temperatures is essential for modeling their performance in energetic applications. At the same time, oxidation mechanisms are critical for stability of such alloys during their storage and handling. The stability of alloys is also important for structural applications, where oxidation and corrosion need to be minimized. Ideally it should be possible to control oxidation rates by adjusting process parameters of the mechanical alloying synthesis and the alloy composition. Thus, the investigation of the oxidation mechanisms in aluminum-rich Al–Ti alloys prepared by MA will logically be followed up. It is also of interest to compare the oxidation mechanisms of powders of Al-rich Al–Ti alloys with those of pure aluminum powders. The background of the research presented here necessitates the work with powders as opposed to consolidated bulk alloys. It is expected that the results will be sufficiently general to be useful for insights in the oxidation of consolidated bulk alloys. In the part of this work, the oxidation behavior is studied for a set of mechanically alloyed Al-rich Al–Ti powders with varied compositions.

For all kinds of energetic material applications, the ignition of specific material is the initial step which leads to combustion, so that after investigating the oxidation behavior, the next big issue will be whether it is possible to identify the process governing ignition of the aluminum-rich Al–Ti mechanical alloys. The ignition in practical systems usually occurs at very high particle heating rates (e.g.,

$10^3 - 10^6 K/s$) that exceed by far the typical heating rates of thermal analysis ($< 100 K/min$). Therefore, the objective of this part of the work will be to study the kinetics of ignition of the Al–Ti mechanical alloys directly and compare the results to the kinetics of the phase transitions and oxidation steps identified earlier by thermal analysis. Specifically, it is of interest to establish which of the phase transformations occurring in Al–Ti mechanical alloys upon heating would affect their ignition.

This research continues with Al–Li system, despite substantial interest in Al-Li alloys as additives to energetic materials, relatively little is known about the mechanisms of their ignition and combustion. One of the principal reasons for this is that Al–Li alloys with the lithium concentrations exceeding several percents, which would be of practical interest to combustion applications, are not readily available.

The methodologies, which was developed in Al–Ti system, have been applied to Al–Li system. Synthesizing, characterizing and establishing phase relations and the degree of metastability in metastable Al-Li alloys have been conducted with the goal to understand changes in the structure and phase make-up occurring in the alloys upon their heating.

CHAPTER 2

TECHNICAL APPROACH

2.1 Overview

Figure 2.1 shows the outline of the current project. After the initial selection of the type of alloy under investigation, synthesis and systematic characterization follow. Results of the characterization step are being used to improve synthesis condition in an iterative fashion. Combustion testing completes the procedure. Synthesis and characterization are described in greater detail below.

2.2 Synthesis: Mechanical Alloying

Metastable intermetallic materials are readily produced by mechanical alloying (MA). MA, a non-equilibrium powder metallurgical method to prepare highly metastable materials was developed by a number of groups [39–41], and has since found wide application for the production of structural (e.g. oxide dispersion hardened) materials, or mechanically activated materials with increased reactivity. An extensive review of the technique was given recently by Suryanarayana [42].

Mechanical alloying is essentially high-energy ball milling of metal powders in the presence of process control agents (PCA). For all synthesis experiments, a SPEX 8000 shaker mill (see Figure 2.2) and a planetary ball mill (Retsch PM400) were used.

Mechanical alloying is sensitive to a set of process parameters such as the degree of filling of the milling vials, the size and size distribution of the milling medium, and the amount of process control agents (PCA) that balances cold-welding against fracturing and grinding. An overview is given in Table 2.1.

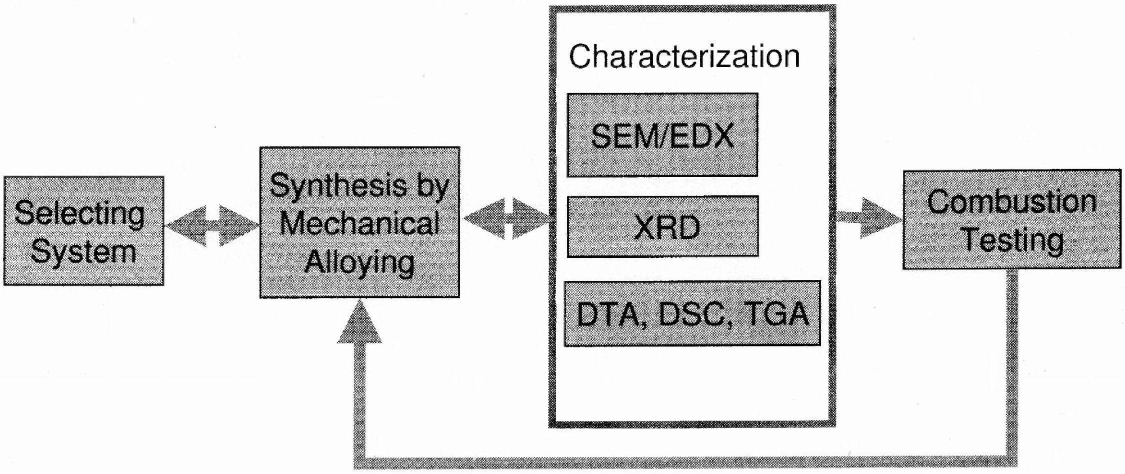

Figure 2.1 Organization chart of the current project.

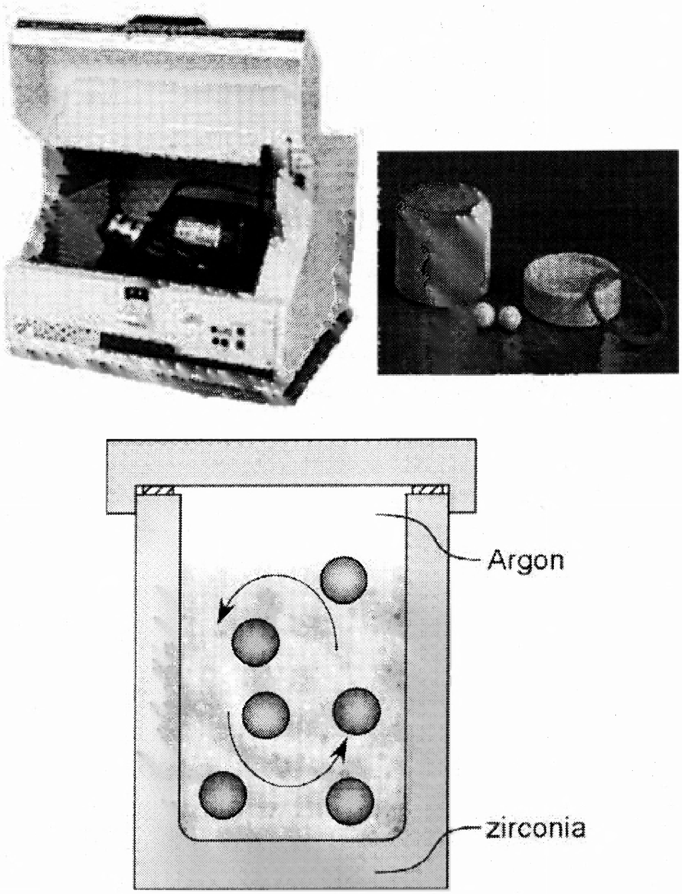

Figure 2.2 SPEX 8000 shaker mill with ZrO_2 vial and balls.

Table 2.1 Process Parameters of Mechanical Alloying

Parameter	Effect on milling process and product	Typical range for materials explored in this project
Milling time	Particle size refinement increases with milling time	5 min - 15 hours
Type and frequency of motion of the milling vessel	Affects milling energy	Rotation, oscillation 1000 RPM (currently unmodified)
Use of a process control agent (PCA)	Controls balance between fracturing and cold-welding of powder particles	None, or stearic acid at levels of 2 -4 wt-%
Ball diameter	Affects size distribution of product powder	2 mm – 10 mm
Ball material	Relates to ball mass and affects milling energy	Steel, YSZ
Ball-to-powder mass ratio (BPR)	Affects milling energy	2 - 10
Total powder mass	Affects milling energy	1 g - 10 g
Particle size of starting powders	Affects texture of Arrested Reactive Milling produced nano-composites	$1 - 100\,\mu$m
Process temperature	Controls maximum achievable metastability of the product	Ambient (currently uncontrolled)
Atmosphere	Prevents or controls partial oxidation	Argon, vacuum, air

* a) Stearic acid was selected based on its previous extensive use in mechanical alloying [42].

* b) Optimum parameters depend on the type of mill used – the values shown here are for the shaker mill used in the current research (SPEX 8000D), and are shown mainly for illustrative purposes.

2.3 Materials Characterization

The techniques described below are the basis for the characterizations of materials synthesized in this research.

2.3.1 Scanning Electron Microscopy (SEM)

SEM complements optical microscopy for studying the texture, topography and surface features of powders or solid pieces; objects from tens of nanometers up to millimeter size can be seen and, because of the depth of focus of SEM instruments, the resulting pictures have a definite three-dimensional quality. Another advantage of SEM is the reflection design, so special methods of sample preparation are not required comparing with TEM (Transmission Electron Microscope). Microscopy is readily combined with specially resolved elemental analysis using energy dispersive X-ray spectrometer (EDX).

2.3.2 Powder X-ray Diffraction (XRD)

In powder diffraction methods a monochromatic beam of X-rays strikes a finely powdered sample that, ideally, has crystals randomly arranged in every possible orientation. In such a powder sample, the various lattice planes are therefore also present in every possible orientation. For such a set of planes, therefore, at least some crystals must be oriented to fulfill the diffraction condition. The diffracted beams are detected and collected. Each crystalline phase has a characteristic powder pattern, which can be used as a fingerprint for identification purposes. The most important use of the powder method is in the qualitative identification of crystalline phases or compounds.

2.3.3 Thermal Analysis

Thermal analysis may be defined as the measurement of physical and chemical properties of materials as a function of temperature. Most usefully kinds of solid are 'thermally active' in one way or another and may be profitably studied by thermal analysis. The two main thermal analysis techniques are thermogravimetry (TG), which records the change in weight of a sample as a function of either temperature or time, and differential thermal analysis (DTA), which measures the difference in temperature, ΔT, between a sample and an inert reference materials as a function of temperature; DTA therefore detects changes in the heat content. A technique that is closely related to DTA is differential scanning calorimetry (DSC). In DSC, the equipment is designed to allow a quantitative measurement of the enthalpy changes that occur in a sample as a function of either temperature or time.

2.3.4 Ignition and Combustion Studies

Intended applications of the materials under development are in reactive compositions, solid propellants, explosives, and pyrotechnics. Therefore initial performance assessments are made using several laboratory ignition and combustion experiments. Optical diagnostics are used to characterize ignition temperatures at different heating rates approaching the rates observed in practical applications. Flames of the produced aerosolized powders are also studied optically. In addition combustion products are collected and analyzed.

CHAPTER 3

MECHANICAL ALLOYS IN THE ALUMINUM-RICH PART OF THE ALUMINUM–TITANIUM BINARY SYSTEM

3.1 Introduction

Metals with high volumetric and gravimetric combustion enthalpies are of interest as materials with high energy densities. Aluminum in particular and aluminum-based alloys have been investigated as additives in various fuel formulations for propellants, explosives, incendiaries or pyrotechnics [1,32,43]. Practical applications are limited, however, since chiefly kinetic obstacles such as long ignition delays and slow burning rates prevent the theoretical combustion enthalpies from being fully exploited. Based on recent research [13] that linked internal phase transformations to macroscopic events during combustion of metal particles, interest in metastable intermetallic materials has developed. The first material system to be studied in this work was mechanical alloys in the aluminum–titanium binary system with titanium concentrations of less than 25 at-%. Titanium is of particular interest as a component to increase the density of metallic fuel additives, and thus increase the specific impulse of the respective propellants. Recent observations suggest that ignition and combustion of aerosols of Al–Ti mechanical alloys are enhanced compared to equilibrium alloys or blends of elemental powders [37].

A detailed characterization of phase relations and the degree of metastability in metastable Al–Ti alloys is needed to attempt performance optimization of these materials as advanced energetics. This information is also necessary to model processes of combustion of metallic fuel particles, specifically to quantitatively predict ignition behavior as a function of heating rate and of the particles' environment [38].

A number of experimental and theoretical studies on mechanical alloying of Al_3Ti have been published. Less information is available on Al-Al_3Ti composites with compositions close to pure Al. Equilibrium phases in this region of the system include the α-Al phase with *fcc* structure and low- and high-temperature modifications of Al_3Ti ($D0_{23}$ below 1008 K, and $D0_{22}$ above) [44]. In addition, a metastable phase with $L1_2$ structure has been reported for Al_3Ti [44]. References disagree however about whether the $D0_{23}$ phase is a stable phase in the system. Lattice dynamic calculations give the energy differences indicating relative stability of the Al_3Ti phases as $D0_{22} < D0_{23} < L1_2$, showing therefore the $D0_{22}$ phase as the most stable even at low temperatures [45]. Experimentally, it was found that the $D0_{22}$ phase, when mechanically milled at ambient conditions deteriorates, and transforms first to the $D0_{23}$ phase and eventually to the $L1_2$ phase, supporting the sequence of relative stability [46]. The same study concluded that the $D0_{23}$ and $L1_2$ structures form via the formation of antiphase boundaries, causing a loss of long range order, and that the energetic differences are compensated by the arising configurational entropy in the increasingly disordered phases.

Mechanical alloying of Al and Ti powders with Al_3Ti bulk composition leads to the formation of a *fcc* phase with lattice dimensions close to the $L1_2$ structure [47]. Re-equilibration of this material was shown by thermal analysis to result in the formation of the $L1_2$ (at 638 K), $D0_{23}$ (at 727 K) and $D0_{22}$ (at 910 K) phases [47]. A preliminary study investigating mechanical alloys in the Al-Al_3Ti compositional range and limited to temperatures below 873 K, essentially confirmed this transformation sequence for all compositions [48].

In order to relate the re-equilibration processes in mechanical alloys to ignition and combustion behavior, their stability must be characterized as a function of temperature, and the relaxation process must be described until equilibrium is achieved. Dependence of the equilibration processes in bulk compositions need to be known in order to design mechanically alloyed powders for specific energetic requirements.

3.2 Experimental

The mechanical alloys were prepared in a SPEX 8000 shaker mill. Starting materials were elemental powders of Al (Alfa Aesar, 99.8%, -40 +325 mesh) and Ti (Alfa Aesar, 99%, -325 mesh). Optimum milling parameters required to achieve a stationary state in a minimum amount of time were determined in a series of separate experiments before actual sample preparation was begun. For synthesis, 5 g of initially unmixed metal powder were milled in zirconia vials under argon atmosphere with 2 wt-% of stearic acid ($CH_3 - (CH_2)_{16} - COOH$, Fluka, 99%) added as PCA. Zirconia balls of 10 mm diameter and a total mass of 50 g were used as milling medium, giving a ball-to-powder weight ratio (BPR) of 10. Samples were milled for a total time of 15 hours each, the time after which the mechanical alloy with $Al_{0.75}Ti_{0.25}$ composition showed no further structural or compositional changes.

The sample temperature rose up to 323 – 333 K during milling. Moderate sample caking posed a problem for milling effectiveness; milling for extended periods also limits the useful lifetime of the mill. Therefore, milling was carried out in intervals of 180 min, after which the mill was allowed to cool to room temperature, and caked samples, if present, were manually broken apart in a glove box under protective Ar atmosphere.

Morphology and compositional homogeneity of the mechanical alloys were examined on a LEO 1530 Field Emission Scanning Electron Microscope (FE-SEM). The SEM is equipped with a energy dispersive X-ray spectrometer (EDX) that allows standardless compositional analysis with a maximum spatial resolution of approximately 0.1 μm.

Structure and phase makeup was determined for each mechanical alloy by X-ray powder diffraction (XRD) on a Bragg-Brentano type Phillips X'pert MRD diffractometer operated at 45 kV and 40 mA, using Cu-Kα radiation ($\lambda = 1.5438$ Å).

Temperature dependent structural transformations were observed by differential scanning calorimetry (DSC) using a Netzsch Simultaneous Thermal Analyzer STA409-PC. Samples were contained in alumina sample pans. The furnace of the STA409-PC was evacuated to approximately 0.3 bar and back-filled with Ar (Matheson, ultrahigh purity) three times before each measurement. During measurements, the furnace was continuously flushed with Ar at approximately 10 ml/min. DSC traces were recorded at a heating rate of 15 K/min. Low-temperature scans (< 873 K) were baseline corrected using a repeat heating of the equilibrated sample.

The back-transformation of the mechanical alloys to thermodynamically stable set of phases occurred over a wide temperature range. To relate events observed by DSC to structural transitions, DSC runs were interrupted at intermediate temperatures, and XRD patterns of these partially relaxed mechanical alloys were collected. The effective quench rates achieved in these experiments were relatively low — about $20 - 30\,K/min$. No strict temperature control at the end of a heating cycle is possible in the DSC apparatus that was used, therefore the targeted temperatures were likely to be overshot by as much as $10 - 20\,°$C. Nevertheless, the samples phase recovery proved instructive by identifying intermediate transition products.

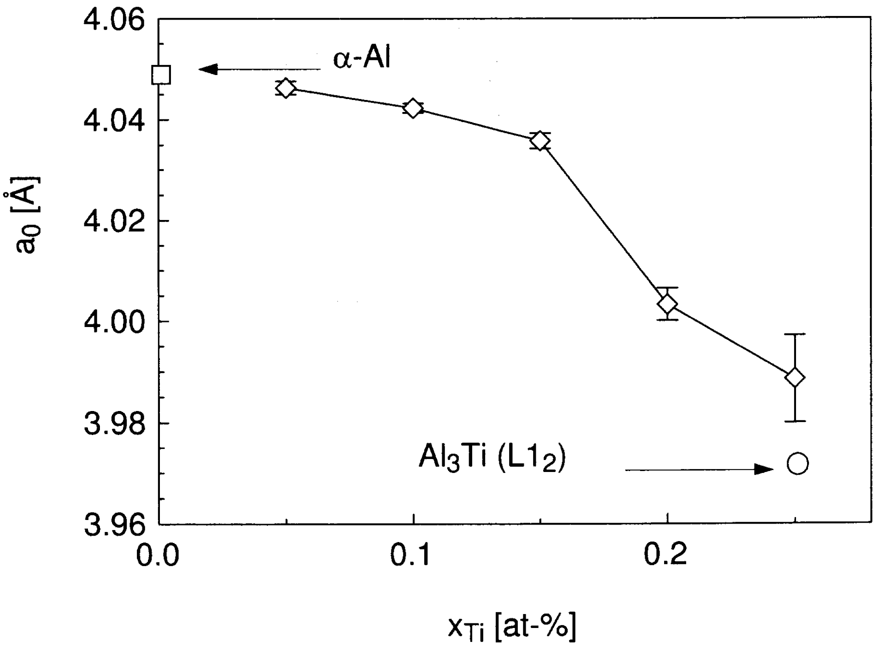

Figure 3.1 Lattice parameter of the *fcc* phase observed in as-milled mechanical alloys.

3.3 Results

SEM analysis of polished sections of the as-milled mechanical alloys showed them to be chemically homogeneous within the resolution limit of the instrument, ~ 10 nm. Only the bulk composition could be measured by EDX. XRD patterns showed only peaks consistent with an *fcc* phase with lattice dimensions similar to α-Al. Diffraction peaks became wider and weaker with increasing Ti concentration. The apparent lattice parameter vs. Ti concentration is shown in Figure 3.1. The lattice parameter gradually decreases from the value for pure α-Al (4.049 Å [49]) with increasing Ti concentration up to 15 at-% Ti. The mechanical alloys with 20 and 25 at-% Ti deviate more strongly from pure α-Al with a lattice parameter closer to that of the $L1_2$ phase of Al_3Ti (3.972 Å [44]).

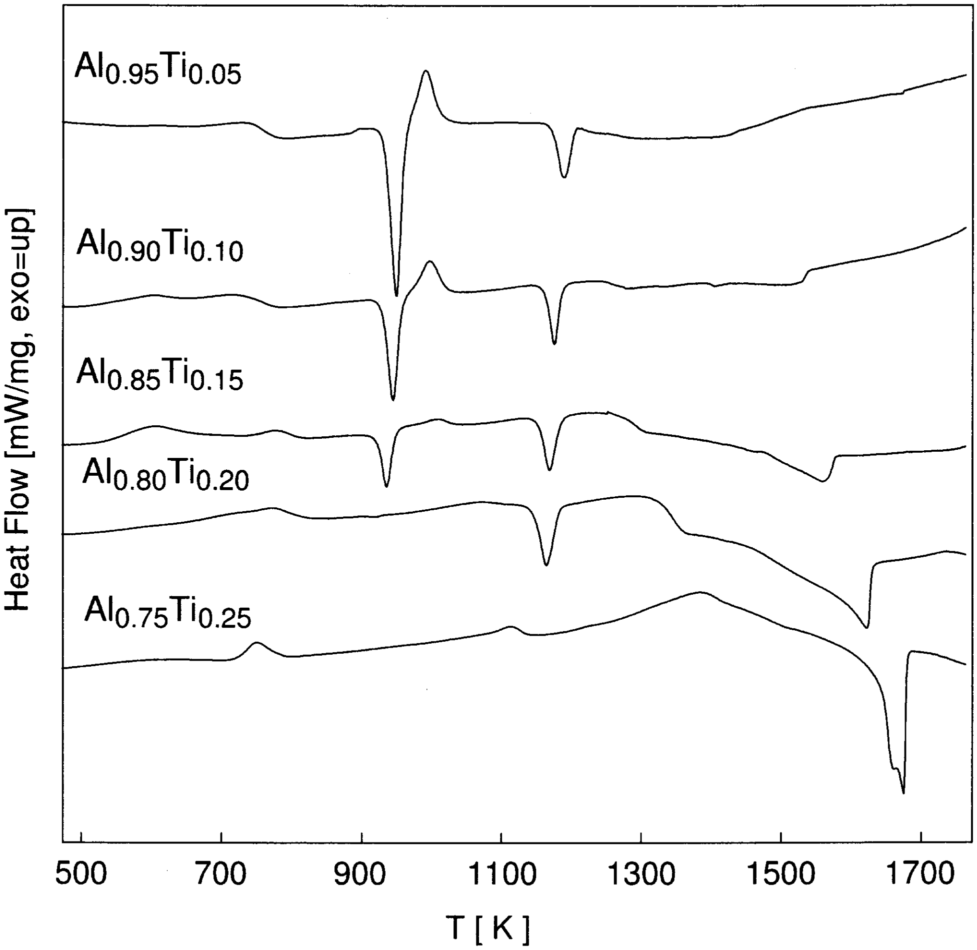

Figure 3.2 DSC traces of Al–Ti mechanical alloys (15 *K/min*; $T_{max} = 1773\,K$).

Figure 3.2 shows the DSC traces of all mechanical alloys up to a maximum temperature of 1773 K. A number of exothermic peaks is observed below 873 K. Melting of Al is observed at 933 K except for $Al_{0.80}Ti_{0.20}$ and $Al_{0.75}Ti_{0.25}$. At high temperatures (1473 – 1673 K), endothermic peaks correspond to the liquidus of each respective bulk composition. An exothermic peak near 1023 K is present in $Al_{0.95}Ti_{0.05}$ and decreases in intensity with increasing Ti concentration. A further endothermic peak near 1173 K is observed for all compositions except $Al_{0.75}Ti_{0.25}$.

To elucidate the nature of the endothermic peak near 1173 K, the $Al_{0.85}Ti_{0.15}$ mechanical alloy was heated repeatedly between 873 K and 1223 K at 15 *K/min*.

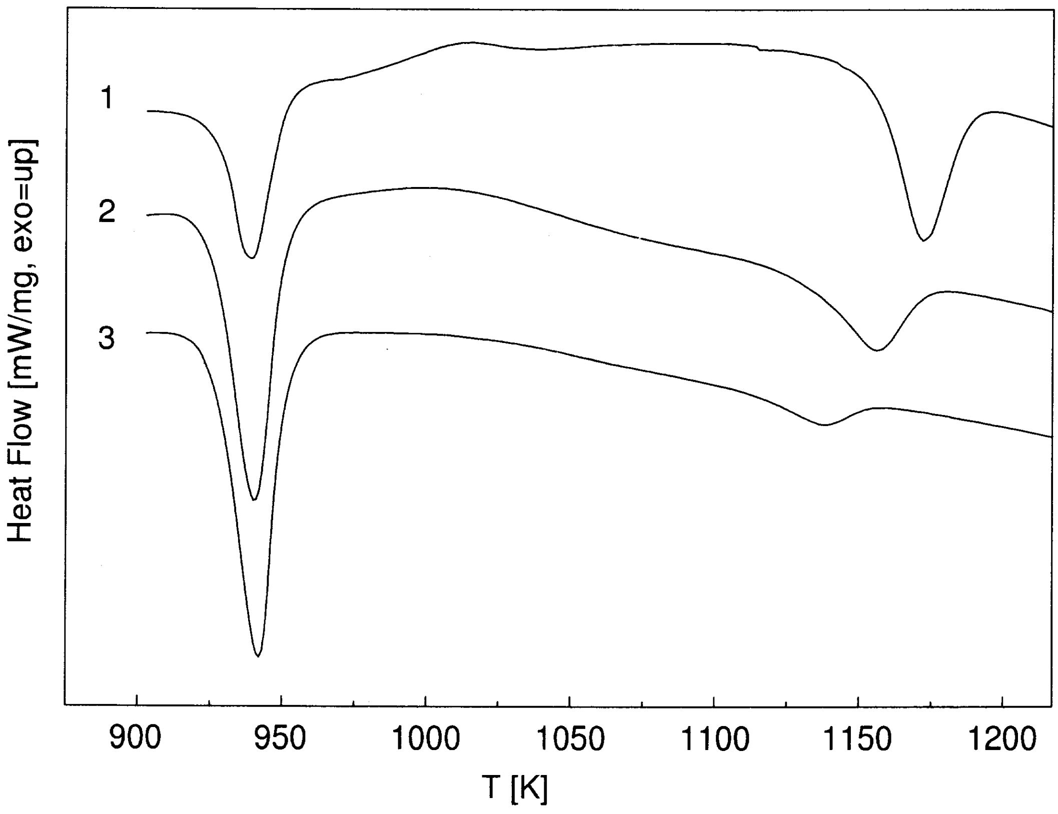

Figure 3.3 DSC traces of the sample of $Al_{0.85}Ti_{0.15}$ mechanical alloy repeatedly heated at $15\,K/min$.

Between heatings, the sample was cooled at the fastest rate possible ($\sim 40 - 50\,K/min$). The result is shown in Figure 3.3. It is observed that while the enthalpy of the eutectic melting peak increases on each subsequent heating cycle, the enthalpy of the second endothermic peak, as well as its peak temperature, decrease. A sample held at 1223 K for 5 hours after initial heating at $15\,K/min$ showed no endothermic peak at near 1173 K on repeated heating.

The temperatures of the observed transitions are shown in Figure 3.4. The subsolidus peaks are broad and overlap strongly. The temperatures of the eutectic melting peak and of the endothermic peak near 1173 K decrease slightly with increasing Ti concentration, while the temperature of the exothermic peak near

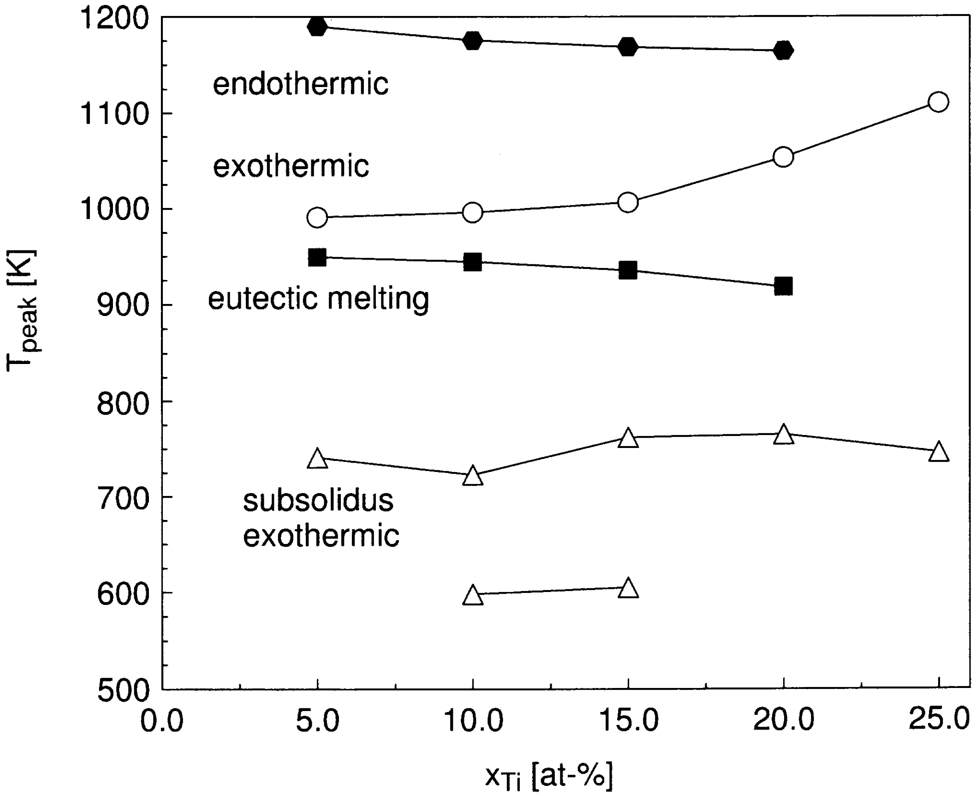

Figure 3.4 A summary of peak temperatures of all observed transitions of Al–Ti mechanical alloys in DSC. Open symbols are exothermic, and, filled symbols are endothermic transitions.

1023 K increases. Temperatures of the liquidus peaks are not shown in Figure 3.4, as they were found to conform to the equilibrium phase diagram [50].

XRD patterns were collected from samples recovered from intermediate temperatures, determined for each composition according to the peak temperatures shown in Figure 3.4. The maximum temperatures from which powder samples could be recovered was limited to 1173 – 1273 K by increasing melt formation. The set of patterns for $Al_{0.85}Ti_{0.15}$ mechanical alloy is shown in Figure 3.5. The fresh mechanical alloy only shows peaks corresponding to an *fcc* phase. At 633 K, in addition to peaks of α-Al, diffraction peaks consistent with the $L1_2$ phase of Al_3Ti were observed. At 873 K, the peaks of α-Al are sharper. The $L1_2$ phase has disappeared and the $D0_{23}$ and $D0_{22}$ phases are observed instead. At 1123 and 1193 K, only peaks of

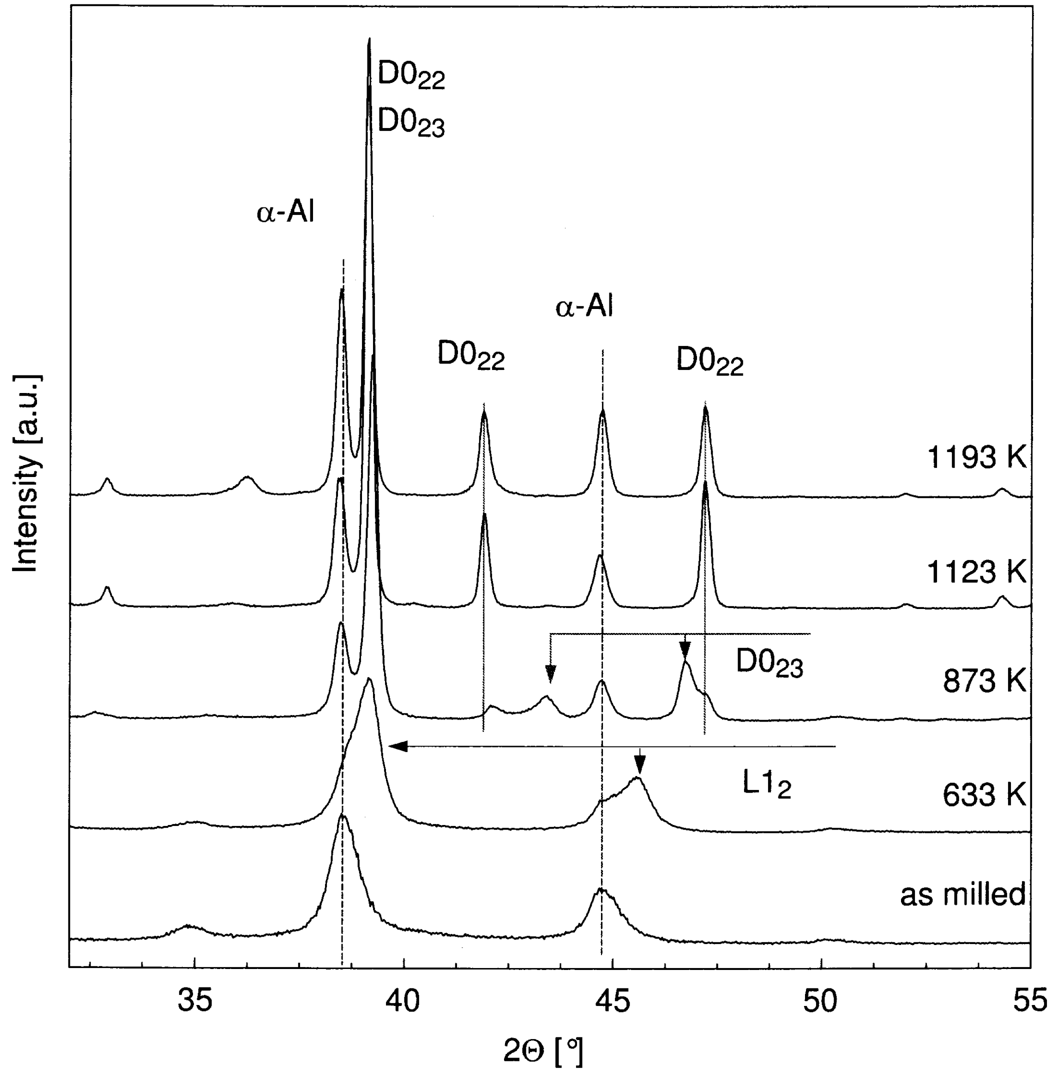

Figure 3.5 Section of XRD patterns of the $Al_{0.85}Ti_{0.15}$ mechanical alloy recovered from intermediate temperatures.

the $D0_{22}$ phase are observed in addition to α-Al. The only observable difference between 1123 and 1193 K is a increase in intensity of α-Al peaks compared to the $D0_{22}$ peaks. Recovery temperatures and observed phases for all compositions are listed in Table 3.1.

Table 3.1 Phases Observed at Intermediate Temperatures

$Al_{0.95}Ti_{0.05}$	$Al_{0.90}Ti_{0.10}$	$Al_{0.85}Ti_{0.15}$	$Al_{0.80}Ti_{0.20}$	$Al_{0.75}Ti_{0.25}$
as-milled MA: $a_0 = 4.0463$ Å	as-milled MA: $a_0 = 4.0423$ Å	as-milled MA: $a_0 = 4.0358$ Å	as-milled MA: $a_0 = 4.0033$ Å	as-milled MA: $a_0 = 3.9886$ Å
	613 K α-Al: $a_0 = 4.040$ Å $L1_2$: $a_0 = 3.998$ Å	633 K α-Al: $a_0 = 4.034$ Å $L1_2$: $a_0 = 3.977$ Å	623 K α-Al: $a_0 = 4.018$ Å $L1_2$: $a_0 = 3.978$ Å	603 K $L1_2$: $a_0 = 3.997$ Å
873 K α-Al: $a_0 = 4.044$ Å $D0_{22}$ $a_0 = 3.839$ Å $a_0 = 8.577$Å	873 K α-Al: $a_0 = 4.056$ Å $D0_{22}$: $a_0 = 3.852$ Å $a_0 = 8.590$Å $D0_{23}$: $a_0 = 3.886$ Å $c_0 = 8.366$ Å	873 K α-Al: $a_0 = 4.050$ Å $D0_{22}$: $a_0 = 3.851$ Å $a_0 = 8.572$Å $D0_{23}$: $a_0 = 3.886$ Å $c_0 = 8.343$ Å	873 K α-Al: $a_0 = 4.051$ Å $D0_{22}$: $a_0 = 3.851$ Å $a_0 = 8.570$Å $D0_{23}$: $a_0 = 3.886$ Å $c_0 = 8.340$ Å	873 K $D0_{23}$: $a_0 = 3.893$ Å $c_0 = 8.356$ Å
	1023 K α-Al: $a_0 = 4.056$ Å $D0_{22}$: $a_0 = 3.846$ Å $c_0 = 8.608$ Å	1123 K α-Al: $a_0 = 4.055$ Å $D0_{22}$: $a_0 = 3.849$ Å $c_0 = 8.613$ Å	1073 K α-Al: $a_0 = 4.053$ Å $D0_{22}$: $a_0 = 3.846$ Å $c_0 = 8.593$ Å $D0_{23}$: $a_0 = 3.858$ Å $c_0 = 8.446$ Å	1123 K $D0_{22}$: $a_0 = 3.843$ Å $c_0 = 8.628$ Å $D0_{23}$: $a_0 = 3.872$ Å $c_0 = 8.482$ Å
		1193 K α-Al: $a_0 = 4.052$ Å $D0_{22}$: $a_0 = 3.849$ Å $c_0 = 8.613$ Å		

Note: the c_0 lattice constant of the $D0_{23}$ phase (ideal c/a=4) is halved for direct comparison to the $D0_{22}$ phase (ideal c/a=2)

The $D0_{22}$ phase is observed for all compositions at the respective highest temperatures from which powders were recovered. The temperature range over which the $D0_{23}$ phase is observed increases with increasing Ti concentration. While The $D0_{23}$ phase is not observed for $Al_{0.95}Ti_{0.05}$, it is observed to coexist with $D0_{22}$ at 873 K for 10, 15, and 20 at-% Ti. It is the only phase detected at 873 K for the Al_3Ti composition, and it persists to at least 1073 K and 1123 K for 20 and 25 at-% Ti, respectively.

3.4 Discussion

X-ray diffraction peaks of the as-milled mechanical alloys become broader and weaker with increasing bulk Ti concentration. In addition, peak positions shift to higher values. From the deviation of the lattice parameter from pure α-Al, the Ti concentration in the *fcc* phase is estimated to be 1.6 at-% (2.8 wt-%) at 15 at-% bulk Ti concentration using a lattice parameter vs. composition relation obtained from rapidly solidified Al–Ti alloys [51]. The remaining Ti is contained in x-ray amorphous phases, or in extended grain boundaries. The maximum observable solubility of any solute in the supersaturated *fcc* phase depends on the mechanical alloying process parameters [36]. The present result is in agreement with 2.46 wt-% Ti previously found for an Al 20 wt-% Ti mechanical alloy [52]. A different maximum solubility of Ti in the *fcc* phase has been reported as 6.7 wt-% Ti [47]. That result corresponded to different milling conditions, and was obtained from the mechanical alloying of an elemental blend with Al_3Ti composition for 10 hours.

The assignment of the exothermic transitions observed for $Al_{0.75}Ti_{0.25}$ to the formation of the $L1_2$, $D0_{23}$, and $D0_{22}$ phases, respectively, agrees with the interpretation suggested in Ref. [47]. Using the pure elements as reference state, the only exothermic transitions expected are due to the formation of the equilibrium phase of Al_3Ti. Considering the observed phase transformations of Al_3Ti (Table 3.1,

Figure 3.5), it appears reasonable to compare the integral exothermic transitions to the enthalpy calculated for Al_3Ti formation from the reference elements ($\Delta_f H_{Al_3Ti} = 47\,kJ/mol$ [53]). Figure 3.6 (A) shows summary of the observed exothermic enthalpies. The combined total enthalpy exceeds the exothermic heat effect calculated for Al_3Ti formation from the elements up to a Ti concentration of 15 at-%. This suggests that the mechanical alloys are metastable with respect to the component elements. At 20 and 25 at-% Ti the sum of exothermic enthalpies drops, consistent with the observed drop in lattice parameter (Figure 3.1) and the assumption that the $L1_2$ phase forms at least partially during milling.

Under equilibrium conditions, the only endothermic transitions expected are eutectic melting and melting at the liquidus. An endothermic transition at this temperature has been reported previously in an $Al_{0.75}Ti_{0.25}$ mechanical alloy, although no interpretation has been offered [47]. Enthalpies of the endothermic transitions are shown in Figure 3.6(B). Due to the wide temperature range over which melting along the liquidus occurs, the DSC features are difficult to integrate reliably and have therefore been omitted from Figure 3.6(B). The decrease of the enthalpy of the endothermic transition near 1173 K on repeated heating (see Figure 3.3), accompanied by the increased eutectic melting peak suggests that both transitions are caused by Al melting. This is further supported by the relative increase in the intensities of α-Al peaks in the diffraction pattern of the sample recovered from 1193 K (Figure 3.5). Figure 3.6(B) shows that for all compositions, the observed enthalpy of eutectic melting is less than that estimated for the system in equilibrium ($\Delta_m H_{Al} = 10.79\,kJ/mol$ [54]). This is a further indication that only a fraction of the Al component melts at this temperature. Part of the nominally free Al in the system must be stabilized, possibly by Ti supersaturation or morphological effects. The peak shape of the endothermic transition near 1173 K (see Figures 3.2 and 3.3) indicates a true phase transition as opposed to an annealing process. At the same time, DSC scans of a sample of mechanical alloy annealed for 5 hours immediately above the transitions show no endothermic transition at this temperature. Therefore, the process must be metastable with the full equilibration of the system being ultimately controlled by diffusion. The repeated occurrence of the peak in subsequent scans of the same sample (see Figure 3.3) then possibly suggests immediate stabilization of the superheated Al component by its decomposition products, or partial re-precipitation on cooling. The latter is considered less likely in view of the long-term annealing result.

3.5 Summary

A series of mechanical alloys in the Al-rich part of the Al–Ti binary system was produced with identical process parameters. The mechanical alloys were chemically homogeneous on a scale of $\sim$ 10 nm. The maximum Ti concentration in α-Al under these milling conditions was found to be 1.6 at-%. The as-milled alloys are increasingly metastable with respect to the component elements; a maximum degree of metastability was observed at 15 at-% Ti. The $L1_2$ phase of Al_3Ti, energetically less stable than the $D0_{23}$ or $D0_{22}$ phases, was likely to be present in mechanical alloys with 20 and 25 at-% Ti based on the observed XRD patterns and trends in enthalpies of exothermic transitions. No such Al_3Ti precursor phases were present in mechanical alloys with compositions up to 15 at-%. Endothermic transitions absent from the equilibrium system were systematically observed near 1173 K. These were interpreted as delayed melting of superheated Al component up to this point.

In the context of energetic materials, the observed metastability is expected to result in a maximum increase in combustion rates and decrease in ignition temperatures for Al–Ti mechanical alloys with Ti concentrations in the range of $10 - 15$ at-%.

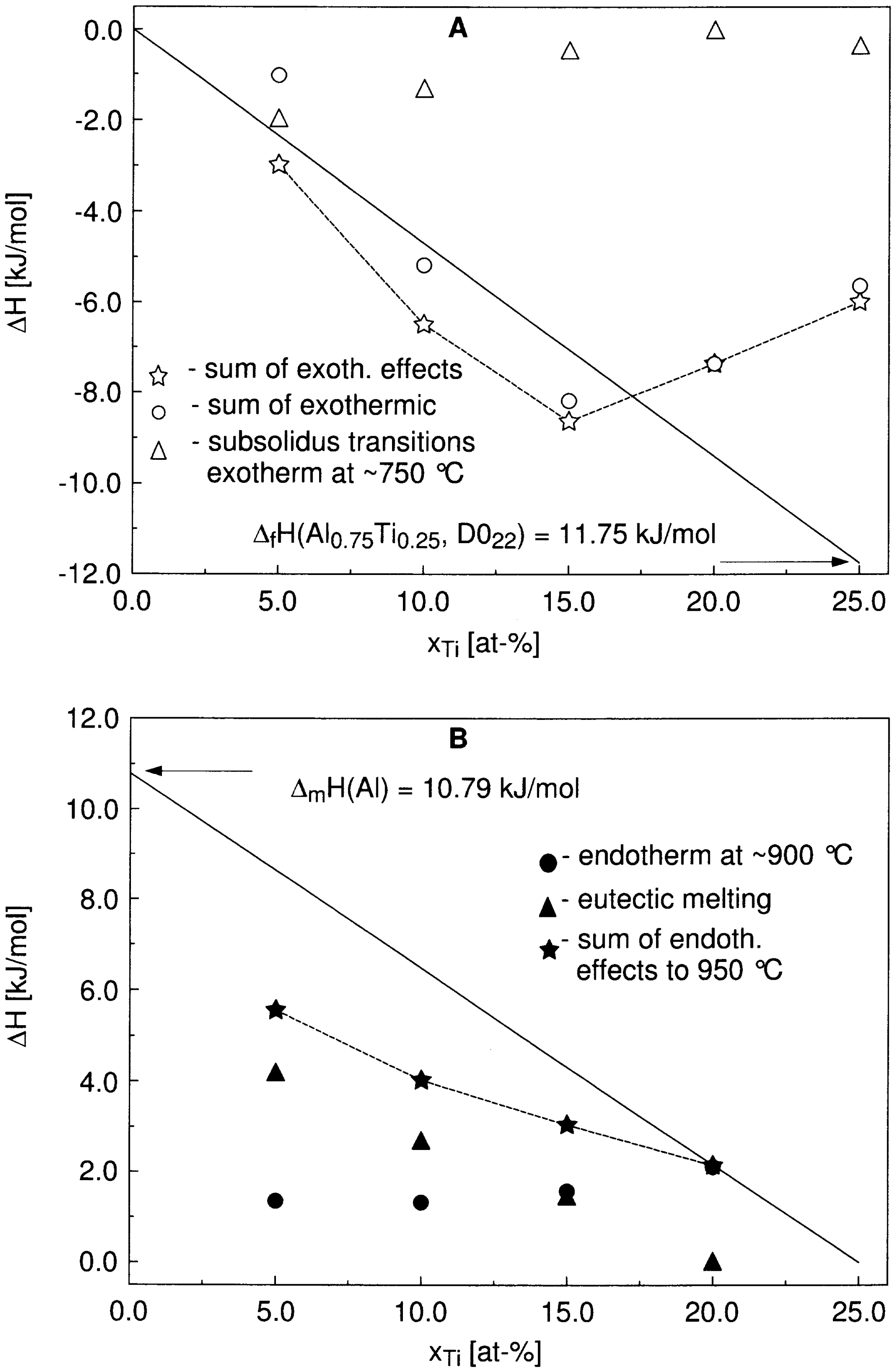

Figure 3.6 Enthalpies of (A) exothermic, and (B) endothermic transitions.

CHAPTER 4

CARBIDE FORMATION IN ALUMINUM–TITANIUM MECHANICAL ALLOYS

4.1 Introduction

Metastable aluminum-based materials, particularly mechanical alloys have recently been suggested as a possible alternative to aluminum as energetic additive to propellants, explosives, and pyrotechnic formulations [13, 34, 37]. Their modified surface morphologies, chemistry-dependent passivating effect of the surface oxide layer, as well as their metastability contribute to shorter ignition delays, higher combustion rates, and more complete combustion [33, 36, 55–57].

In this context, Al-rich mechanical alloys in the Al–Ti system have been prepared and characterized [56]. As part of that investigation, thermal analysis (differential scanning calorimetry, DSC) was performed, and several features remained unexplained. Specifically, an endothermic peak near 1173 K was observed, which could not be attributed to any transition in the Al–Ti binary system. The transition was observed to be partially reversible; reversibility decreased with increasing Ti concentration. This peak had been observed previously in similarly prepared $Al_{0.75}Ti_{0.25}$ mechanical alloys, but was not satisfactorily explained [47].

While the endothermic peak can not be explained by any reaction in the binary Al–Ti system, it is possible that the peak is caused by a peritectic reaction in the ternary Al–Ti–C system. Mechanical alloying usually requires some kind of process control agent to balance particle fracturing and cold-welding. Organic chemicals such as stearic acid ($CH_3 - (CH_2)_{16} - COOH$) are frequently being used. When this additive gradually deteriorates during prolonged milling, a certain degree of carbon contamination of the mechanical alloy will occur.

According to phase equilibrium work in the Al–Ti–C system [58–60], the reaction

$$(1-\mathrm{x})\,\mathrm{Al_4C_3} + 3\,\mathrm{Al_3Ti} = (13-4\mathrm{x})\,\mathrm{Al\,(liq.)} + 3\,\mathrm{TiC_{1-x}} \quad \Delta\mathrm{H} = 84\,\mathrm{kJ/mol} \tag{4.1}$$

occurs in the vicinity of 1173 K. DSC traces similar to the ones observed for mechanical alloys have been observed for Al-rich Al–Ti–C alloys. In this part, a systematic study of the endothermic transition observed for Al–Ti mechanical alloys is presented, and the relationship of this transition and reaction 4.1 is established.

4.2 Experimental

The mechanical alloys, which were synthesized as described in the § 3.2 , have been used for this specific investigation.

Morphology and compositional homogeneity of the mechanical alloys were initially examined on a LEO 1530 Field Emission Scanning Electron Microscope (FE-SEM). The SEM is equipped with an energy dispersive x-ray spectrometer (EDX) that allows standardless compositional analysis with a maximum spatial resolution of approximately 1 μm.

Temperature-dependent structural transformations were investigated by differential scanning calorimetry (DSC) using a Netzsch Simultaneous Thermal Analyzer STA409-PC. Samples were contained in alumina sample pans. The furnace of the STA409-PC was evacuated to approximately 0.03 bar and back-filled with Ar (Matheson, 99.998%) three times before each measurement. During measurements, the furnace was continuously flushed with Ar at approximately 10 ml/min. DSC

Table 4.1 Bulk Compositions of Mechanical Alloys in at-%

x_{Al}	x_{Ti}	x_C	$\frac{Al}{Al+Ti}$
91.7	4.8	3.4	95
86.8	9.6	3.5	90
81.9	14.4	3.7	85
77.0	19.2	3.8	80
72.1	24.0	3.9	75

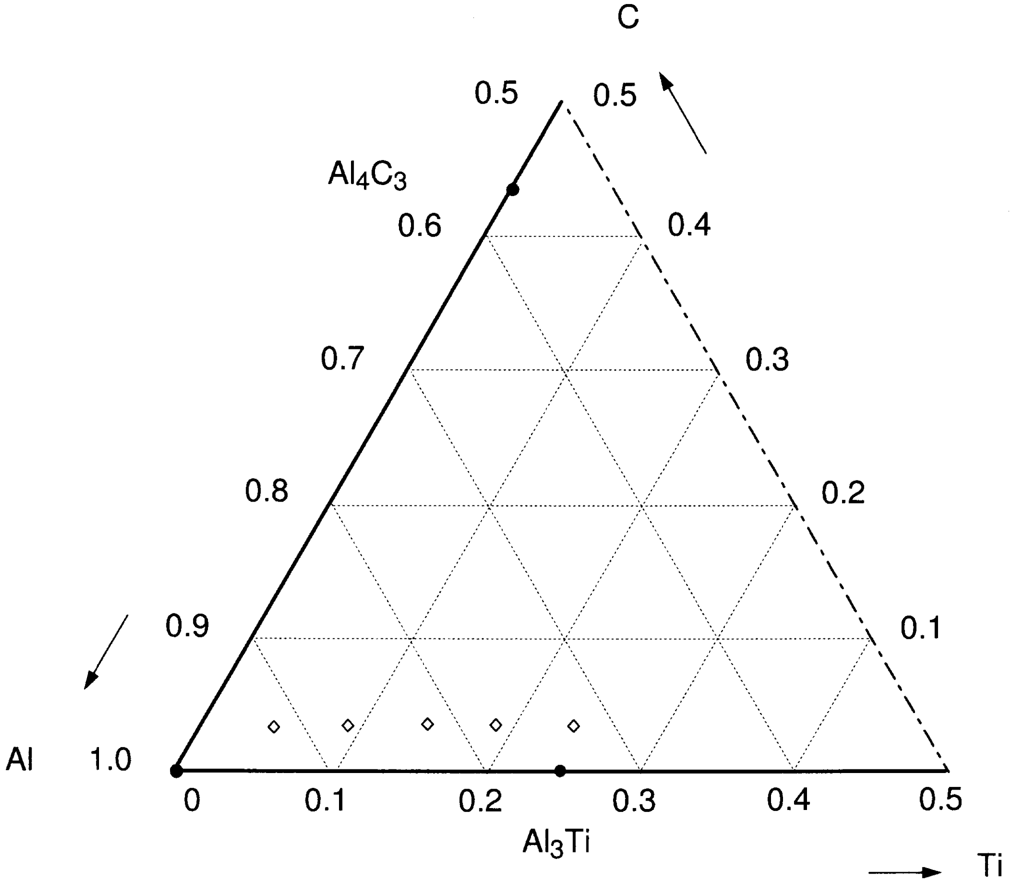

Figure 4.1 Al-rich corner of the Al–Ti–C ternary system, showing the effective bulk compositions.

traces were recorded at various heating rates in the range of 5 to 40 K/min up to a maximum temperature of 1773 K. Selected samples were heated and cooled repeatedly to determine the reversibility of the observed effects.

Partially annealed material from selected temperatures up to 1273 K was obtained by heating the DSC to a specific temperature at 10 K/min, followed by cooling to room temperature at a rate of approximately 40 K/min. These samples were analyzed by XRD to identify and quantify the phases present, and determine their lattice parameters. A set of samples recovered in this way was also cross-sectioned for SEM imaging.

4.3 Results

The use of stearic acid as a process control agent alloys effectively changed the bulk compositions, introducing carbon as an additional component. Table 4.1 and Figure 4.1 show the resulting bulk composition of the mechanical alloys assuming that carbon was quantitatively transferred from PCA to the mechanical alloys.

Figure 4.2 shows DSC traces of an $Al_{0.85}Ti_{0.15}$ mechanical alloy at varying heating rates. The temperature range shown includes melting of Al at $\sim$ 933 K and the endothermic peak attributed to reaction 4.1 near 1173 K. The formation of the $D0_{22}$ phase of Al_3Ti is visible as a broad exothermic feature between 973 and 1073 K. In contrast to the melting of Al, the endothermic peak near 1173 K shifts towards higher temperatures at higher heating rates.

Samples of $Al_{0.95}Ti_{0.05}$, $Al_{0.90}Ti_{0.10}$, and $Al_{0.85}Ti_{0.15}$ were heated at various rates for a simplified kinetic analysis. Peak temperatures were processed according to Kissinger's method [61]; the results are shown in Figure 4.3. Apparent activation energies as estimated from linear regression are 320 kJ/mol for $Al_{0.95}Ti_{0.05}$, 548 kJ/mol for $Al_{0.90}Ti_{0.10}$, and 547 kJ/mol for $Al_{0.85}Ti_{0.15}$, respectively.

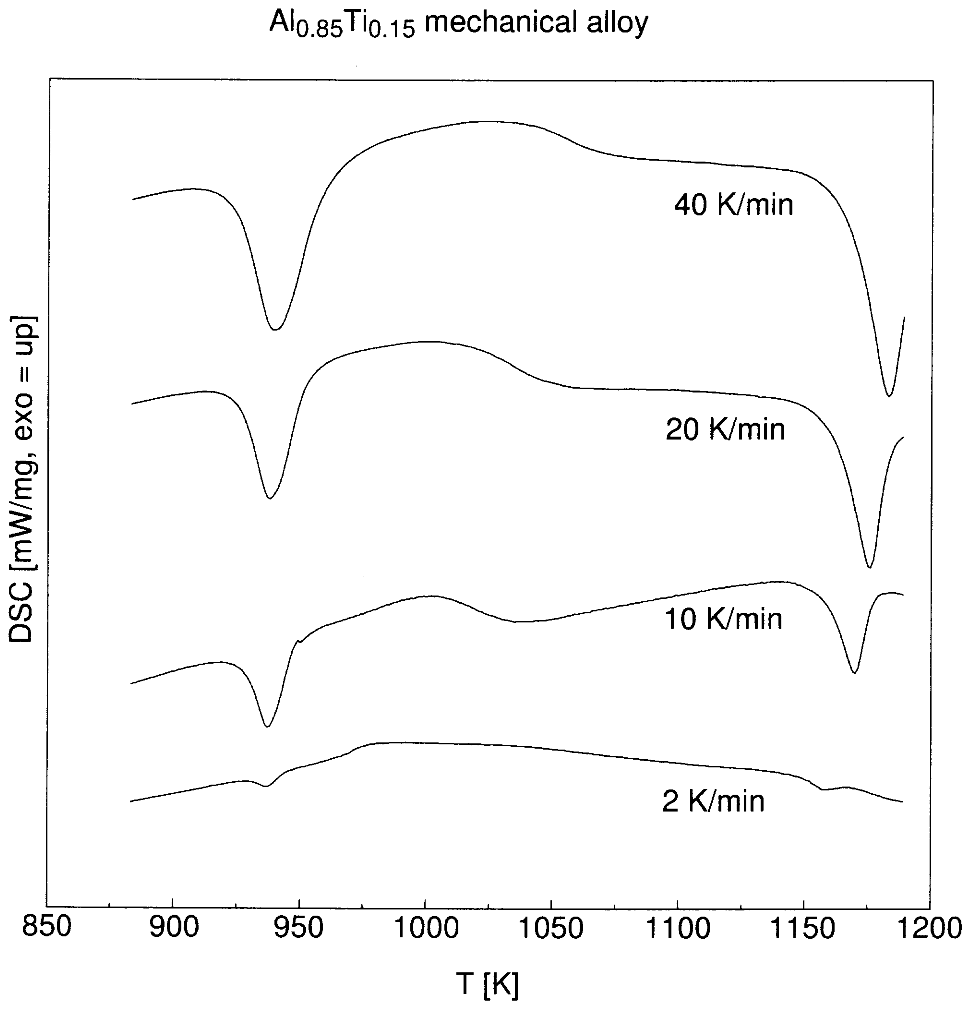

Figure 4.2 DSC traces of an $Al_{0.85}Ti_{0.15}$ mechanical alloy sample at varying heating rates in the melting region.

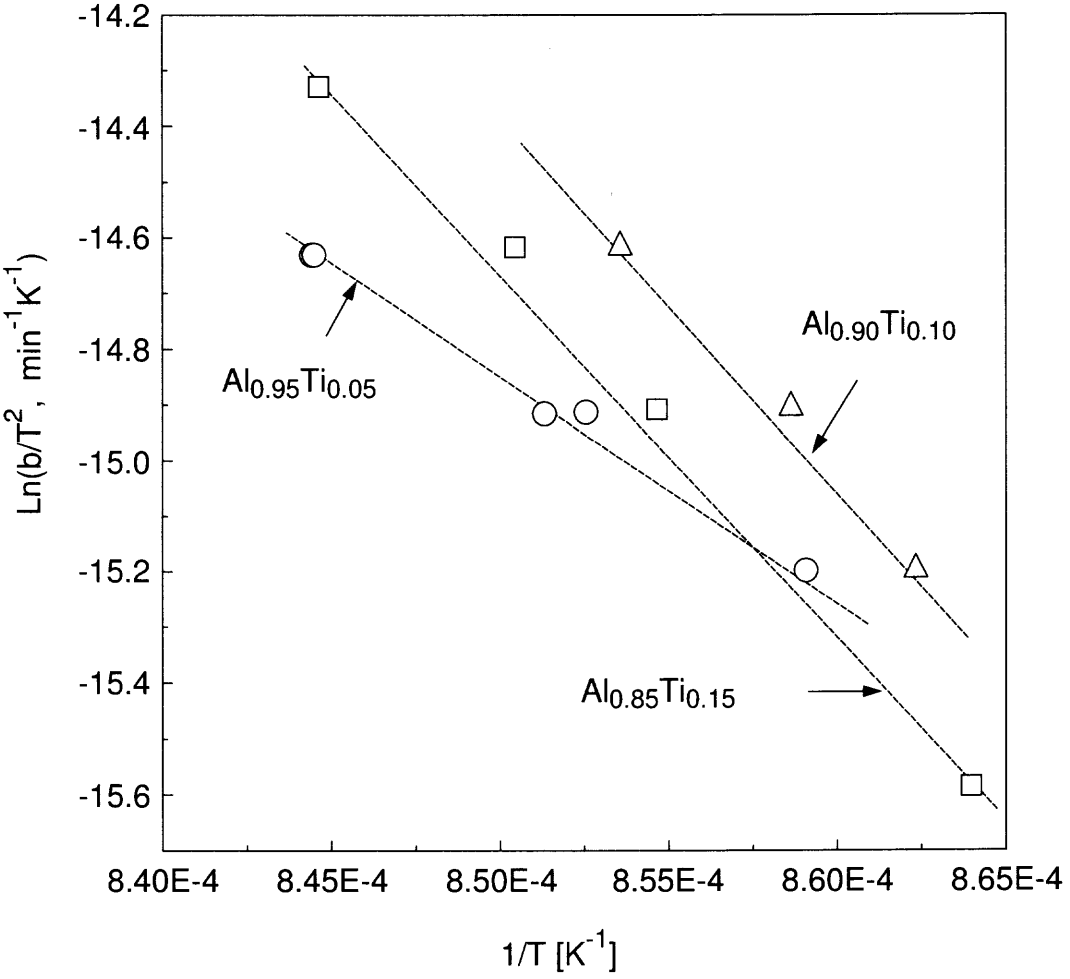

Figure 4.3 Kissinger plot of the high-temperature endothermic peak.

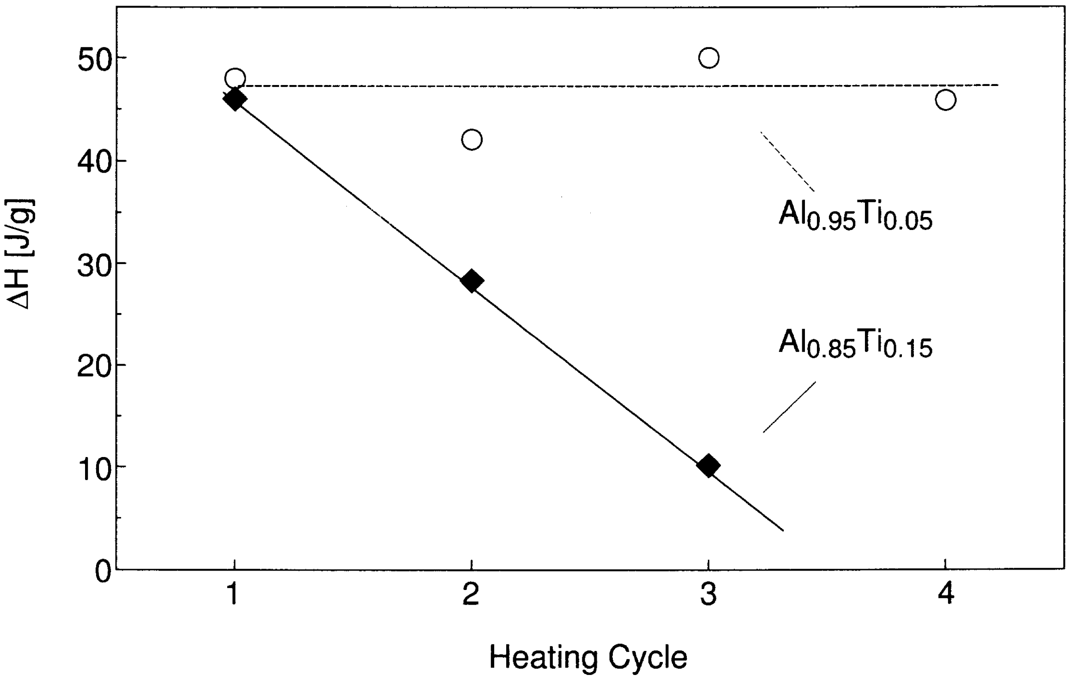

Figure 4.4 Heat effect of the observed endothermic transition of the sample repeatedly heated near 1173 K.

Figure 4.4 shows the heat effects observed for repeated heating of the same sample of an $Al_{0.95}Ti_{0.05}$ and an $Al_{0.85}Ti_{0.15}$ mechanical alloy, respectively. For $Al_{0.95}Ti_{0.05}$, the transition is repeatable within the error of the experiment, while the observed heat effect deteriorates during repeated heating-cooling cycles of the $Al_{0.85}Ti_{0.15}$ mechanical alloy. Figure 4.5 shows XRD patterns of an $Al_{0.85}Ti_{0.15}$ mechanical alloy annealed at 1123 K and 1193 K.

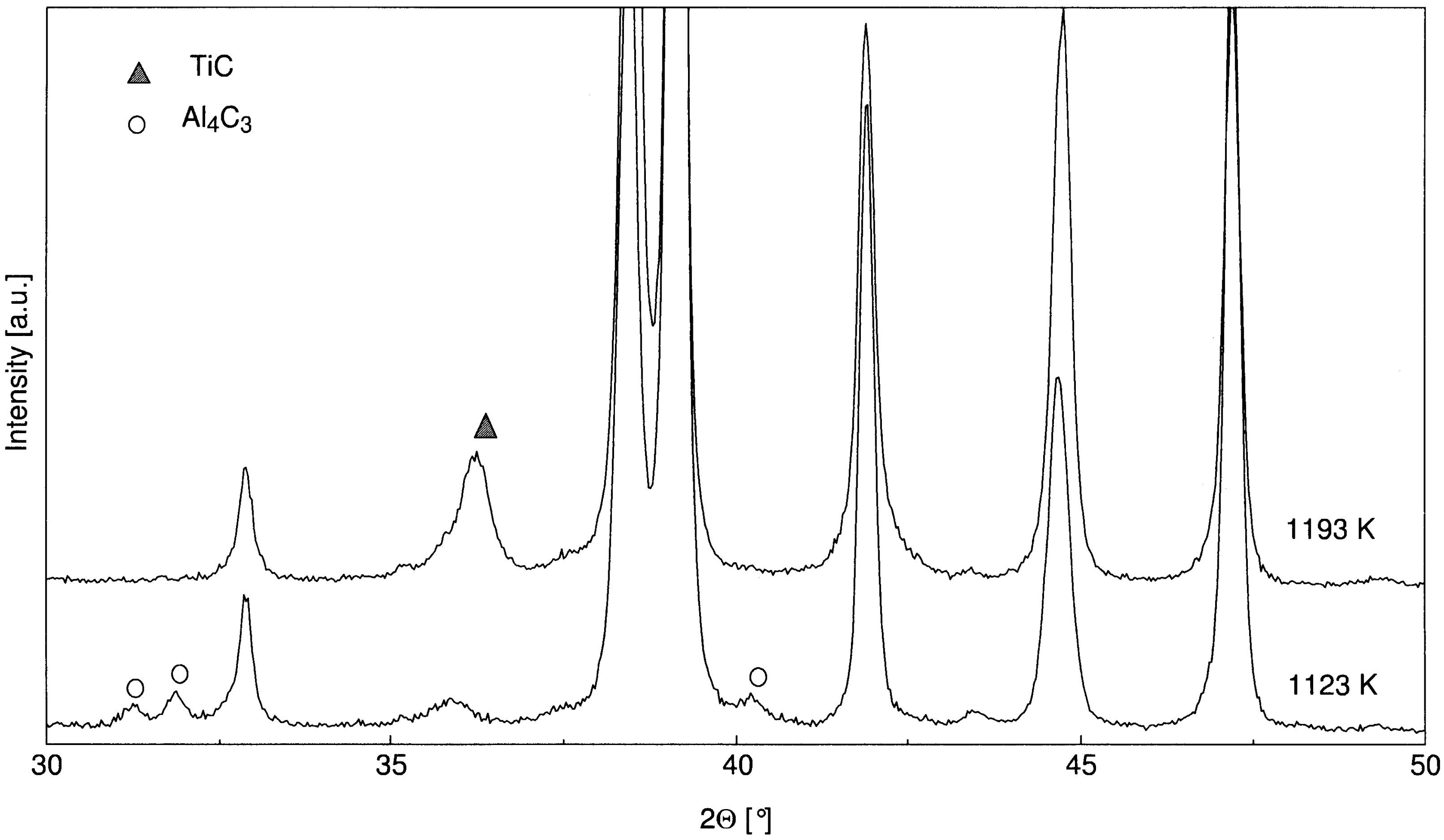

Figure 4.5 XRD patterns of an $Al_{0.85}Ti_{0.15}$ mechanical alloy annealed at 1123 K and 1193 K. Unmarked peaks belong to the major phases, α-Al and Al_3Ti ($D0_{22}$).

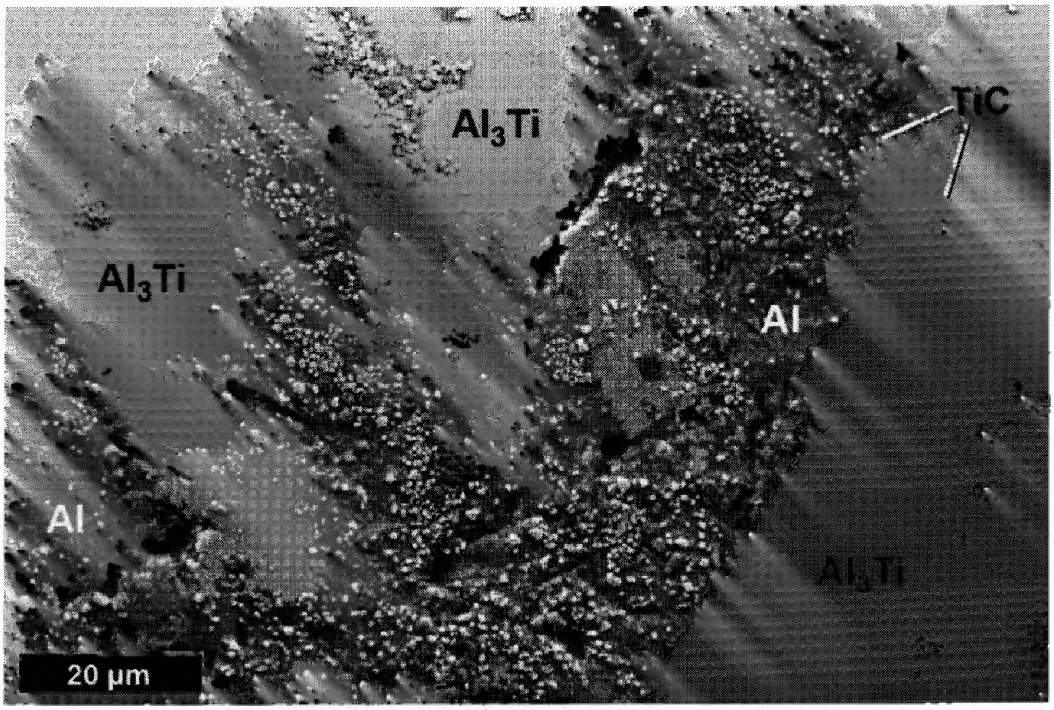

Figure 4.6 Backscattered electron image of an $Al_{0.85}Ti_{0.15}$ mechanical alloy annealed at 1773 K.

Al_4C_3 is visible at 1123 K while only TiC can be detected at 1193 K. Figure 4.6 shows a backscattered electron image of an $Al_{0.85}Ti_{0.15}$ mechanical alloy that has been heated to 1773 K. After this treatment, the endothermic transition was no longer observed on repeated heating. The image shows large, relatively homogeneous grains of Al_3Ti, and a fine grained matrix of Al. Throughout the sample, small (less than $\sim 1\,\mu m$) grains of TiC are visible; they are more abundant in the Al phase than in Al_3Ti. Although reaction 4.1 occurs near 1173 K as confirmed by DSC, these TiC grains are not detectable at the same resolution in samples that were annealed at $\sim$ 1223 K.

4.4 Discussion

The ternary peritectic reaction described by equation 4.1 has been studied previously. Its reaction enthalpy was reported as 84 kJ/mol (158 J/g) at 1200 K [60]. Assuming

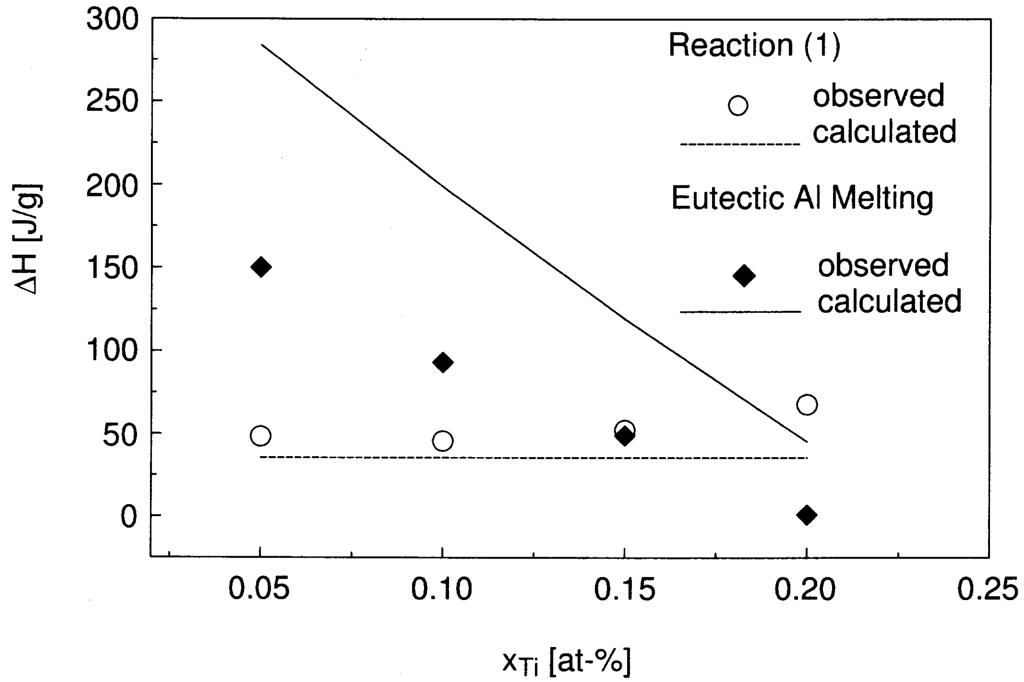

Figure 4.7 Observed and calculated heat effects of Al melting and of reaction 4.1.

that all carbon introduced by the process control agent is available for the reaction, the reaction enthalpy relative to the whole mechanically alloyed powder is calculated to be 35.4 J/g, independent of the bulk Al/(Al+Ti) ratio. Figure 4.7 compares the measured heat effects with the expected enthalpy as well as observed and calculated values for the enthalpy of Al melting. The observed enthalpy of reaction 4.1 agrees with the calculation reasonably well. Based on the coincidence of the temperature range of reaction 4.1 and the observed endothermic peak and the similarity of the calculated and measured enthalpies, the observed peak is attributed to reaction 4.1. However, Figure 4.7 shows that the melting of Al is significantly less endothermic than expected. This suggests an effective Al/(Al+Ti) ratio lower than expected from the bulk compositions. The presence of an additional Al-containing phase must be considered although no such phase has been identified by XRD. Particularly, partial reaction with the alumina DSC sample pans can not conclusively be ruled out.

The endothermic peak associated with reaction 4.1 was not observed for the $Al_{0.75}Ti_{0.25}$ nominal bulk composition. Contrary to this, in a previous investigation, Zhang et al. [47] did observe the transition in an $Al_{0.75}Ti_{0.25}$ mechanical alloy. In that study, mechanical alloys had been prepared in a planetary mill for a series of milling times. Reaction 4.1 was observed and reversible after 10, 15, and 20 hours of milling, while it was absent after 30 and 40 hours of milling. This likely reflects the state of the mechanical alloy; after relatively short milling times the mechanical alloy consists of fine-grained Al and Ti. This is consistent with the observation of Ti peaks in XRD patterns of not fully milled mechanical alloys [47]. Only after prolonged milling, a homogeneous Al_3Ti phase is achieved. From the homogeneous phase, the transition is no longer observed.

The apparent progressive deterioration of the observed heat effect of reaction 4.1 (see Figure 4.4) in the present work, specifically its dependence on the bulk composition of the mechanical alloy must be evaluated in this context. All mechanical alloys were prepared with the same milling time. As reported previously [56] , XRD analysis suggests that at this milling time, an Al_3Ti precursor, similar to the $L1_2$ phase of Al_3Ti forms only for the nominal compositions $Al_{0.80}Ti_{0.20}$ and $Al_{0.75}Ti_{0.25}$, while the XRD patterns of more Al-rich mechanical alloys more closely resemble pure Al (Figure 4.1 in Ref. [56]). The observation that this influences the apparent reversibility of the reaction suggests that mechanical alloys with a higher Ti concentration are more homogeneous after the same milling time than those with a lower Ti concentration, and that the loss of reversibility is caused by gradual encapsulation of TiC by Al_3Ti, formed on cooling. In addition to this effect, reaction rates also decrease due to the coarsening of the TiC precipitates and the resulting reduction of the TiC–Al interface area.

The formation of TiC in this ternary system is an equilibrium reaction; it is therefore not thermally activated. The process is however controlled by the thermally activated diffusion of C and Ti in the Al melt as the rate limiting step, thus the apparent activation energies reflect the respective diffusion rates.

4.5 Summary

Based on the coincidence of the endothermic transitions observed in mechanical alloys with those observed previously in conventional Al–Ti–C alloys, it is concluded that the formation of TiC according to reaction 4.1 is responsible for the previously unexplained transition in Al–Ti mechanical alloys. This implies that nearly all carbon from the process control agent was incorporated in the mechanical alloy during processing. Apparent activation energies for the formation of TiC in Al–Ti mechanical alloys prepared with a carbon-containing process control agent were determined.

CHAPTER 5

OXIDATION BEHAVIOR OF ALUMINUM–TITANIUM MECHANICAL ALLOYS ON ALUMINUM-RICH SIDE

5.1 Introduction

Al–Ti alloys with high Al content, especially Al_3Ti intermetallic compounds, have been of significant interest for structural and other applications because of their high strength, low density, and potential for oxidation resistance [62–65]. Mechanical alloying (MA) has been used to prepare various stable, metastable or dispersion strengthened Al–Ti alloys. Recently, mechanical alloying was used to prepare Al rich Al–Ti alloys for use as metallic high energy-density materials such as additives for propellants, explosives, or pyrotechnic formulations [33, 56, 66].

Aluminum powders are currently used in many related energetic materials [67]; however the advantages of aluminum resulting from its high combustion enthalpy are impeded by the relatively long ignition delays of aluminum particles. The modified surface morphologies, chemistry-dependent passivating effect of the surface oxide layer, as well as the metastability of the Al–Ti mechanical alloys contribute to their shorter ignition delays, higher combustion rates, and more complete combustion [57, 66].

Understanding the oxidation mechanisms and kinetics of the alloy powders at elevated temperatures is essential for modeling their performance in energetic applications. At the same time, oxidation mechanisms are critical for stability of such alloys during their storage and handling. The stability of alloys is also important for structural applications, where oxidation and corrosion need to be minimized. Ideally it should be possible to control oxidation rates by adjusting process parameters of the mechanical alloying synthesis and the alloy composition. Thus, this study is aimed to investigate the oxidation mechanisms of aluminum-rich Al–Ti alloys prepared by MA. It is also of interest to compare the oxidation mechanisms of powders of Al-rich Al–Ti alloys with those of pure aluminum powders. The background of the research presented here necessitates the work with powders as opposed to consolidated bulk alloys. It is expected that the results will be sufficiently general to be useful for insights in the oxidation of consolidated bulk alloys. Recent interest in metal-ceramic composites for net-shape manufacturing as well as reactive bonding applications [68, 69] emphasizes the need for reliable powder oxidation data. Further, the very large specific surface area of powders results in comparatively high oxidation rates enabling relatively rapid analysis by constant-heating rate thermal analysis vs. long-term constant-temperature oxidation experiments.

While the aluminum component in Al–Ti alloys is known to form Al_2O_3 scales at the metal-oxide interface via selective oxidation [70], the issue is complicated by the competition with titanium for oxygen, and the relatively fast growth rate of TiO_2 [71]. Further, previous reports on the oxidation of Al-rich Al–Ti cast alloys [72, 73] indicate that α-Al_2O_3 is the only alumina phase present in the scale. Conversely, the scale of mechanically alloyed powders is reported to consist of γ-Al_2O_3 and TiO_2 at the outer surface and γ-Al_2O_3 near the alloy as a protective layer [74]. Anomalously high oxidation rates at early stages were observed in both cast alloys and MA materials [72, 74]. No comprehensive and consistent oxidation mechanism has been proposed so far.

In this part of the research, the oxidation behavior is studied for a set of mechanically alloyed Al-rich Al–Ti powders with varied compositions. This work presents the results of thermal analysis and phase compositions of the partially

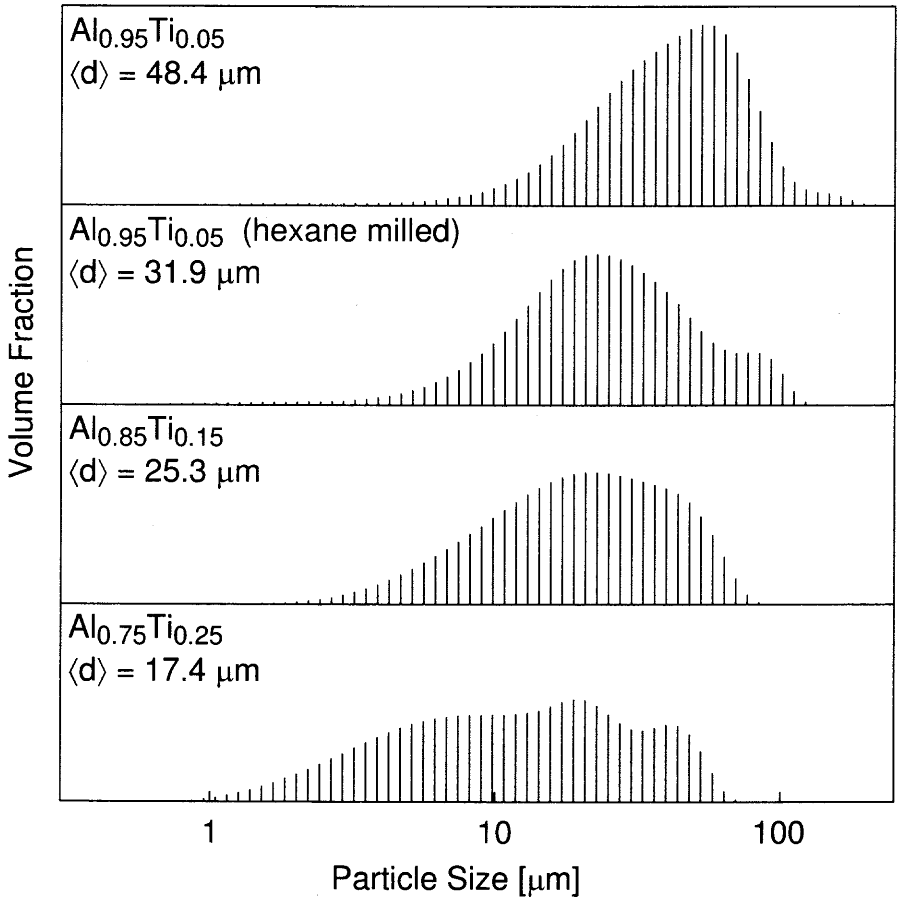

Figure 5.1 Selected size distributions of the mechanically alloyed Al–Ti powders.

oxidized alloys. The oxidation mechanisms are discussed based on the reported experimental results.

5.2 Experimental

5.2.1 Synthesis

The mechanical alloys, which were synthesized as described in the § 3.2 , have been used as initial materials for oxidation investigation.

Powder samples for selected compositions with reduced particle sizes were prepared by additional milling of the mechanical alloy under hexane for a short time.

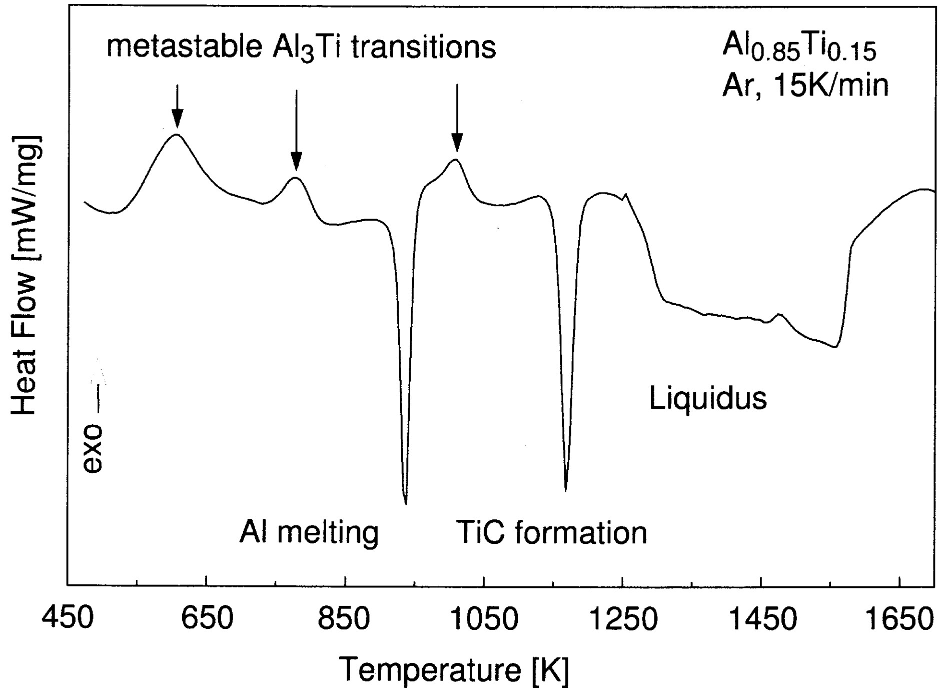

Figure 5.2 Characteristic transitions of mechanically alloyed powder with $Al_{0.85}Ti_{0.15}$ composition in an inert atmosphere.

The size distributions measured for mechanical alloys with different compositions as well as for the samples with reduced particle sizes are shown in Figure 5.1.

The Al–Ti mechanical alloys under investigation have been described in detail in the Chapter 3. The main results related to the present work are briefly summarized below. SEM imaging and EDX analysis showed the cross-sectioned particles to be chemically homogeneous within the resolution limit of the instrument, ~ 100 nm, with non-homogeneity somewhat higher at increasing Ti contents. Phase transitions occurring during heating of the mechanical alloys were studied by thermal analysis. A characteristic DSC trace is shown in Figure 5.2. The observed endothermic equilibrium events include the melting of Al at 933 K (not observed for $Al_{0.80}Ti_{0.20}$ and $Al_{0.75}Ti_{0.25}$ alloys) and the liquidus occurring in the temperature range of 1473 – 1673 K, depending on the alloy's bulk composition. Non-equilibrium peaks include relatively small and broad exothermic subsolidus transitions observed below

873 K, an exothermic peak near 1023 K present in lower-Ti concentration alloys, and an endothermic peak near 1173 K observed for all compositions with less than 25% Ti.

In the subsolidus region, exothermic transitions are associated with the formation of a series of successively less metastable Al_3Ti phases from the original mechanical alloy [47, 56]. An exothermic transition observed between 973 K and 1023 K, has been ascribed previously to the formation of the equilibrium phase of Al_3Ti [47, 56]. The second endothermic peak observed around 1173 K has been attributed to the precipitation of titanium carbide, caused by low levels of carbon introduced by the PCA (stearic acid) [75].

5.2.2 Materials Characterization

Morphology and texture of intermediate oxidation products were examined on a LEO 1530 Field Emission Scanning Electron Microscope (SEM). The SEM is equipped with an energy dispersive X-ray spectrometer (EDX) that allows standardless compositional analysis with a maximum spatial resolution of approximately 1 μm.

Structure and phase makeup of each recovered sample were determined by XRD on a Bragg-Brentano type Phillips X'pert MRD diffractometer operated at 45 kV and 40 mA, using Cu-K-α radiation ($\lambda = 1.5438$ Å). All XRD patterns were quantitatively analyzed by whole-pattern fitting using the General Structure Analysis System (GSAS) software [76].

Particle size distributions of the mechanical alloys were determined by Low-Angle Laser Light Scattering (LALLS) using a Coulter LS 230 analyzer. Suspensions for particle size analysis were prepared in water.

5.2.3 Thermal Analysis

Differential thermal analysis (DTA) and thermo-gravimetric analysis (TGA) were performed in a Netzsch Simultaneous Thermal Analyzer STA409 PC. The instrument was calibrated for temperature with the melting points of a set of metal standards. The temperature is accurate within ± 1 K. Experiments were performed in oxygen (50 ml/min; Matheson, 99.98%); a low flow of argon (10 ml/min; Matheson, 99.999%) was supplied to protect the thermo-balance. The experiments were therefore effectively conducted in a mixed 5:1 oxygen/argon atmosphere. Samples were contained in alumina crucibles. Sample sizes were $15 - 20\,mg$; heating rates ranged from $2\,K/min$ to $40\,K/min$. To recover intermediate oxidation products for further analysis by x-ray diffraction (XRD), the furnace power was turned off at predetermined temperatures. The effective cooling rate achieved this way is estimated to be about $40\,K/min$.

5.3 Results

5.3.1 Oxidation

DTA traces for starting powders and mechanical alloys heated at $15\,K/min$ in oxygen are shown in Figure 5.3A. The simultaneously recorded TGA traces are shown in Figure 5.3B. The measurements of the temperature-dependent sample mass were normalized by the initial sample mass as opposed to the effective surface area of the powder, since for the given size distributions (see Figure 5.1), sample mass and surface area are proportional.

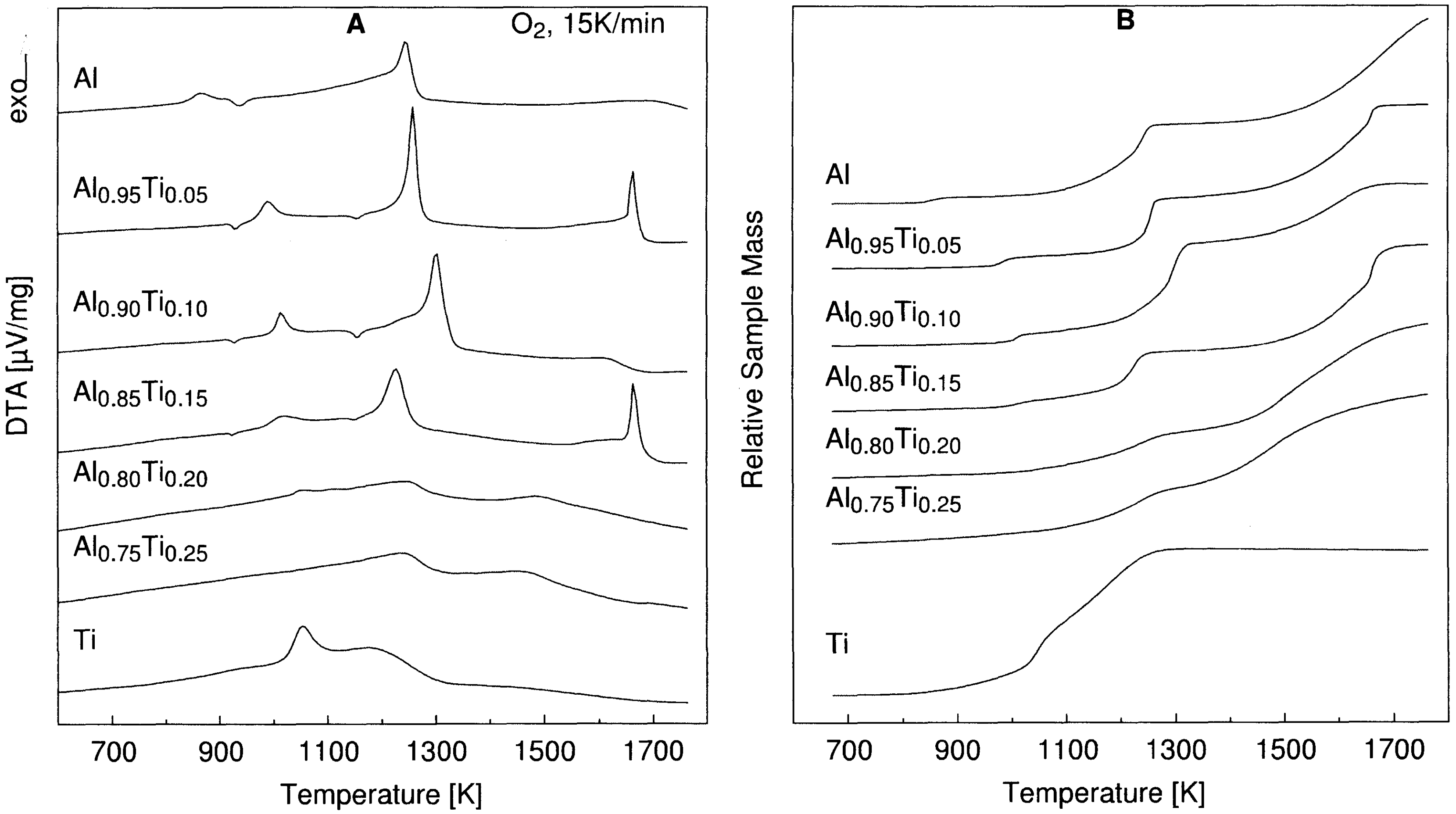

Figure 5.3 DTA (A), and simultaneous TGA (B) traces of mechanically alloyed powders heated in oxygen at 15 K/min. The measurements of the sample mass relative to the mass of the unoxidized material are plotted on a consistent scale; however, the traces are shifted for clarity

For aluminum the first oxidation peak occurs at about 863 K, before its melting point. The second oxidation peak begins gradually after the melting and ends sharply at about 1273 K. The third, very broad and poorly repeatable oxidation peak is observed around 1673 K. The exothermic DTA peaks correlate well with the stepwise weight increase observed from the TGA trace. This sequence of aluminum oxidation was observed in several earlier studies [77, 78]. Recently, a mechanism has been proposed connecting the stepwise oxidation of aluminum with polymorphic phase changes occurring in the growing layer of Al_2O_3 [79].

Oxidation of titanium powder produces a broad exothermic event starting at about 873 K and continuing until about 1323 K. The peak maximum is observed at 1173 K. Another, narrower exothermic event is also observed with a peak maximum at 1053 K. Changes in the oxidation behavior of pure Ti near 1023 K have been previously attributed to the transformation of the α-Ti to the β-Ti solid solution [80].

The oxidation sequence of the Al–Ti mechanical alloys includes three steps, similar to that of pure aluminum, especially for aluminum-rich compositions. The TGA traces correlate well with the DTA, showing that the exothermic peaks are accompanied by a mass increase, as expected for oxidation processes. The first oxidation step is well resolved for the $Al_{0.95}Ti_{0.05}$, $Al_{0.90}Ti_{0.10}$, $Al_{0.85}Ti_{0.15}$, and $Al_{0.80}Ti_{0.20}$ alloys, however, unlike for pure aluminum, it occurs at a temperature exceeding the Al melting point. The second and third oxidation steps become broader and occur at gradually lower temperatures with increased titanium concentration. The position of the third oxidation step was generally not reproducible, and in some experiments sharp peaks overlap with the broad oxidation peak. It was observed that these sharp peaks occurred at discrete temperatures, roughly coinciding with peritectic reactions in the binary Al–Ti system [81]. Specifically, sharp peaks have been observed at 1618 K (near the $Al_3Ti \Longrightarrow L + Al_{11}Ti_5$ peritectic at 1628 K), in the range 1643 – 1653 K (near the $Al_{11}Ti_5 \Longrightarrow L + TiAl$ peritectic at 1652 K), and at 1753 K (slightly above the $TiAl \Longrightarrow L + \alpha\text{-}Ti$ peritectic at 1717 K). This coincidence suggests that the observed peaks are due to oxidation of the freshly formed melt. The observation of peritectic reactions outside the initial compositional range ($x_{Ti} < 25$ at-%) indicates that the Al component possibly oxidizes preferentially, leaving an Al-depleted alloy residue that may contain more than 25 at-% Ti.

Both, melting due to the Al-Al_3Ti eutectic and due to TiC formation [75] are clearly resolved in the DTA traces for the three most aluminum-rich compositions. The eutectic disappears for the $Al_{0.80}Ti_{0.20}$ alloy, while the TiC formation peak can still be resolved. The stepwise oxidation pattern is poorly resolved for this alloy. For the $Al_{0.75}Ti_{0.25}$ composition, the first oxidation step does not occur at all, the remaining two oxidation steps are extremely broad, and no aluminum melting peaks are observed.

5.3.2 Oxidation Kinetics

Thermal analysis was performed at different heating rates to characterize the oxidation kinetics. Example DTA and TGA traces for the $Al_{0.95}Ti_{0.05}$ mechanical alloy oxidized at 2, 15, and 40 K/min are shown in Figure 5.4. As expected, the peaks for all the oxidation events shift towards higher temperatures at increased heating rates. Due to the somewhat irreproducible nature of the features near the 3rd oxidation step, these temperatures were omitted from the analysis. Table 5.1 summarizes the recorded peak temperatures.

The results were processed to determine the kinetics of the different events using an isoconversion method after Kissinger [82]. It was therefore assumed that each oxidation event can be described as a first order reaction. According to the Kissinger method, the activation energy, E_A, is found as the slope of a straight line

Table 5.1 Peak Temperatures of Oxidation Steps (from TGA)

Composition	Heating Rate [K/min]	Exothermic DTA peaks (oxidation events)[K]	
		1^{st} event	2^{nd} event
$Al_{0.95}Ti_{0.05}$	2	946.2	1195.8
	15	985.0	1255.6
	40	1001.0	1277.8
$Al_{0.90}Ti_{0.10}$	5	981.6	1255.8
	15	1008.6	1293.0
	40	1017.2	1329.2
$Al_{0.85}Ti_{0.15}$	5	994.0	1192.0
	10	1015.2	1211.6
	15	1009.8	1223.6
	20	1027.8	1232.8
	40	1033.0	1242.8
$Al_{0.80}Ti_{0.20}$	5	1014.8	1191.2
	15	1040.2	1245.6
	40	1064.2	1254.0
$Al_{0.75}Ti_{0.25}$	5		1212.0
	10		1230.4
	15		1239.4
	20		1256.6
	40		1234.4

described by:

$$\ln\left(\frac{b}{T_{max}^2}\right) = -\frac{E_A}{RT_{max}} + B \tag{5.1}$$

where b is the heating rate, Tmax is the peak temperature, R is the universal gas constant, and the constant B depends on the specific reaction model. Kissinger plots obtained for the different oxidation events are shown in Figure 5.5. For each experimental data set, the activation energies were estimated from linear fits. The results are presented in Table 5.2.

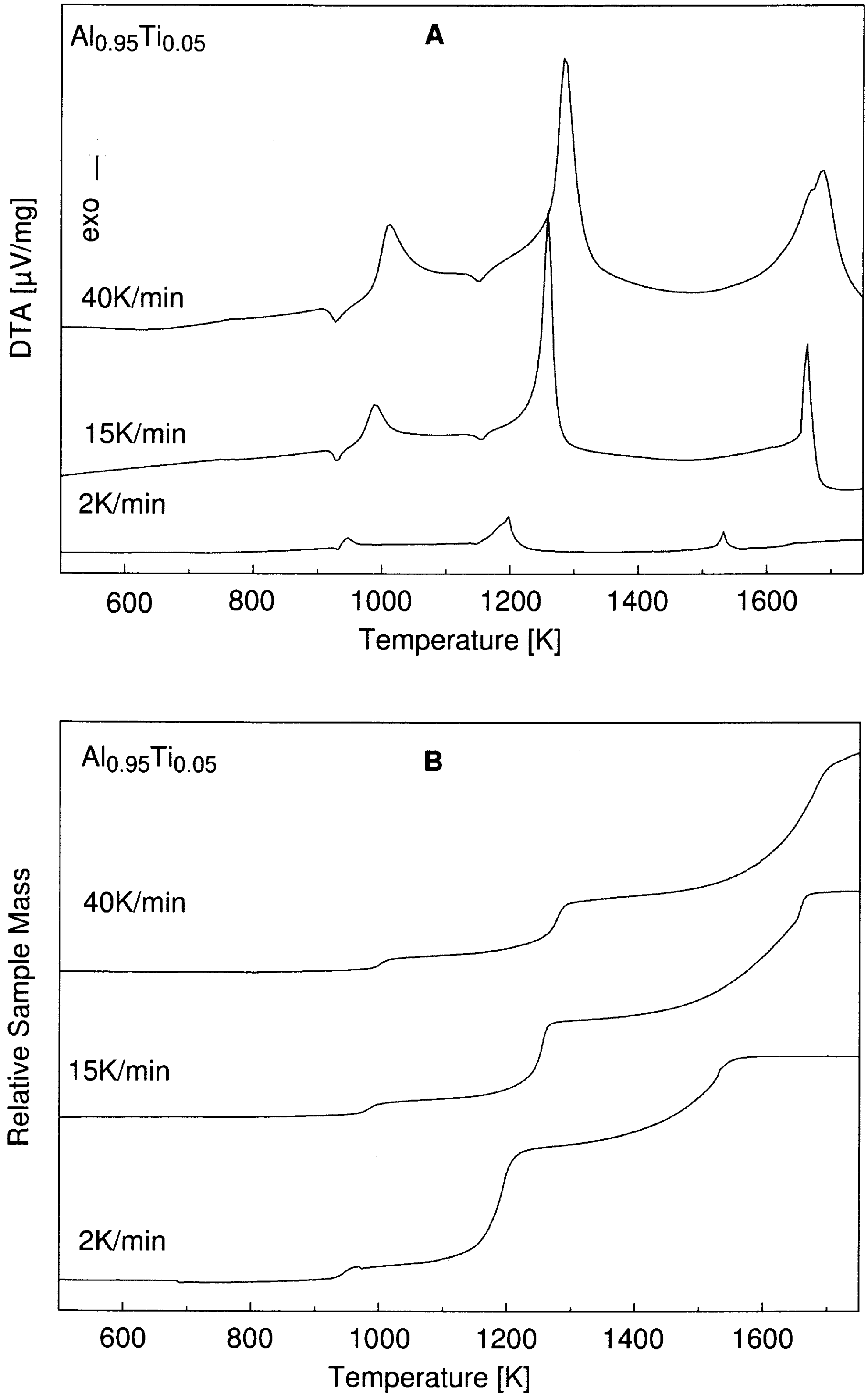

Figure 5.4 Thermal analysis of the mechanically alloyed $Al_{0.95}Ti_{0.05}$ heated in O_2 with different heating rate. (A) DTA and (B) TG

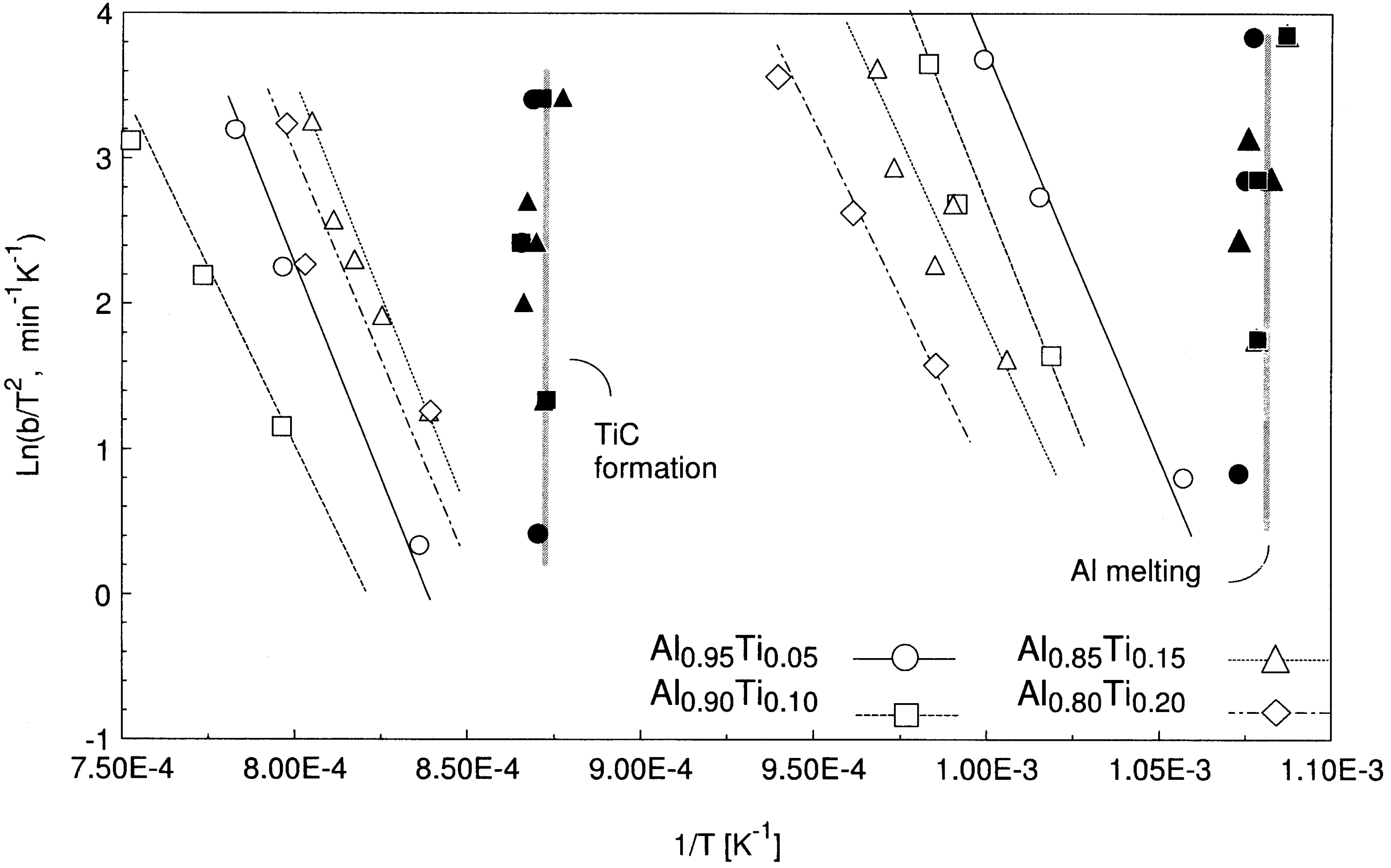

Figure 5.5 Kinetic analysis of the first and the second oxidation steps for mechanically alloyed Al–Ti powders. (see text)

Table 5.2 Activation Energies Estimated for Different Oxidation Events Using the Kissinger Method

Composition	E_A(kJ/mol)	
	1^{st} event	2^{nd} event
$Al_{0.95}Ti_{0.05}$	408.3	433.8
$Al_{0.90}Ti_{0.10}$	430.0	371.5
$Al_{0.85}Ti_{0.15}$	384.2	459.0
$Al_{0.80}Ti_{0.20}$	360.4	332.6
$Al_{0.75}Ti_{0.25}$		383.5

5.3.3 Phase Compositions of Partially Oxidized Samples

Samples oxidized to intermediate stages were recovered at temperatures determined using the positions of the respective oxidation peaks for each composition. The samples were typically obtained before the first oxidation event and after each of the three events observed at increasingly higher temperatures. Example XRD patterns for the $Al_{0.95}Ti_{0.05}$, $Al_{0.85}Ti_{0.15}$, and $Al_{0.75}Ti_{0.25}$ mechanical alloys are shown in Figure 5.6 a, b and c.

Each pattern is labeled with the temperature at which the sample was recovered. All main peaks in the XRD patterns are labeled according to the phases identified using the JCPDS database [83] and assigned for quantitative analysis; the few weak peaks labeled with question marks could not be identified. The unidentified peaks are present in the $Al_{0.75}Ti_{0.25}$ samples recovered from 1023 to 1323 K and could be due to an Al–Ti phase richer in Ti than Al_3Ti. Weak peaks of ZrO_2 are detected, showing contamination of the mechanical alloys by the material of the milling balls and vial. These contamination peaks became weaker or completely disappear at elevated temperatures.

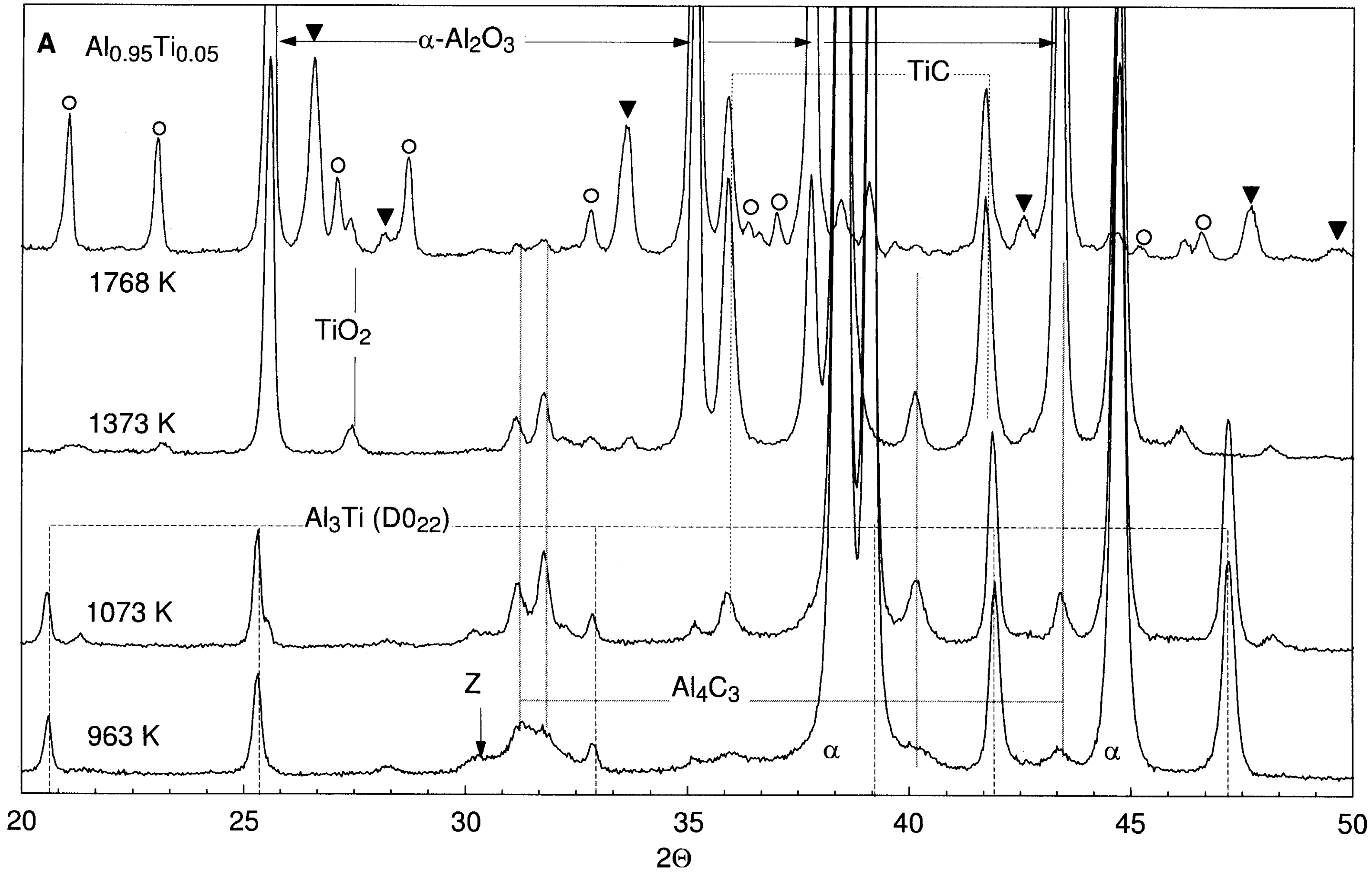

Figure 5.6a $Al_{0.95}Ti_{0.05}$ X-ray diffraction patterns for partially oxidized Al–Ti mechanical alloys.

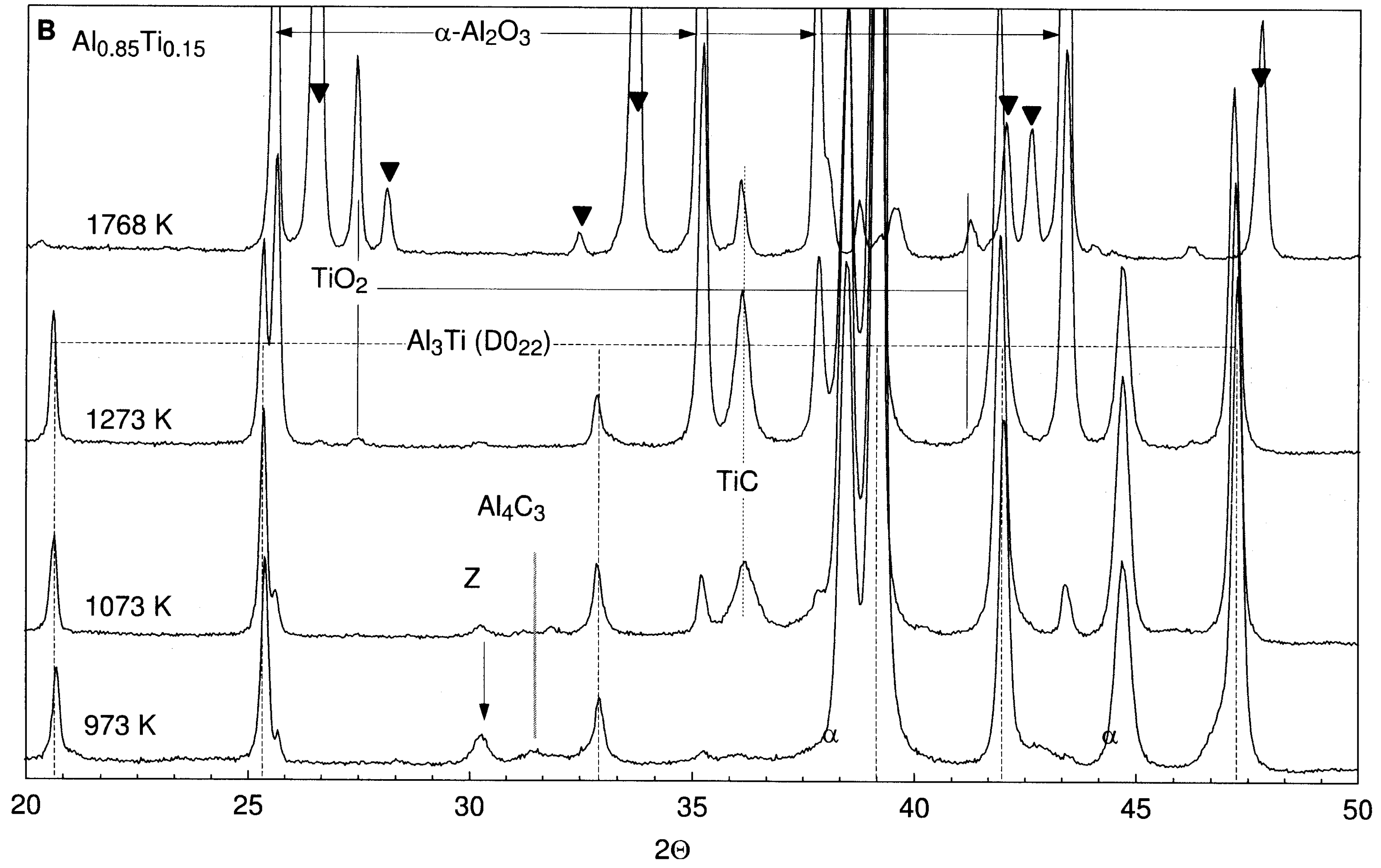

Figure 5.6b $Al_{0.85}Ti_{0.15}$ X-ray diffraction patterns for partially oxidized Al–Ti mechanical alloys.

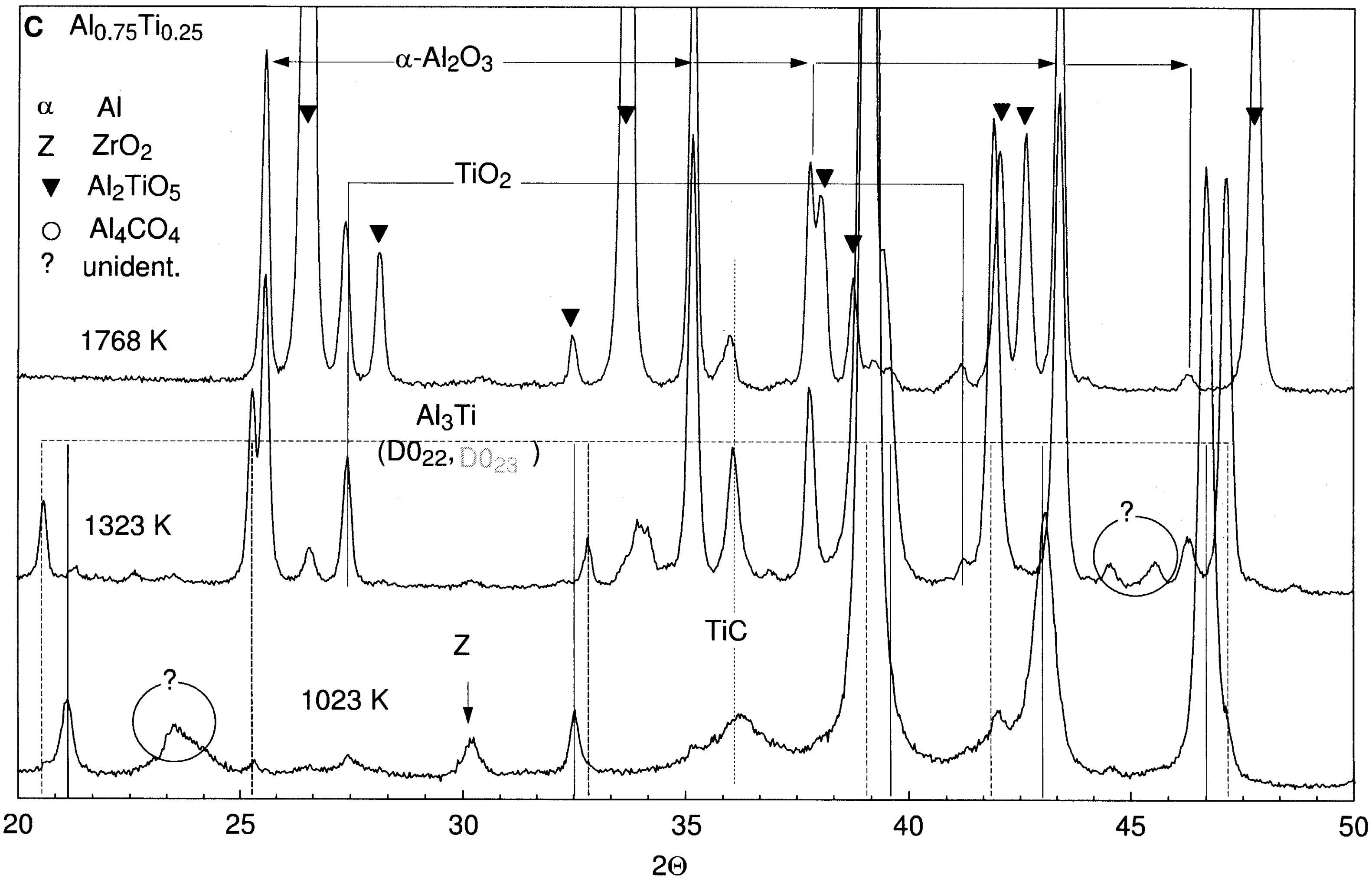

Figure 5.6c $Al_{0.75}Ti_{0.25}$ X-ray diffraction patterns for partially oxidized Al–Ti mechanical alloys.

Table 5.3 Phase Compositions (Weight %) of Samples Oxidized to Intermediate Temperatures According to Quantitative X-ray Analysis

Composition	T(K)	Al_3Ti	Al	Al_4C_3	TiC	TiO_2	α-Al_2O_3	Al_2TiO_5	Al_4CO_4
$Al_{0.95}Ti_{0.05}$	963	28.21	63.67	8.12	-	-	-	-	-
	1073	24.18	55.02	12.29	-	-	8.51[a]	-	-
	1213	6.71	52.31	9.80	4.64	-	26.54	-	-
	1373	-	34.07	4.20	6.76	0.33	54.64	-	-
	1768	-	0.70	0.84	2.41	0.49	81.28	7.54	6.74
$Al_{0.90}Ti_{0.10}$	953	52.79	46.49	0.72	-	-	-	-	-
	1023	18.41	59.03	4.09	13.47	-	5.00	-	-
	1273	0.63	32.20	-	14.25	0.85	52.08	-	-
	1703	-	7.01	-	7.92	0.76	79.28	5.03	-
	1768	-	0.40	-	2.44	0.83	76.06	20.27	-
$Al_{0.85}Ti_{0.15}$	973	71.35	27.56	1.10	-	-	-	-	-
	1073	58.18	28.60	-	5.62	-	7.60	-	-
	1273	33.88	13.00	-	7.47	-	45.65	-	-
	1693	-	0.99	-	-	4.18	66.37	28.47	-
	1768	-	-	-	-	2.52	61.42	35.50	-
$Al_{0.80}Ti_{0.20}$	973	91.47	8.53	-	-	-	-	-	-
	1073	63.14	10.84	-	7.14	-	18.88	-	-
	1323	48.04	3.06	-	6.34	0.42	42.14	-	-
	1768	-	-	-	-	2.52	46.91	50.57	-
$Al_{0.75}Ti_{0.25}$	1023	100[b]	-	-	-	-	-	-	-
	1323	45.21	-	-	4.28	2.24	46.74	1.54	-
	1768	-	-	-	-	2.44	34.18	63.38	-

Note: [a] including $\gamma - Al_2O_3$ (7.33 %) and $\alpha - Al_2O_3$ (1.18 %)

[b] including the $D0_{23}$ (88.24 %) and $D0_{22}$ (11.76 %) modifications of Al_3Ti

A summary of the quantitative phase analysis of all partially oxidized Al–Ti mechanical alloys is shown in Table 5.3. Before the first oxidation event, the major phases for all the mechanical alloy compositions are Al_3Ti and Al. Note that the Al_3Ti phases ($D0_{22}$ and $D0_{23}$) form during the heating of mechanical alloys, corresponding to the low-temperature exothermic phase changes illustrated in Figure 5.2. Aluminum carbide, Al_4C_3, is also present in most powders; the carbon contamination is the result of using stearic acid as PCA. For the $Al_{0.75}Ti_{0.25}$ (Al_3Ti) composition, free aluminum is not observed and $D0_{23}$ is the major Al_3Ti form. After the first oxidation event, small amounts of aluminum oxide, Al_2O_3, are detected for all powders. Titanium oxide, TiO_2, appears after the second and third oxidation events. Large amounts of the ternary Al_2TiO_5 oxide form at higher temperatures. While aluminum carbide is observed to oxidize when the temperatures increases, titanium carbide forms above approximately 1173 K.

The formation of different polymorphs of Al_2O_3 over the course of oxidation was of particular interest because such polymorphic transformations have recently been proposed to explain the mechanism of stages observed in the oxidation of aluminum [79]. However, the weak and broad peaks of γ-Al_2O_3 and other transition alumina phases are usually difficult to distinguish by powder XRD, especially for such complicated XRD patterns as produced by the Al–Ti mechanical alloys. To increase XRD peak intensities from thin oxide layers, samples of the $Al_{0.95}Ti_{0.05}$ mechanical alloy with reduced particle sizes and therefore higher specific surface areas were prepared and used in these experiments. An example XRD pattern with the range of the diffraction angles expanded to include the strongest peaks of γ-Al_2O_3 is shown in Figure 5.7.

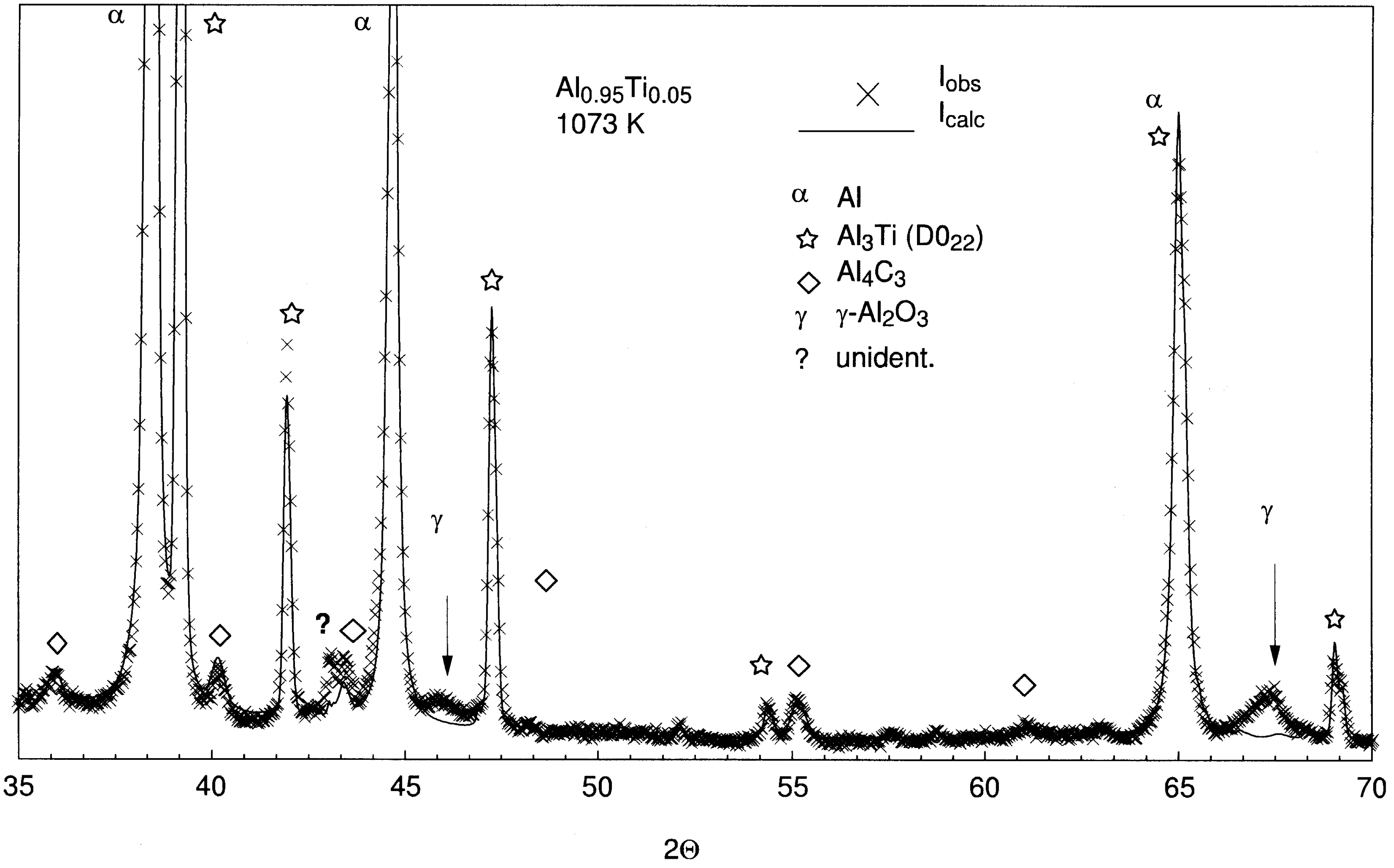

Figure 5.7 Result of whole-pattern refinement of a partially oxidized $Al_{0.95}Ti_{0.05}$ powder. Mismatch between observed and calculated curves shows the presence of wide γ-Al_2O_3 reflections.

The experimental pattern is shown together with the curve computed using GSAS whole pattern fitting in which no Al_2O_3 phases were included. Very broad peaks corresponding to γ-Al_2O_3 are visible in the difference between observed and calculated patterns. Matching these peaks using Rietveld refinements would require making a number of assumptions regarding the strain and crystallite size distribution of the weakly crystalline γ-Al_2O_3, which was beyond the scope of this project.

5.4 Discussion

5.4.1 Phases Formed as Result of Oxidation of Al–Ti Mechanical Alloys

The phase compositions of partially oxidized samples determined using quantitative X-ray analysis could be incomplete. Specifically, amorphous or nanocrystalline phases are likely to be overlooked; some deviations from stoichiometry in the detected phases could remain unnoticed as well. It is possible to assess how significant these factors are by comparing the calculated aluminum/titanium balance with the values of the starting powder mixture. This comparison is shown in Figure 5.8. For the samples oxidized below 1273 K, for all mechanical alloys except $Al_{0.75}Ti_{0.25}$, the phase compositions obtained from the quantitative X-ray analysis underestimated the bulk aluminum content by about 10 – 20%. In general, for each mechanical alloy, the calculated Al–Ti balance approached that of the starting mixture for samples recovered after the second oxidation event, at temperatures around 1273 K. At higher temperatures, the bulk titanium content was underestimated by 10 – 30 %.

The Ti deficit at high temperatures may be due to a number of causes. Phases containing Ti^{3+} could exist in proximity to any unoxidized alloy [84]. Oxidation of titanium generally occurs through dissolution of oxygen and formation of a sequence of intermediate oxides before full oxidation is achieved [85, 86]. Titanium oxides incorporating $Ti^{3+}(Ti_xO_{2x-1})$ have generally low symmetry, which gives rise to

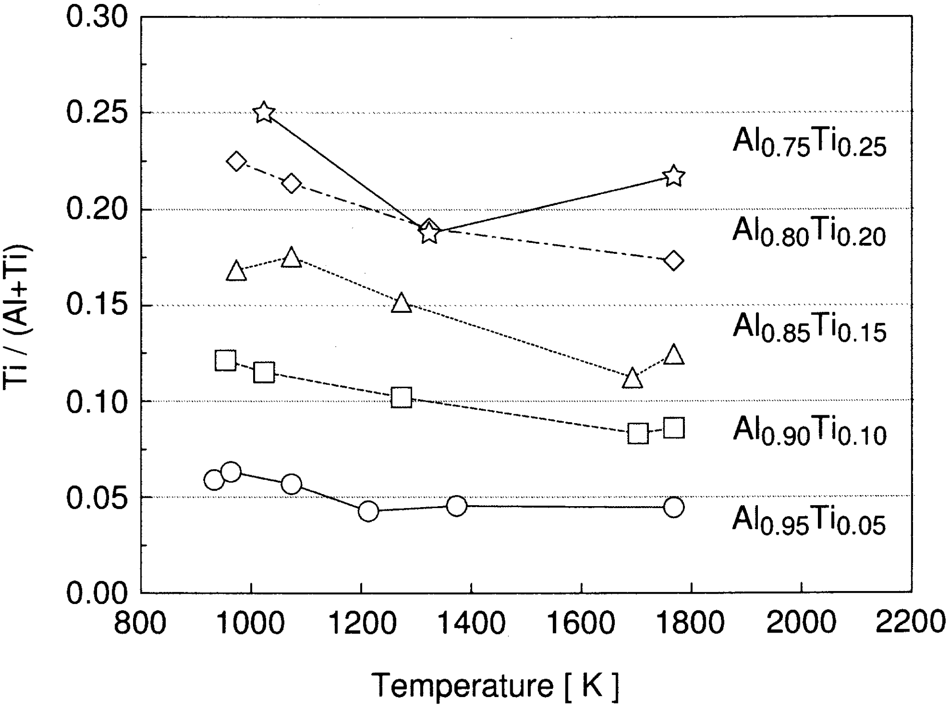

Figure 5.8 Actual Ti/Al ratios as determined by XRD phase analysis compared to nominal values.

lower relative intensities of individual XRD reflections. Such phases could therefore remain unidentified in the quantitative analysis. Further, a solid solution series between Al_2TiO_5 and Ti_3O_5 exists at oxygen partial pressures low enough to stabilize Ti^{3+} [87]. For the quantitative analysis, the stoichiometry of this phase was assumed to be constant, which could cause the overall Ti content to be underestimated while overpredicting Al. Any high-temperature cationic disorder in Al_2TiO_5 was not accounted for, possibly introducing additional bias in the match of XRD intensities.

It is more difficult to interpret the discrepancy in the bulk aluminum balance for the samples recovered from lower temperatures. Since no indication of Al volatilization was seen in the present and previous investigations [56], the mass balance requires that aluminum must be present in either a metallic or an oxide phase. Amorphous material is not directly detectable by XRD, and therefore part of the aluminum contained in amorphous alumina scales may remain unaccounted for. To evaluate whether amorphous alumina could account for the discrepancy between the initial sample composition and the composition implied by the XRD patterns, the weight changes were estimated for different mechanical alloys based on the predicted composition changes and compared with the experimental TGA curves. The results of this comparison are shown in Figure 5.9. The open symbols show the sample mass expected if all the unaccounted aluminum is present in amorphous alumina phase. Note that the actual mass of the sample recovered from a specific temperature is expected to be somewhat greater than the respective mass from the TGA curve at the same temperature because of some residual sample oxidation during the sample recovery procedure. However, the mass of the sample containing required quantities of alumina would be much greater than the experimental TGA data, suggesting that only part of the unaccounted for aluminum is oxidized. Solid symbols show masses calculated assuming that all unaccounted for Al is not oxidized. These values are in most cases smaller than the actual TGA observation. Therefore, parts of the metallic aluminum, or its oxide, respectively, could be nanocrystalline or amorphous and thus undetectable by XRD. Note that for the cases when no aluminum deficit was observed, both open and solid symbols coincide and reflect directly the weight of the composition implied by the XRD analysis.

Whenever possible, a balance between the metallic aluminum and alumina was estimated that would result in the match of the TGA and the predicted sample mass changes. The overall compositions including the proposed phases of aluminum unaccounted for by XRD for all the mechanical alloys are presented in Table 5.4, where the titanium deficits are also shown. The compositions shown in Table 5.4 are proposed to provide the best approximation to the actual sample compositions.

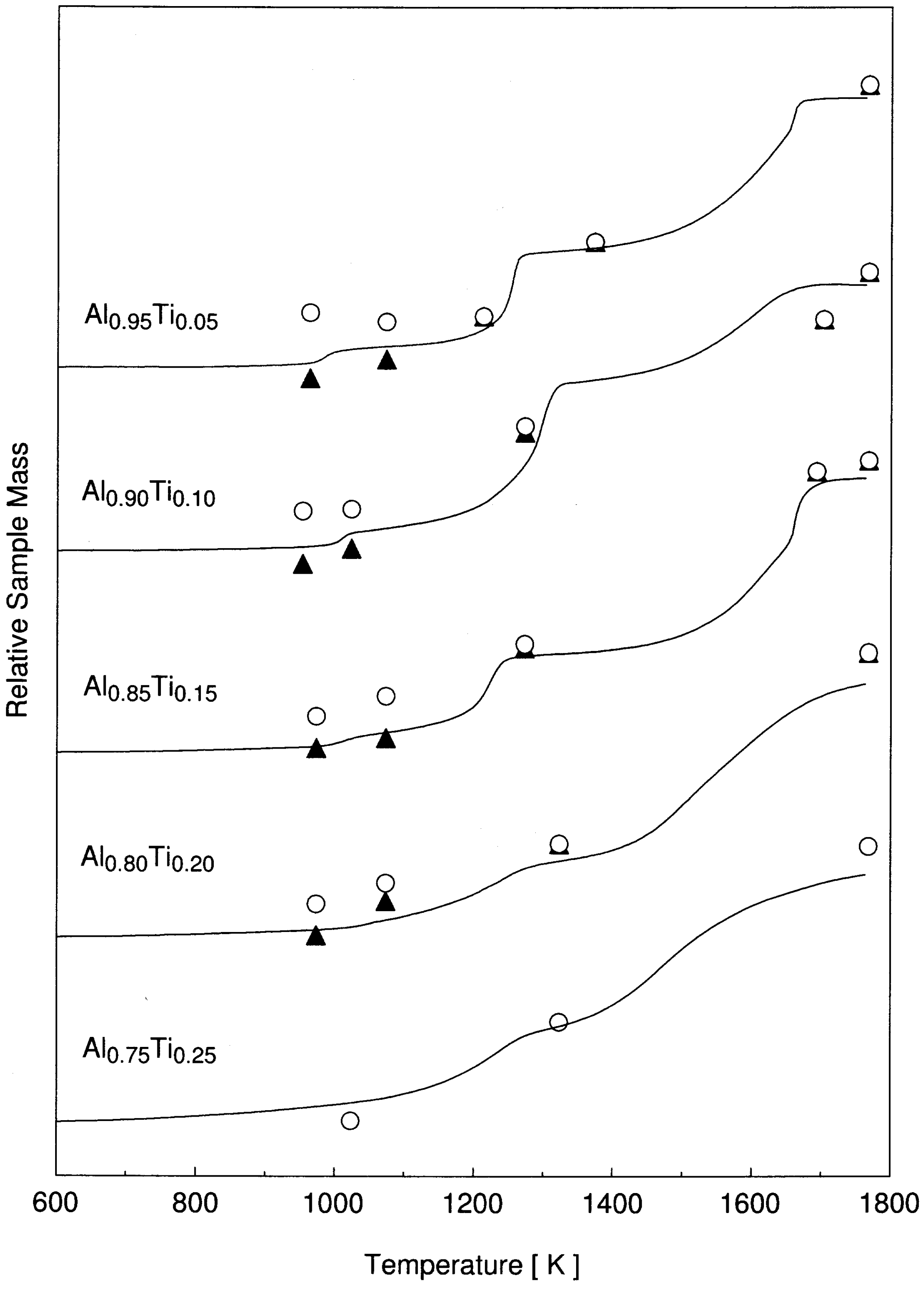

Figure 5.9 Comparison of weight changes as observed by TGA and as calculated from the quantitative XRD analysis assuming that the Al deficit exists as x-ray amorphous Al_2O_3 (open symbols), or as unoxidized Al (filled symbols).

Table 5.4 Molar Amount of Each Phase Relative to the Number of Atoms per Formula Unit

Composition	T(K)	Al_3Ti	Al	Al_4C_3	TiC	TiO_2	α-Al_2O_3	Al_2TiO_5	Al_4CO_4	**(Al)**	**(Ti)**	(Al_2O_3)
$Al_{0.95}Ti_{0.05}$	963	20.0	53.9	9.0						19.3		4.1
	1073	20.0	54.3	15.9			11.1			11.1		2.6
	1213	6.9	63.8	15.7	5.1		42.8				0.7	
	1373		48.9	7.9	8.8	0.5	103.8				0.4	
	1768		1.3	2.1	4.1	0.9	202.2	16.8	16.7		0.5	
$Al_{0.90}Ti_{0.10}$	953	40.0	42.0	0.9						15.8		4.2
	1023	15.5	59.4	5.4	12.2	-	6.7	-	-	11.9		3.1
	1273	0.8	47.1	-	18.8	1.3	100.7	-	-	2.1		
	1703	-	12.5	-	12.7	1.4	187.1	10.6	-		1.8	
	1768	-	0.8	-	4.2	1.6	194.2	46.4	-		1.5	
$Al_{0.85}Ti_{0.15}$	973	60.0	27.7	1.4						9.2		5.7
	1073	49.7	29.1		5.2		10.2			11.5		7.5
	1273	40.7	18.6		9.7		86.6			1.2		
	1693		1.9			8.1	167.5	64.5			4.2	
	1768					5.0	160.5	83.2			2.9	
$Al_{0.80}Ti_{0.20}$	973	80.0	8.9							8.4		6.9
	1073	64.3	13.2		7.8		30.4			6.4		
	1323	58.0	4.4		8.2	0.6	80.3				1.2	
	1768					5.2	124.6	120.6			3.2	
$Al_{0.75}Ti_{0.25}$	1023	100										
	1323	53.0			5.4	3.2	86.5	2.5			7.7	
	1768					5.0	91.9	152.9			4.2	

The reference quantity is 1 *mol* of unoxidized mechanical alloy $Al_xTi_{(1-x)}$. Deficit amounts are shown in parentheses

5.4.2 Oxidation

Using data from Table 5.4, it is possible to trace the evolution of different phases formed during oxidation. In this processing, assuming that both Al and Ti deficits have been properly attributed to metallic and oxide phases, total amounts of all the phases present can be calculated. Considering Table 5.4, one concludes that during the first oxidation event (around 973 K, see Figure 5.3), only aluminum oxide is produced. The amount of free metallic aluminum also increases as a result of partial decomposition of Al_3Ti. Decomposition of Al_3Ti accelerates dramatically by the end of the second oxidation event (around 1273 K, see Figure 5.3), however, only small amounts of oxidized titanium phases are observed. At the same time, large quantities of aluminum oxide are produced. Thus, the second oxidation event is also representative of aluminum oxidation. Further oxidation processes appear to include simultaneous continuing formation of Al_2O_3, TiO_2, and formation of the ternary Al_2TiO_5 oxides.

The metal oxidation processes are accompanied by the formation and following oxidation of aluminum carbides. As noted above, the carbon is introduced in the system from stearic acid used as PCA and it is likely that it is uniformly distributed within the initial mechanically alloyed particles. Products of oxidation of aluminum carbides are expected to be Al_2O_3 and CO_2 gas, while some carbon reacts with titanium, forming titanium carbide that remains relatively stable at elevated temperatures.

The stepwise oxidation observed for the Al-rich mechanical alloys is very similar to that observed for pure aluminum [77, 78]. The oxidation of aluminum is limited by the diffusion of species through the protective alumina film and different steps are observed when the diffusion resistance of the film changes as a result of polymorphic transformations in alumina. A similar scenario is expected for the oxidation of Al–Ti mechanical alloys, however, the sequence of the polymorphic phase changes could be altered. For example, the first oxidation step for aluminum is explained by the transformation of the natural amorphous alumina film into γ-Al_2O_3 nanocrystallites with higher density. This phase change destroys the continuity of the protective coverage of the aluminum surface due to the volume change of the oxide. Therefore, the oxidation rate accelerates while the openings produced in the oxide layer are healing. The stability range of amorphous alumina was shown to depend on the crystallographic orientation of the aluminum substrate [88]. Similarly, the presence of titanium is likely to affect this stability range and therefore, the first oxidation step for mechanical alloys could occur at a shifted temperature. Indeed, our observations indicate that the amorphous alumina is stabilized by the presence of titanium and the first oxidation step occurs at a temperature that is $\sim 150\,^{\circ}\mathrm{C}$ higher than that for pure aluminum (see Figure 5.3). Similarly to results with pure aluminum, the first oxidation step does not correlate with aluminum melting. The proposed mechanism for the first oxidation step is consistent with the γ-Al_2O_3 signatures found in the XRD patterns for the fine powders oxidized to 1073 K (Figure 5.7).

The second oxidation event resulting in a stepwise weight increase is also interpreted in analogy with the oxidation of pure aluminum. The growth of γ-Al_2O_3 accelerates at increased temperatures but is terminated by the formation of a stable α-Al_2O_3 oxide. This transformation is also accompanied by a significant density increase, formation of coarser crystallites, and decrease in the diffusion rate. Table 5.4 shows that no aluminum phases and specifically no oxides remain unaccounted for after the second oxidation event. The formation of α-Al_2O_3 is readily detected by XRD. By contrast, amorphous alumina cannot be detected and transition γ-Al_2O_3 produces broad and weak peaks that could not be well distinguished for most samples, or properly modeled for the quantitative XRD analysis. A significant difference of this process from the analogous process for pure aluminum oxidation is that in the mechanical alloys, fresh molten aluminum is continuously being generated as a result of Al_3Ti decomposition. Therefore, the rate of oxidation is also affected by the rate of aluminum production and is different from that for pure aluminum.

The third oxidation step is interpreted, similar to the pure aluminum oxidation, as the diffusion-limited growth of α-Al_2O_3. At the same time, such processes as formation of the ternary Al_2TiO_5 oxides and peritectic Al–Ti reactions occur in the same temperature range and affect the reaction kinetics.

The stepwise oxidation pattern becomes less visible with increased concentration of titanium. The first oxidation step completely disappears for the stoichiometric $Al_{0.75}Ti_{0.25}$ mechanical alloy which does not contain free aluminum before Al_3Ti decomposition at high temperatures. For this composition, any free aluminum that may be generated at higher temperatures is oxidized so that no metallic aluminum is found in the partially oxidized samples.

5.5 Summary

The oxidation of Al-rich mechanically alloyed Al–Ti powders was investigated by thermal analysis. Oxidation proceeds in three distinct steps, similar to the oxidation steps observed for pure Al. These oxidation steps are relatively sharp, but become more and more diffuse with increasing Ti concentration. Apparent activation energies have been determined for the more reproducible first and second oxidation steps for each alloy composition. For both first and second oxidation steps, the apparent activation energies are close to 400 kJ/mol. Partially oxidized powders were obtained and quantitative x-ray analysis was performed, confirming that Al_2O_3 and TiO_2 are the main reaction products. At higher temperatures, the ternary oxide Al_2TiO_5 forms, however, not as a product of direct oxidation. The presence of $\gamma - Al_2O_3$ in the samples after the first oxidation step was inferred from observed deviations of the calculated Al-Ti balance and confirmed by processing of selected XRD patterns. Based on the experimental results, it is proposed that overall oxidation mechanism of the Al-rich Al–Ti alloys prepared by MA is qualitatively similar to that of pure aluminum and is most notably affected by the polymorphic phase changes in the produced Al_2O_3 layers. Such phase changes affect the rates diffusion through protective Al_2O_3 layers which, in turn, control the oxidation rates. The ranges of stability of different Al_2O_3 polymorphs produced on the surface of alloys are changed compared to those for pure aluminum: specifically, the amorphous alumina is stabilized to the temperatures exceeding the melting point of aluminum. The oxidation rates are also affected by the intermetallic phase changes and formation of ternary Al_2TiO_5 oxides at elevated temperatures. Aluminum melting is not observed to affect the oxidation rate of the mechanically alloyed Al–Ti powders.

CHAPTER 6

IGNITION OF ALUMINUM–TITANIUM MECHANICAL ALLOYS ON ALUMINUM-RICH SIDE IN AIR

6.1 Introduction

Powders of metastable aluminum based alloys have been proposed as potential solid fuels in order to increase burn rates of aluminized propellants and other energetic formulations [33–35]. While the overall combustion enthalpy would not be affected significantly, the phase changes occurring on the metastable relaxation of such alloys were expected to accelerate the reaction kinetics [13, 35]. Feasibility tests have indeed shown higher burn rates for flames of aerosolized powders of several aluminum-based alloys (e.g., Al–Mg, Al–Ti, Al–Li, and Al–Zr) in air [33–35]. Such alloys typically include amorphous metallic phases or a supersaturated solid solution of an alloying element in aluminum. In addition, equilibrium intermetallic phases can be present. The exothermic phase changes occurring in such systems result in the decomposition of supersaturated solid solutions and formation of intermetallic phases. The enthalpy of such phase changes is much less than that of oxidation. However, it was hypothesized that if timed properly, this additional heat release could significantly accelerate ignition and as a result increase the global combustion rate.

Among several aluminum based alloys considered in previous preliminary work [37], particle combustion rates for aluminum-rich Al–Ti mechanical alloys were found to exceed most significantly the combustion rates of aluminum particles of similar size. Therefore, a more detailed study of this material system was warranted. Specifically, it was of interest to establish which of the phase transformations occurring in Al–Ti mechanical alloys upon heating would affect their ignition. A study of the phase changes in samples heated in argon was conducted using differential scanning calorimetry [56, 75]. The exothermic formation of metastable and equilibrium Al_3Ti phases was observed to occur in several steps. Exothermic subsolidus transformations resulting in the formation of the metastable $L1_2$ and $D0_{23}$ phases occurred in the range of $500 - 800\,K$. The stable $D0_{22}$ phase of Al_3Ti formed in the temperature range of $990 - 1040\,K$ above the eutectic melting of Al (935 K). A detailed description of the transitions leading to the formation of the stable $D0_{22}$ form of Al_3Ti is given in Ref. [56]. It was also clear that the oxidation mechanism of an Al–Ti mechanical alloy would differ from that of pure aluminum. Different alumina polymorphs, oxides of titanium, or ternary oxides form resulting in either slower or faster oxidation as compared to pure aluminum. To characterize the oxidation processes for such alloys, a thermo-gravimetric study combined with differential thermal analysis was carried out in which the mechanical alloy samples were heated in an oxygen flow [89, 90]. For Al-rich alloys, the oxidation proceeded stepwise. The thermal kinetics of the oxidation steps was not observed to correlate with the thermal kinetics of the exothermic phase changes in which Al_3Ti formed. Thus, when mechanically alloyed Al–Ti powders are heated in an oxidizing environment, their ignition is preceded or accompanied by three weakly exothermic transitions leading to the formation of increasingly stable Al_3Ti phases, while oxidation occurs concurrently in several distinct steps.

This part of the research is aimed to determine whether it is possible to identify the process governing ignition of the aluminum-rich Al–Ti mechanical alloys. The ignition in practical systems usually occurs at very high particle heating rates (e.g., $10^3 - 10^6\,K/s$) that exceed by far the typical heating rates of thermal analysis ($< 100\,K/min$). Therefore, the approach of this study was to study the kinetics of ignition of the Al–Ti mechanical alloys directly and compare the results to the

Table 6.1 Characterization of Particle Sizes of Synthesized Al-Ti Mechanical Alloys Using Low-Angle Laser Light Scattering

Alloy	Volume mean diameter, μm	Median diameter, μm	Standard deviation, μm
$Al_{0.90}Ti_{0.10}$	28.08	22.06	19.96
$Al_{0.85}Ti_{0.15}$	27.99	22.85	19.04
$Al_{0.80}Ti_{0.20}$	22.70	16.00	17.86
$Al_{0.75}Ti_{0.25}$	19.42	13.83	16.19

kinetics of the phase transitions and oxidation steps identified earlier by thermal analysis.

6.2 Materials

Aluminum-titanium mechanical alloys containing 10, 15, 20 and 25 at-% titanium were used in the experiments. The starting materials were elemental powders of Al (Alfa Aesar, 99.8 %, -40+325 mesh) and Ti (Alfa Aesar, 99 %, -325 mesh). The powders where mechanically alloyed for 15 hours using an 8000D series shaker mill by SPEX CertiPrep. The mechanical alloying was carried out within zirconia vials. The amount of powder used in the alloying cycle was 5 g and the total weight of milling media (3/8 inch diameter ZrO_2 balls) was 50 g, giving a ball to powder mass ratio of 10. Before alloying, 2 wt-% of a process control agent (stearic acid) was added.

The size distributions of the obtained powders were measured using a Beckman Coulter LS 230 laser diffraction particle size analyzer. The size distribution parameters including the volume mean particle sizes, median particle sizes, and standard deviations obtained for different powders, are shown in Table 6.1. Particle size distributions for different mechanical alloy compositions were qualitatively

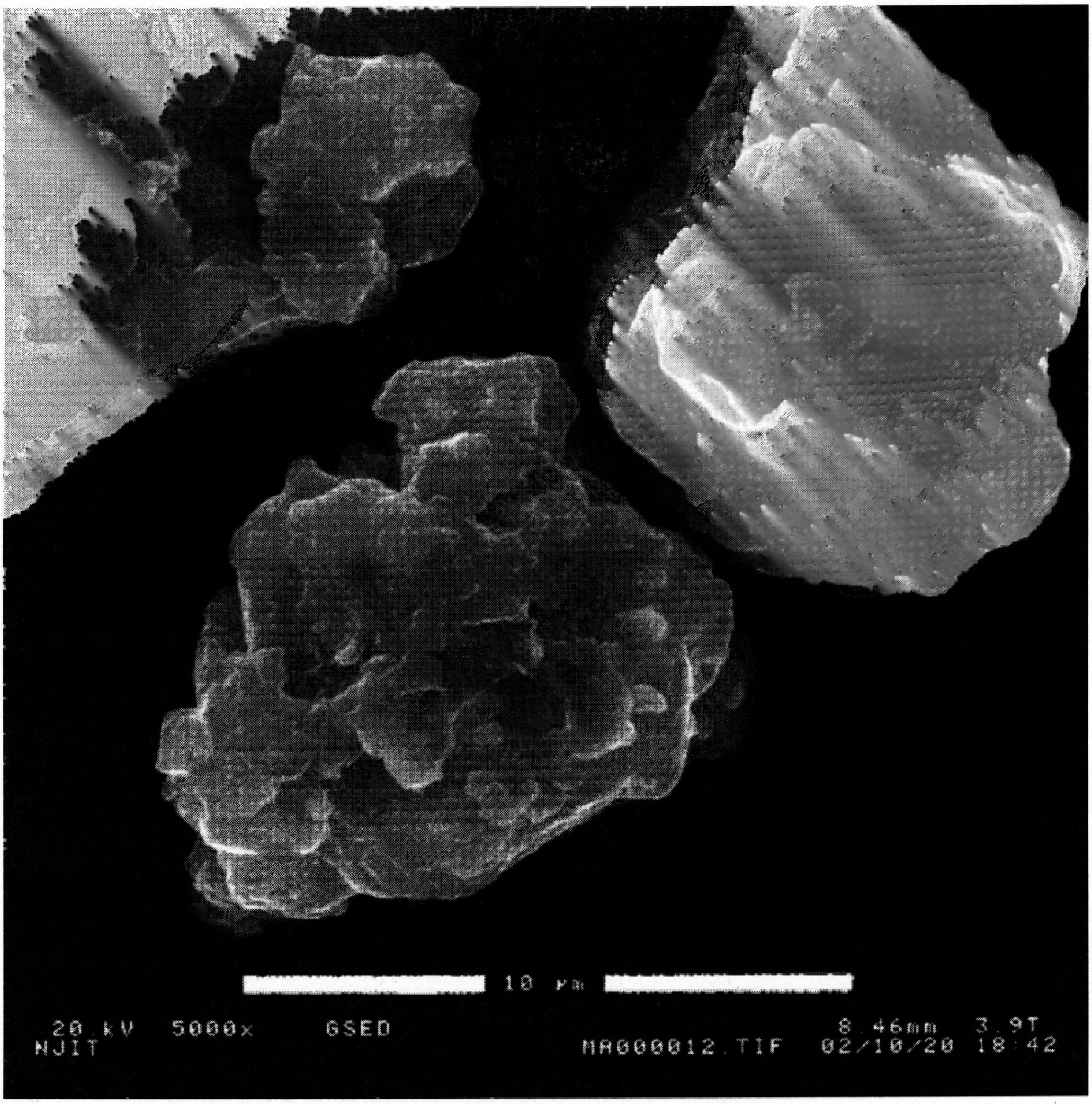

Figure 6.1 SEM image of $Al_{0.90}Ti_{0.10}$ mechanical alloy particles.

similar. Generally, the powders of alloys with higher titanium concentrations had slightly smaller particle sizes.

Particle morphologies were studied using an Electroscan Environmental Scanning Electron Microscope. Figure 6.1 shows a sample SEM image of Al–Ti alloy particles. Particles have irregular shape. The surface morphologies were similar for powders of different Al–Ti mechanical alloys.

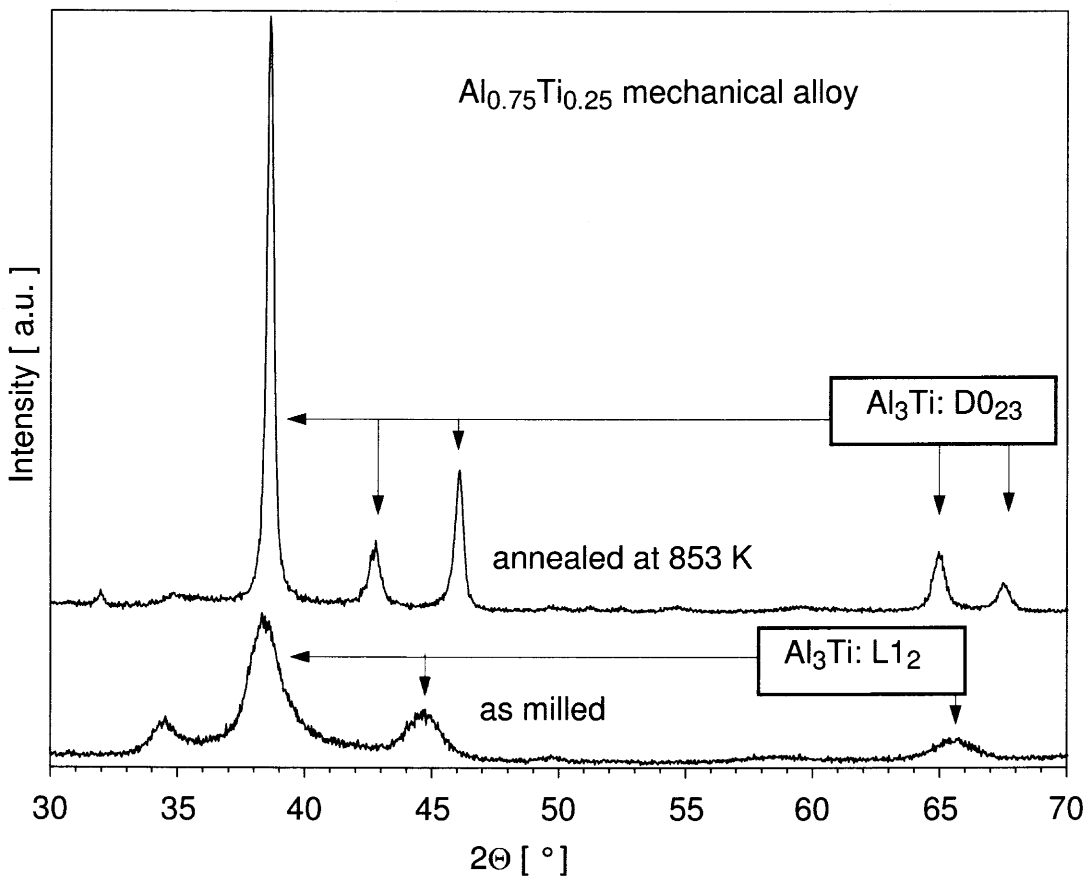

Figure 6.2 X-ray diffraction patterns of fresh (as milled) and annealed $Al_{0.75}Ti_{0.25}$ mechanical alloys.

The phase composition of the powders was analyzed using a Philips X'pert MRD diffractometer. For example, Figure 6.2 shows the x-ray diffraction (XRD) patterns for an as-milled $Al_{0.75}Ti_{0.25}$ mechanical alloy, and the same mechanical alloy annealed at 853 K. The fresh mechanical alloy consists of a primitive cubic phase similar to the metastable $L1_2$ phase of Al_3Ti. The annealed mechanical alloy consists of the $D0_{23}$ phase of Al_3Ti.

The experimental results described below suggested that subsolidus phase changes observed in thermal analysis and occurring between 500 and 800 K could play an important role for the ignition of Al–Ti mechanical alloys. Therefore, selected samples of mechanical alloys were annealed to 853 K to prepare materials in which

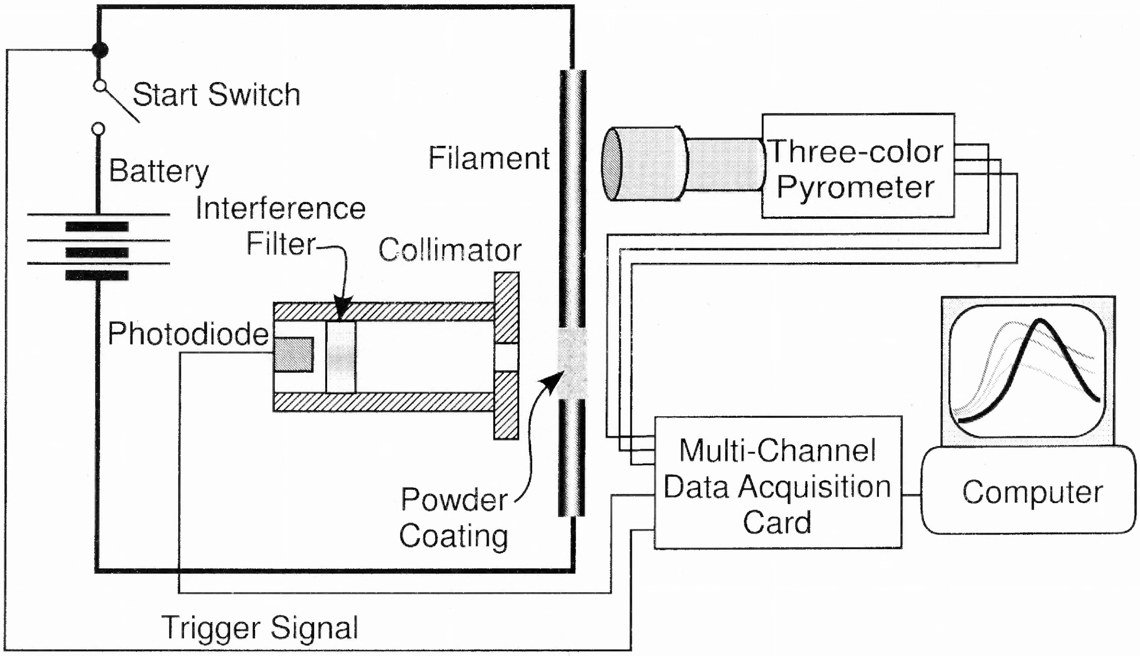

Figure 6.3 Schematic diagram of the setup used for ignition experiments.

no such changes would occur. These annealed samples were also used in ignition experiments, as described below.

6.3 Experimental

Figure 6.3 shows a schematic diagram of the experimental setup used in this research. The powders were ignited in air on the surface of an electrically heated metal filament. The filament heating rate could be readily controlled by changing the applied voltage or adjusting the current in the circuit. From experiments at different heating rates the kinetics of the observed ignition events could be established using a simplified Arrhenius-type analysis, similar to that used in differential thermal analysis. At the same time, the heating rates used in these experiments were of the order of $10^3 - 10^4$ K/s, much higher than those in thermal analysis, approaching the powder heating rates in practical combustion systems.

A 0.5 mm diameter nickel-chromium wire was used as filament. The total length of the heated filament was 4.5 cm, while only an approximately 1-cm long portion of its total length was coated with the powder to be ignited. A small amount of powder was mixed with ethanol and a thin layer of the slurry was deposited on the filament surface using a soft paintbrush. The coating was completely dried before the DC voltage was applied to heat the filament. To observe ignition, a silicon photodiode (DET110 by Thorlabs, Inc.) was focused on the coated portion of the filament. To minimize the effect of thermal radiation from the uncoated portion of the heated filament, the optical input of the photodiode was collimated using a blackened aluminum tube with an iris aperture. Simultaneously with the photodiode traces, the temperature history of the heated filament was measured using a high-speed, infrared pyrometer (DP1581 by Omega Engineering, Inc.) The pyrometer was focused on the uncoated surface of the filament adjacent to the powder coating. Thus, the temperature of the heated powder was not measured directly, but inferred from the measured filament temperature. The advantage of this approach was that the optical measurements were not affected by the potential differences in the powder emissivities that could result from different particle sizes, coating morphologies, or specific alloy compositions. A constant value of the filament emissivity, $\epsilon = 0.75$, which is an average emissivity for the Nichrome wire in the temperature range of $770 - 1270\,\mathrm{K}$ [91], was used consistently, independent of the powder coating. Thus, results of experiments with different powders could be compared against one another directly. At the same time, a systematic error similar for all the powders was introduced to the temperature measurements. This error was related to a small temperature difference between the powder and the heated filament. An estimate based on the heat transfer analysis for a single particle heated on the filament shows the particle temperature could be lower than the filament temperature by about 50 K.

However, the actual error is difficult to determine because it is strongly affected by the unknown thermal resistance of the contact between the particle and filament.

An estimated temperature profile along the heated filament indicated that the temperature gradients are negligible for its central portion used for the measurements. It was also assumed that a thin layer of powder did not affect the filament temperature, and therefore the temperature of the filament region covered by powder was very close to the measured temperature of the uncoated filament.

The DC voltage source was built using three 12V lead-acid batteries connected in series to produce 36 V DC. This limited the highest filament heating rate to about 2×10^4 K/s. One and two batteries connected in series producing 12 and 24 V DC, respectively, as well as a set of resistors were also used in experiments to achieve lower heating rates. The specific heating rates achieved in each experiment were determined from the recorded filament temperature histories.

Both the photodiode and pyrometer outputs were recorded using a PCI-MIO-16E-4 DAQ board by National Instruments, Inc., and a LabView-based digital oscilloscope. Reference photodiode traces produced by uncoated filaments were recorded for each voltage setting. The radiation traces obtained in these reference experiments were compared to the traces from the ignition experiments to identify qualitatively the signal features specific for the igniting powder.

The kinetics of most of the processes observed to occur during oxidation of the Al–Ti mechanical alloys were determined elsewhere [56, 75, 89, 90]. However, the measurements for the subsolidus phase changes occurring in the range of $500 - 800\,K$ were lacking. These measurements were performed using a Netzsch STA409-PC simultaneous thermal analyzer. Samples were contained in aluminum pans and the differential scanning calorimetry (DSC) experiments were performed in argon at heating rates of 5 and $40\,K/min$.

6.4 Data Processing for Ignition Experiments

Direct visual observation of the powders being heated on the filament clearly showed that the powders ignited and burned. A flame was clearly visible as well as smoke generated by the metal combustion. However, analysis of the recorded photodiode traces proved to be difficult. Whereas many qualitative differences could be found between the photodiode traces from the ignition experiments and reference traces recorded while heating uncoated filaments, it was difficult to select which specific signal feature would be attributed to ignition. The following section describes the procedure used to process the photodiode traces.

Time derivatives of "ignition" and reference radiation traces were found to be easier to work with; therefore, such derivatives were routinely produced. The recorded data files were numerically differentiated using PSI-Plot software by Poly Software International, Inc. Figure 6.4 shows examples of derivatives of the radiation traces for an ignition run and for a reference run performed with the same voltage settings. For brevity, such derivatives will be referred to as "radiation traces" or simply "traces." Temperature histories recorded in both, ignition and reference runs are also shown in Figure 6.4. The temperature traces nearly overlap, indicating good reproducibility between the experiments.

The reference and ignition radiation traces are quite different. Two peaks are observed on the ignition trace, while the reference trace shows a smoothly increasing signal. Finally, the rate of signal increase at about 0.22 s becomes much higher for the ignition trace as compared to the reference. As noted above, it was never obvious which of the peaks or other features, e.g., sharp increase in the signal, observed in the photodiode trace corresponded to ignition. Therefore, systematic analysis of the photodiode signal features observed for different powders and at different heating rates was necessary. For this analysis, the signal features were labeled as

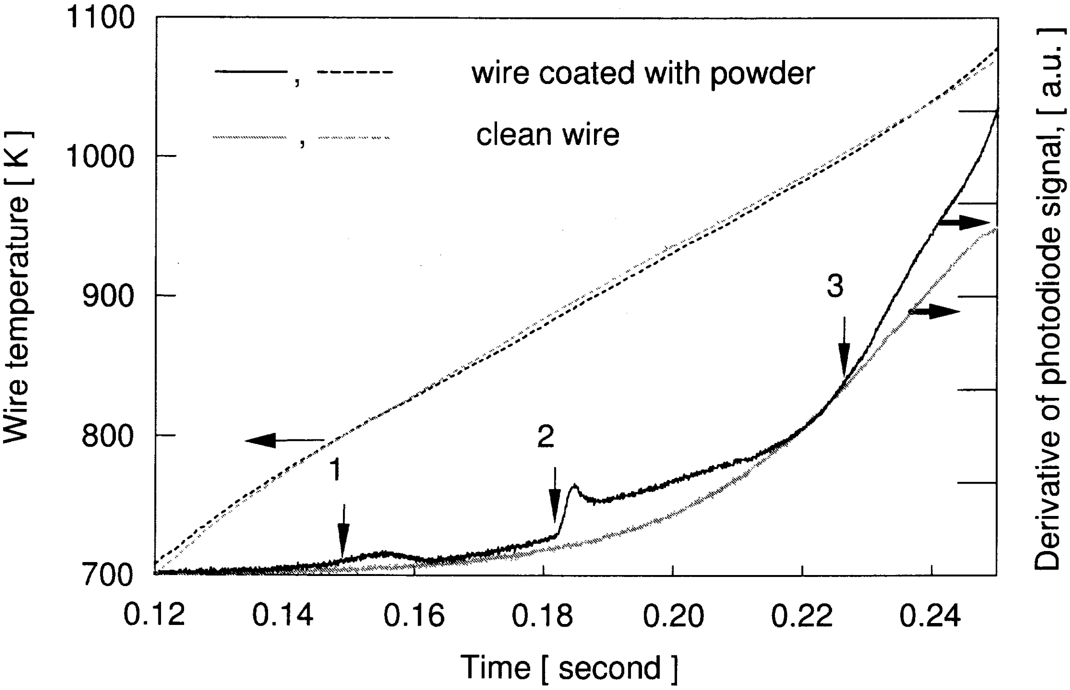

Figure 6.4 Recorded traces of the wire temperature (measured by pyrometer) and derivatives of photodiode signal recorded with and without powder coating (MA $Al_{0.75}Ti_{0.25}$). Heating rate is approximately 3×10^3 K/s. The onset points for the characteristic events are shown on the radiation traces.

events. Since a similar sequence of events was observed in earlier thermal analysis experiments, it was assumed that each signal feature corresponds to an identifiable physical transition occurring within the sample. As many as three events could be identified in many experiments, as in the example shown in Figure 6.4. The events were numbered in the order of their appearance during the filament heating, as illustrated in Figure 6.4. The onset temperature of each event was determined and tabulated as a result of data processing.

Figure 6.4 shows that the filament temperatures increased nearly linearly as a function of time. Therefore, the radiation signal could be plotted against the filament temperature instead of time while still illustrating the undistorted radiation signal history in these experiments. The plots of radiation versus temperature will be

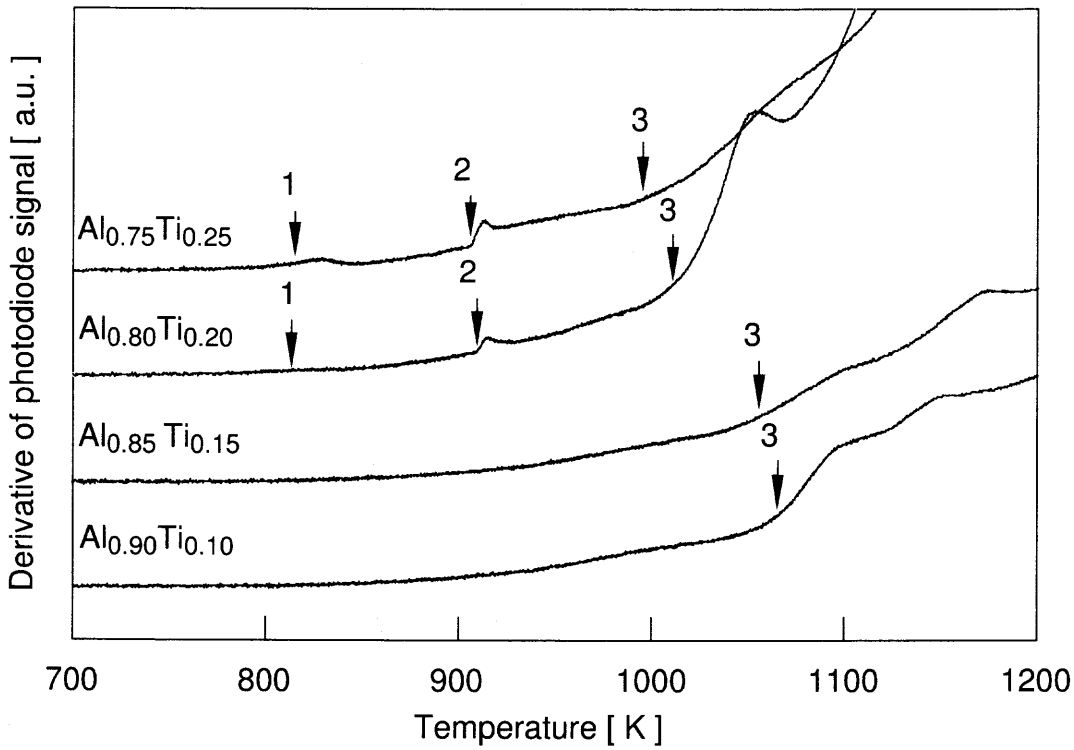

Figure 6.5 Derivatives of the photodiode signal as functions of the wire temperature for different Al–Ti mechanical alloys recoded at the same filament heating rate of 3000 K/s.

discussed below as more useful for the direct determination of the onset temperature for different events observed during filament heating.

6.5 Results

Typical radiation traces recorded in the ignition experiments with powders of different Al–Ti mechanical alloys are shown in Figure 6.5. All of the shown traces describe experiments conducted at the lowest pre-set filament heating rate ($3 \times 10^3\, K/s$). For the $Al_{0.75}Ti_{0.25}$ mechanical alloy powder, three events, similar to those observed in the example shown in Figure 6.4, are clearly visible. The first event is a weak peak at about $830\, K$. The second event is an asymmetric sharp peak observed just above $900\, K$. The third event is a rapid increase in the trace level starting just under $1000\, K$ and continuing throughout the rest of the experiment.

Oscillations in the photodiode traces could also be observed following the onset of the event 3. However, no repeatable pattern for these oscillations could be established. Thus, the high-temperature oscillations following the event 3 will not be discussed below.

For the alloy with a lower titanium concentration, $Al_{0.80}Ti_{0.20}$, the first peak labeled as event 1 was much weaker (but could be clearly distinguished with an expanded vertical scale.) It was identified as event 1 because its onset temperature was close to the corresponding temperatures for the event 1 always observed for the $Al_{0.75}Ti_{0.25}$ alloy. The photodiode trace features corresponding to the events 2 and 3 appeared similar to those for the $Al_{0.75}Ti_{0.25}$ alloy and occurred at close respective onset temperatures. The photodiode traces recorded at the lowest heating rate for the alloys with lower titanium concentrations, $Al_{0.85}Ti_{0.15}$ and $Al_{0.90}Ti_{0.10}$, exhibit only an increase in the signal occurring above 1000 K that is similar to the event 3 for the alloys with high titanium concentration.

The radiation traces changed as a function of the heating rate. The onset temperatures for different events shifted, enabling one to determine the respective kinetics. The peaks corresponding to different events could become more pronounced or indistinguishable. These observations are illustrated in Figure 6.6. A set of curves on top shows the evolution of the radiation traces for the $Al_{0.75}Ti_{0.25}$ mechanical alloy at different heating rates. As the heating rate increases, the onset of event 1 shifts towards higher temperatures. The amplitude of the respective peak does not change considerably. The onset temperature of event 2 also shifts to higher temperatures at increased heating rates. At the same time, the amplitude of the respective peak increases. In some experiments with $Al_{0.80}Ti_{0.20}$ and $Al_{0.75}Ti_{0.25}$ alloys, the increase in the peak amplitude for event 2 was dramatic and the photodiode output saturated. Such a sharp radiation increase could certainly be associated with the onset of

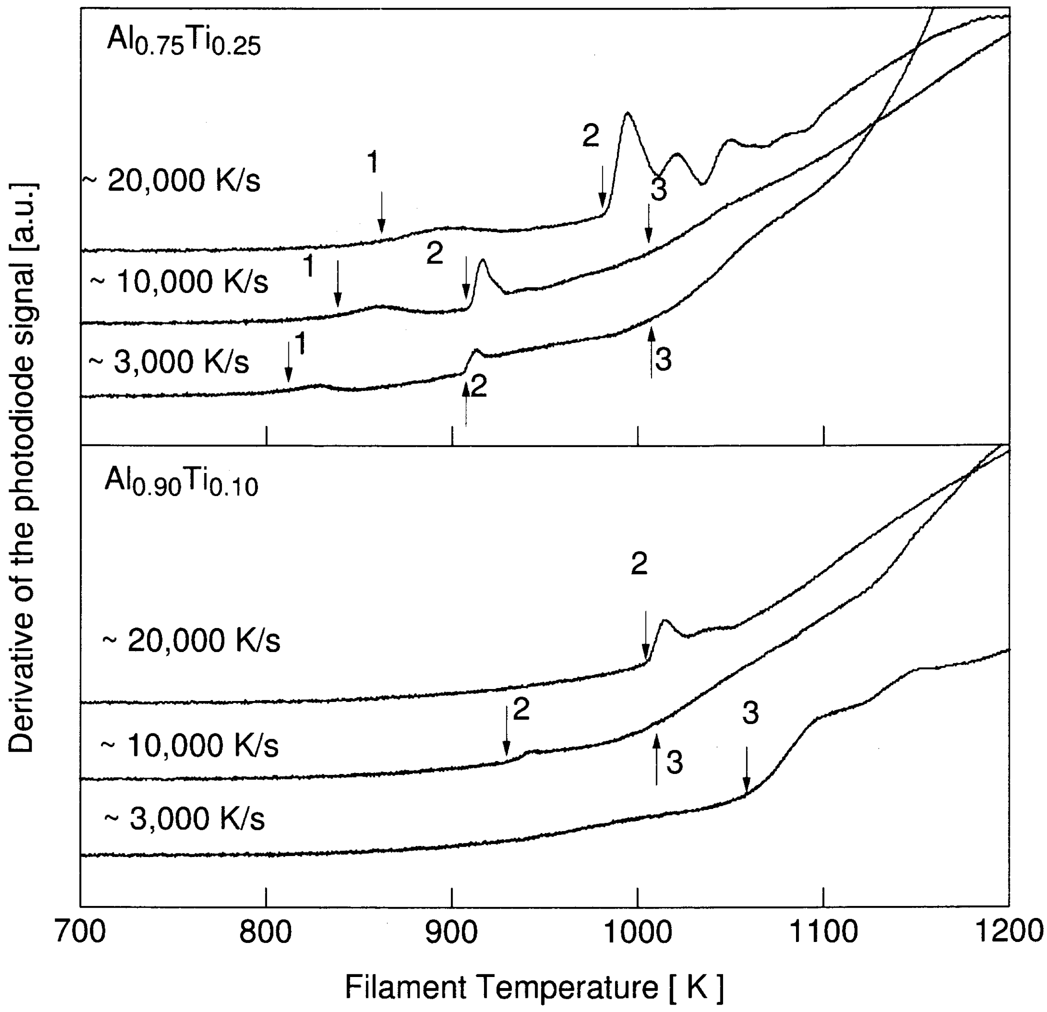

Figure 6.6 Evolution of the ignition traces as a function of the heating rate. Traces for the $Al_{0.75}Ti_{0.25}$ and $Al_{0.90}Ti_{0.10}$ mechanical alloys are shown.

combustion. Figure 6.7 shows a radiation trace recorded during one such run, for the $Al_{0.80}Ti_{0.20}$ alloy heated at a rate of about 10000 K/s. The inset in Figure 6.7 shows a magnified portion of the radiation trace showing that event 1 also occurred in this experiment, similar to the lower heating rates.

The high-temperature shift in the onset temperature of event 3 is less significant. In fact, analysis of many experiments did not show a consistent increase in the onset temperature of this event as a function of heating rate. At the highest

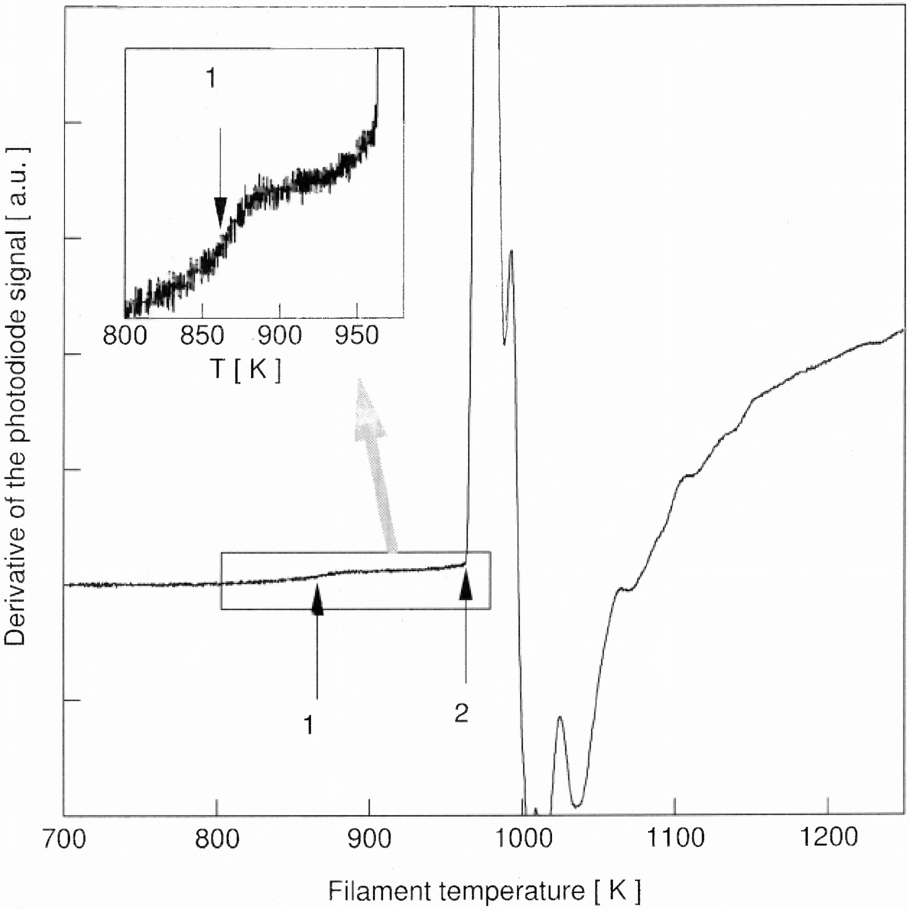

Figure 6.7 A radiation trace showing combustion of $Al_{0.80}Ti_{0.20}$ alloy triggered by event 2 at a heating rate of approximately 10^4 K/s. The inset shows a magnified portion of the radiation trace to show event 1.

heating rate, it becomes impossible to identify the onset of event 3 because of overlaps with the radiation peak corresponding to event 2.

The set of curves at the bottom part of Figure 6.6 shows the evolution of radiation traces for the $Al_{0.90}Ti_{0.10}$ mechanical alloy. The characteristic asymmetric peak corresponding to event 2 becomes clearly visible at increased heating rates. Its onset temperature becomes higher at higher heating rates, and its amplitude increases. This behavior is consistent with that described above for the $Al_{0.75}Ti_{0.25}$ alloy. Event 3 can be identified for all heating rates. Its onset temperature remains

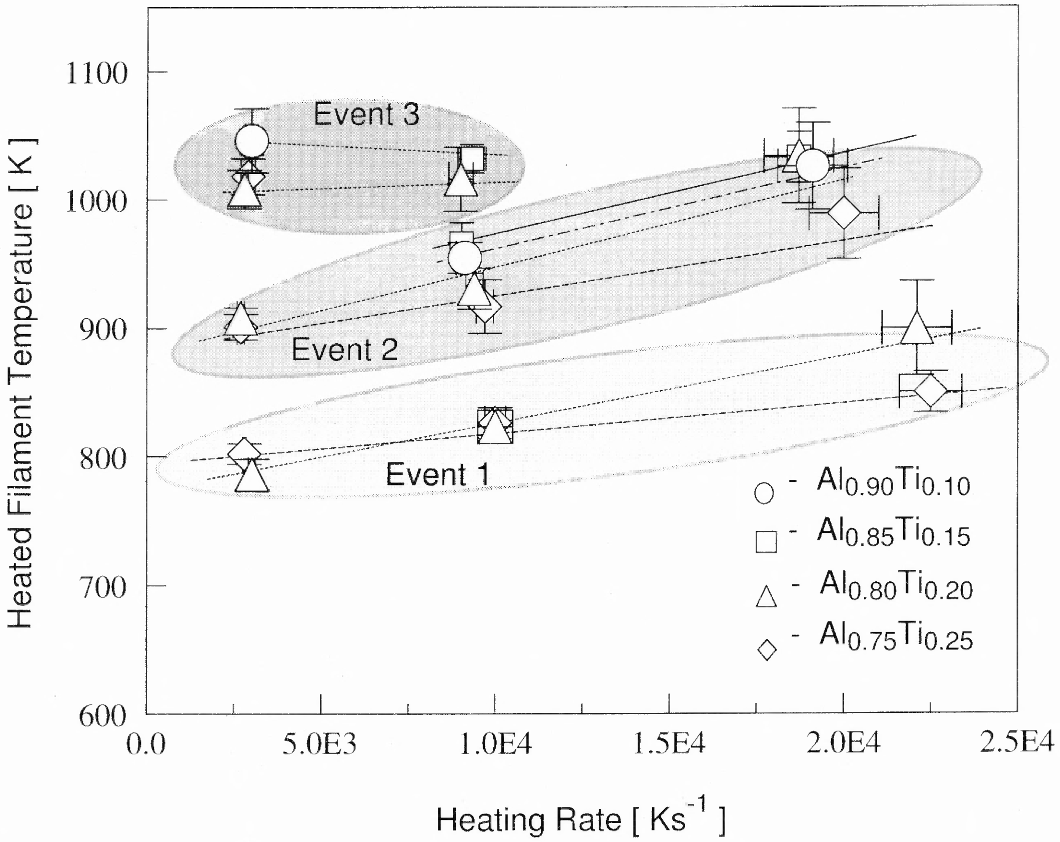

Figure 6.8 Onset temperatures for different events observed in ignition traces as a function of the heating rate.

almost the same at different heating rates, which is consistent with the trend observed for the $Al_{0.75}Ti_{0.25}$ alloy.

A summary of the identified onset temperatures for different events observed in the radiation traces at different heating rates is shown in Figure 6.8. Different symbols are assigned to different alloys. The three sets of points grouped in the plot correspond to the three events identified in the radiation traces. As described above, event 1 was observed consistently only for the $Al_{0.80}Ti_{0.20}$ and $Al_{0.75}Ti_{0.25}$ mechanical alloys. Event 2 was observed for all the alloys. Event 3 could be separated from event 2 only at lower heating rates.

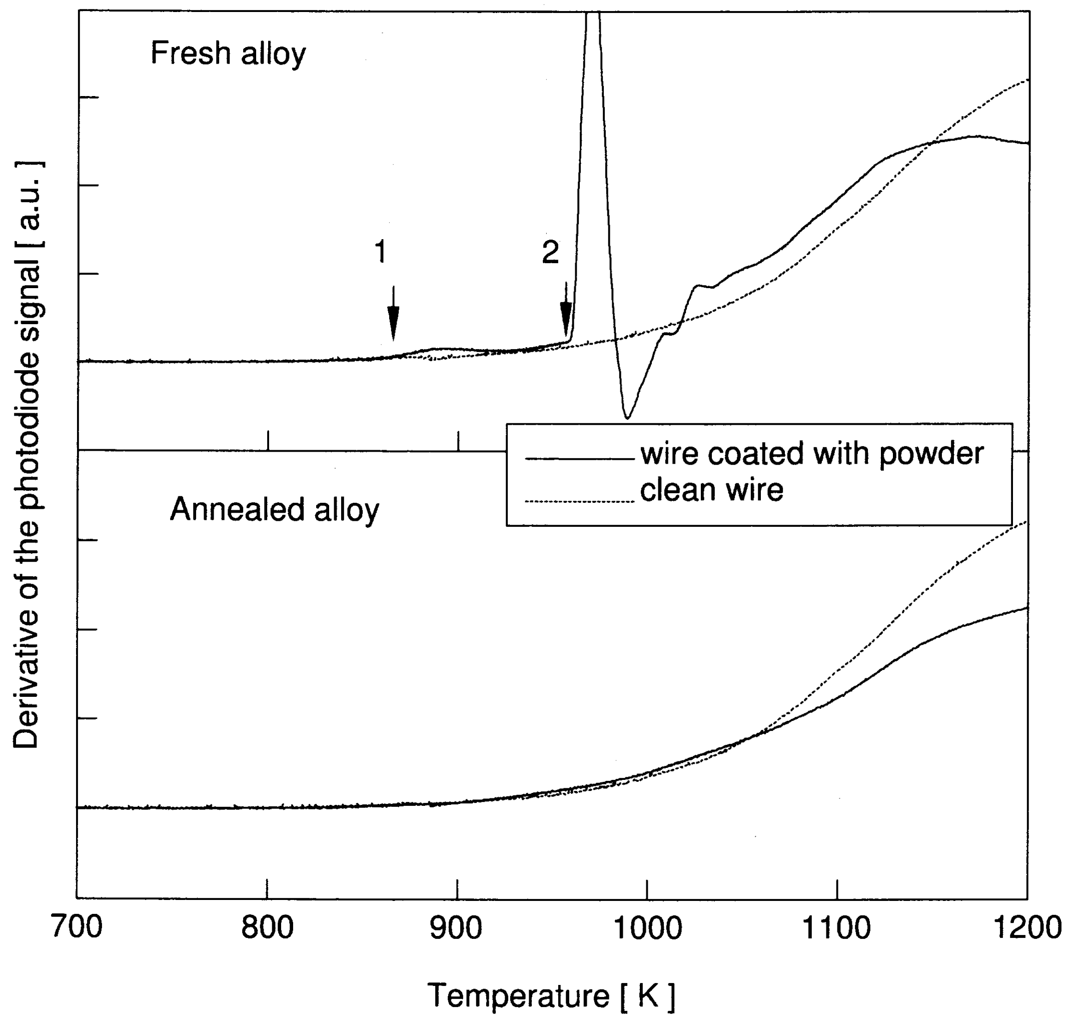

Figure 6.9 Effect of annealing on the $Al_{0.75}Ti_{0.25}$ alloy radiation traces. The heating rate is 10^4 K/s.

The effect of powder annealing on its ignition behavior is illustrated in Figure 6.9. For this experiment, mechanical alloy $Al_{0.75}Ti_{0.25}$ was heated in argon atmosphere in the thermal analyzer up to 853 K. This annealing temperature was selected to avoid the effect of all subsolidus phase changes on the ignition of the annealed powder. The radiation trace for the annealed powder (Figure 6.9) shows that neither event 1, 2, or 3 is observed. Thus, ignition could not be identified within the temperature range of 700 – 1100 K achievable using the heated nickel-chromium

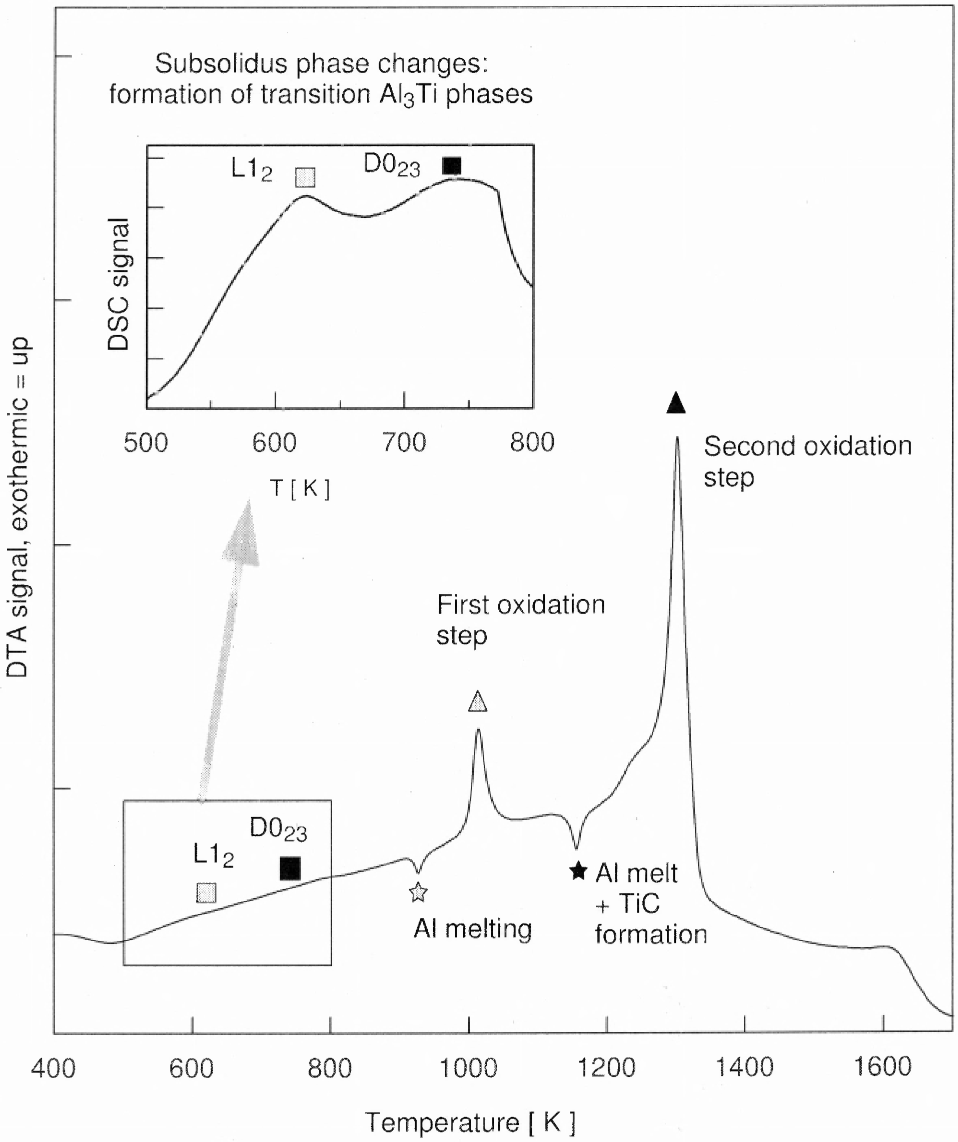

Figure 6.10 DTA and DSC traces for mechanically alloyed powder $Al_{0.90}Ti_{0.10}$. The heating rate is 15 K/min. Specific phase changes and oxidation steps determined elsewhere [47, 56, 75, 89, 90] are labeled.

filament. The interpretation of this observation is that the powder annealing has dramatically increased its ignition temperature.

The results of the differential thermal analysis (DTA) and DSC experiments are illustrated in Figure 6.10. The inset shows an example of a DSC measurement for the low-temperature phase changes. The main curve in Figure 6.10 is a characteristic

Table 6.2 Temperatures of Formation of Transition Al_3Ti Phases Measured by DSC at Different Heating Rates

Alloy	Heating rate, K/s	Peak temperature of formation of Al_3Ti phases, K	
		$L1_2$	$D0_{23}$
$Al_{0.90}Ti_{0.10}$	0.083	584	624
	0.667	660	740
$Al_{0.85}Ti_{0.15}$	0.083	591	623
	0.667	751	805
$Al_{0.80}Ti_{0.20}$	0.083	589	630
	0.667	758	794
$Al_{0.75}Ti_{0.25}$	0.083	584	641
	0.667	722	767

DTA curve of $Al_{0.90}Ti_{0.10}$ mechanical alloy heated in oxygen flow [89, 90]. Each peak is labeled to assign the respective phase change or oxidation step identified in the earlier work [47, 56, 75, 89, 90] and in the DSC measurements presented here. The onset temperature for the two identified subsolidus phase changes determined for different heating rates are shown in Table. 6.2.

6.6 Discussion

6.6.1 Identification of Ignition

A systematic analysis of the recorded radiation traces shows that event 1 is an unlikely ignition trigger. It produces a weak peak consistently observed only for the $Al_{0.80}Ti_{0.20}$ and $Al_{0.75}Ti_{0.25}$ mechanical alloys, while all of the alloys were observed to ignite at all the heating rates used. Therefore, ignition was triggered by either event 2 or event 3. At higher heating rates, events 2 and 3 essentially merged and the amplitude of the peak corresponding to event 2 increased rapidly. Because the heating rates in most practical systems are even higher than used in this research, it is expected that event 2 would be further amplified and result in a strong temperature jump. Thus, it is suggested that the onset of the radiation peak corresponding to event 2 should be considered as ignition for these practical systems. Respectively, to predict the ignition temperature of an Al–Ti mechanical alloy, the kinetics of event 2 should be determined.

6.6.2 Phase Changes Corresponding to the Observed Ignition

To establish which of the observed phase changes or oxidation steps affect ignition during heating of the Al–Ti mechanical alloys, the thermal kinetics of the processes studied by thermal analysis [56, 75, 89, 90] were compared to the kinetics of different events determined from the radiation traces in these ignition tests. An overview of processes occurring in a sample heated in oxidizing environment and identifiable from the thermal analysis is presented in Figure 6.10. The two endothermic peaks are equilibrium phase changes, i.e., aluminum melting at 933 K and decomposition of aluminum carbide with the formation of aluminum melt and titanium carbide occurring in the vicinity of 1170 K [75]. Note that carbon is present as a contamination in the mechanically alloyed powders because of the use of stearic acid as a process control agent [75]. Two strong exothermic peaks, around 1020 and 1300 K, represent the two oxidation steps. Two weak exothermic peaks observed between 600 and 800 K represent the formation of the metastable Al_3Ti phases $L1_2$ and $D0_{23}$. The third exothermic peak corresponding to the formation of the stable $D0_{22}$ phase of Al_3Ti overlapped with the second oxidation step for the experiments in oxidizing environments, and so it could not be separated as shown in Figure 6.10.

While it was suggested above that event 2 is the most likely ignition trigger, all of the events identified in the radiation traces were considered. These comparisons are illustrated in Figures 6.11a – d. For each mechanical alloy, a set of Arrhenius plots is presented showing the inverse characteristic temperatures for each of the observed phase changes and oxidation steps as a function of the logarithm of heating rate. The same plot also includes the inverse temperatures corresponding to the onset of characteristic events from the ignition radiation traces. Note that the heating rates of the ignition experiments are much higher than those of thermal analyses. The temperature measurements in the ignition experiments are also less accurate. As mentioned above, these temperatures are likely to include a noticeable systematic error (up to $50\,K$) because the measured filament temperature is likely to be somewhat higher than the temperature of the heated powder. Thus, an exact match between the kinetic trends for the wire ignition experiments and thermal analysis could not be expected. However, the comparison is still instructive. If the phase changes or oxidation steps trigger ignition, the extrapolation of the respective Arrhenius trends to high heating rates should point to the range of the expected ignition temperatures.

Subsolidus transformations resulting in the formation of the $L1_2$ and $D0_{23}$ phases of Al_3Ti were observed for all the alloy compositions, as shown in Figures 6.11a – d. However, the equilibrium melting of Al was only observed for $Al_{0.90}Ti_{0.10}$ and $Al_{0.85}Ti_{0.15}$ alloys (cf. Figures 6.11a and b). Only one oxidation step was observed for the $Al_{0.75}Ti_{0.25}$ alloy, as shown in Figure 6.11d. For all the compositions, the Arrhenius trends for the oxidation steps occurring above the aluminum eutectic melting temperature extrapolated to high heating rates, point to temperatures that are higher than the experimental temperatures at which event leading to ignition are observed. The differences between the temperature ranges expected based on the oxidation kinetics and the temperatures at which ignition events are identified are especially significant for the $Al_{0.85}Ti_{0.15}$, $Al_{0.80}Ti_{0.20}$, and $Al_{0.75}Ti_{0.25}$ compositions (Figure 6.11b, c, and d, respectively). On the other hand, as shown in Figure 6.11, for each alloy the Arrhenius trend for the subsolidus exothermic formation of the $L1_2$ phase of Al_3Ti is extrapolated to a region that is very close to the onset temperatures for the events identified from the radiation traces in the ignition tests. Specifically, the extrapolated Arrhenius line comes close to the temperatures corresponding to the onset of the event 2, suggested to trigger ignition. The possible systematic error in temperature measurements for ignition tests discussed above could shift the inverse temperatures corresponding to the ignition events to the right side of the plot in Figure 6.11. This would make the match between the event 2 temperatures and the extrapolated Arrhenius plot for the first subsolidus phase change even better for the $Al_{0.90}Ti_{0.10}$, $Al_{0.85}Ti_{0.15}$, and $Al_{0.80}Ti_{0.20}$ alloys. Therefore, the kinetic comparison suggests that the exothermic formation of a transition phase of Al_3Ti is likely to be the ignition trigger for the Al–Ti mechanical alloys. The enthalpy of formation of these transition phases does not exceed 10 kJ/mol [45, 56], which is much less than the metal oxidation enthalpy. Thus, the particle ignition can only be triggered if the effects of the exothermic phase changes and oxidation are coupled. A plausible mechanism is that the heat released due to the beginning exothermic phase change raises the particle temperature so that the rates of both the phase transition and oxidation are increased, which leads to ignition.

The expected temperature of the eutectic melting (endothermic) peak also happens to be in the vicinity of the temperatures at which ignition events are observed. However, melting is not observed for the alloys with high titanium concentration, while the ignition events remain qualitatively similar. Also, the melting temperature does not change as a function of the heating rate, unlike the onset temperatures for both the event 2 in the radiation traces and the phase transition producing a metastable Al_3Ti phase.

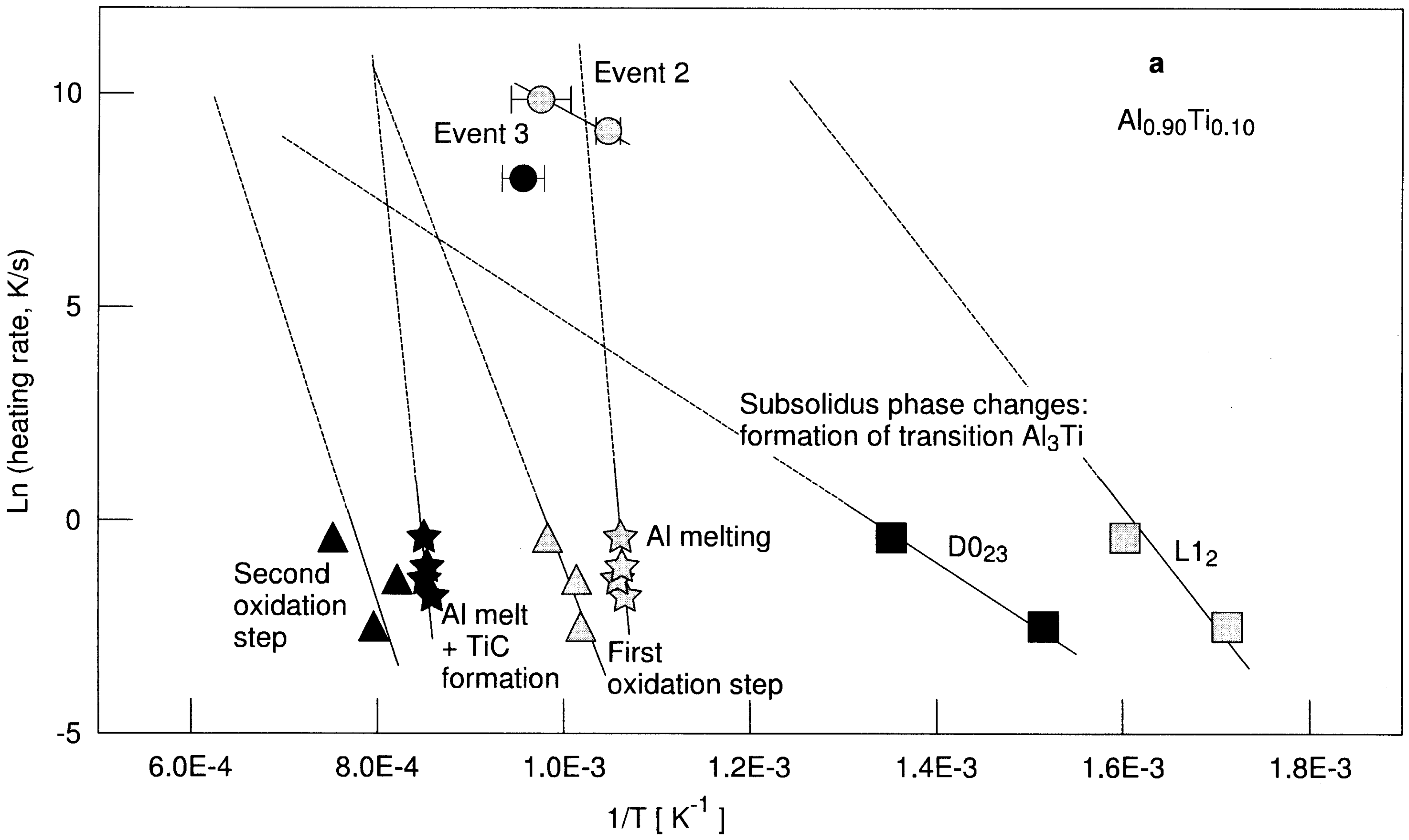

Figure 6.11a Arrhenius plots for thermal analysis data and for events in ignition experiments for different Al–Ti mechanical alloys. ($Al_{0.90}Ti_{0.10}$)

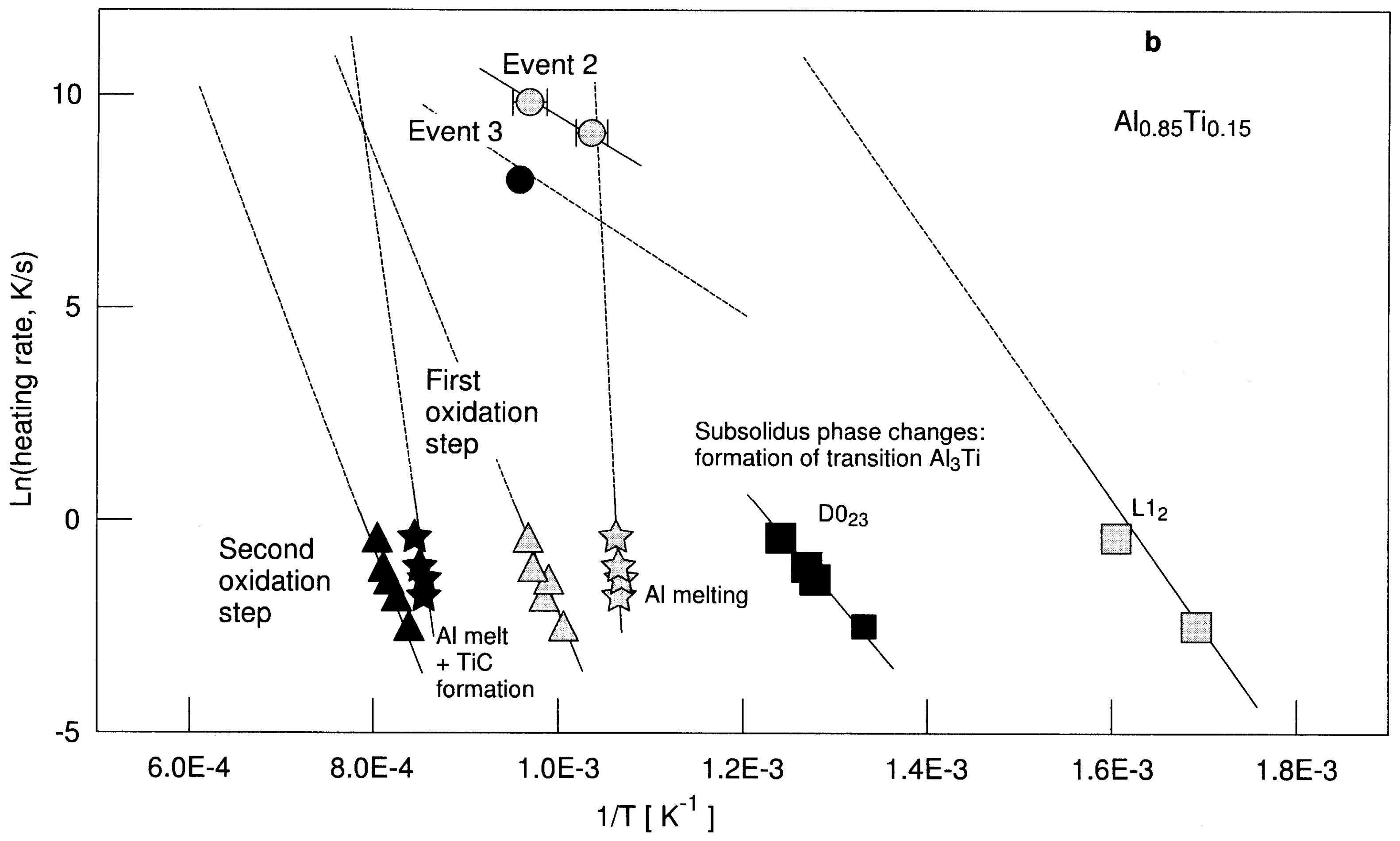

Figure 6.11b Arrhenius plots for thermal analysis data and for events in ignition experiments for different Al–Ti mechanical alloys. ($Al_{0.85}Ti_{0.15}$)

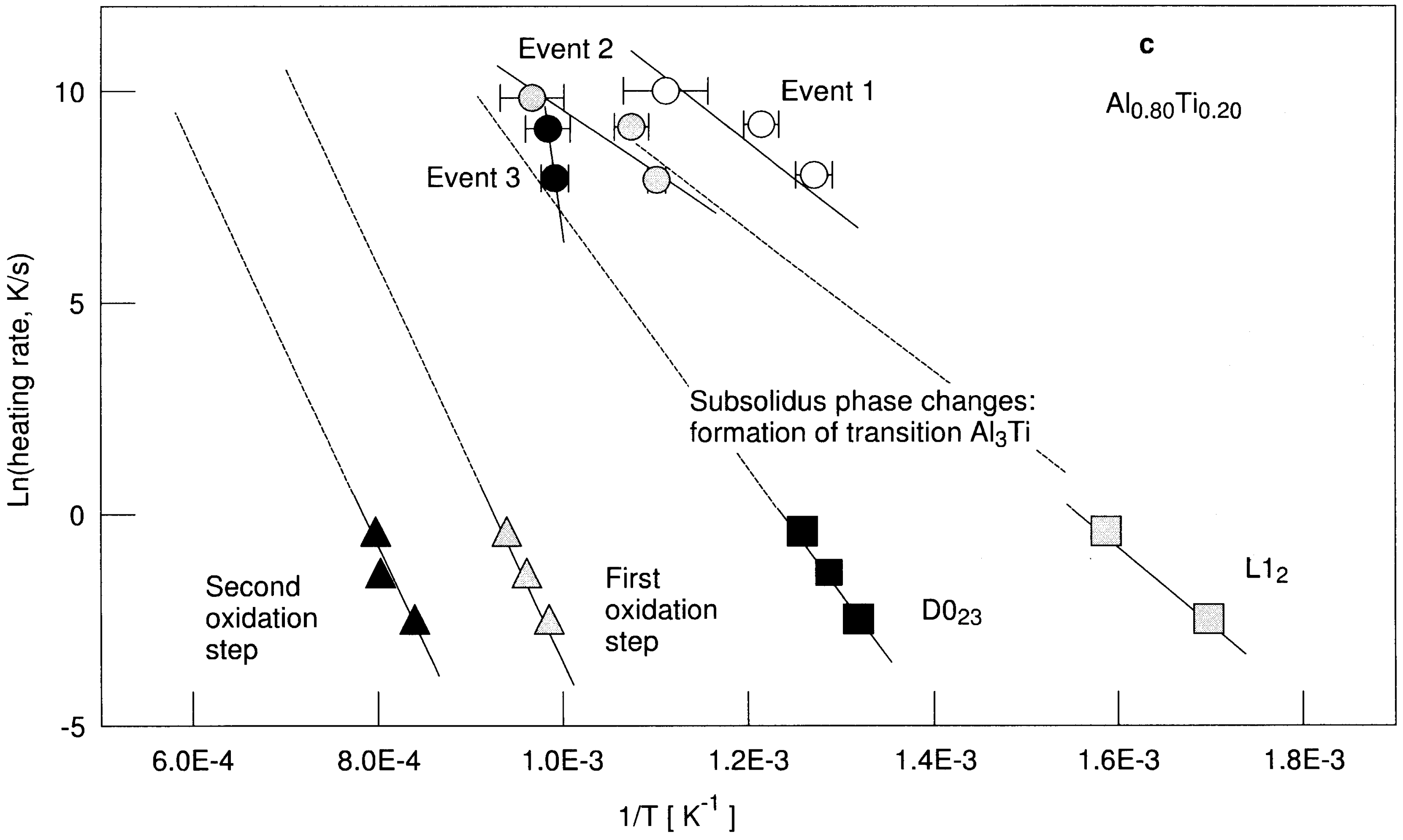

Figure 6.11c Arrhenius plots for thermal analysis data and for events in ignition experiments for different Al–Ti mechanical alloys. ($Al_{0.80}Ti_{0.20}$)

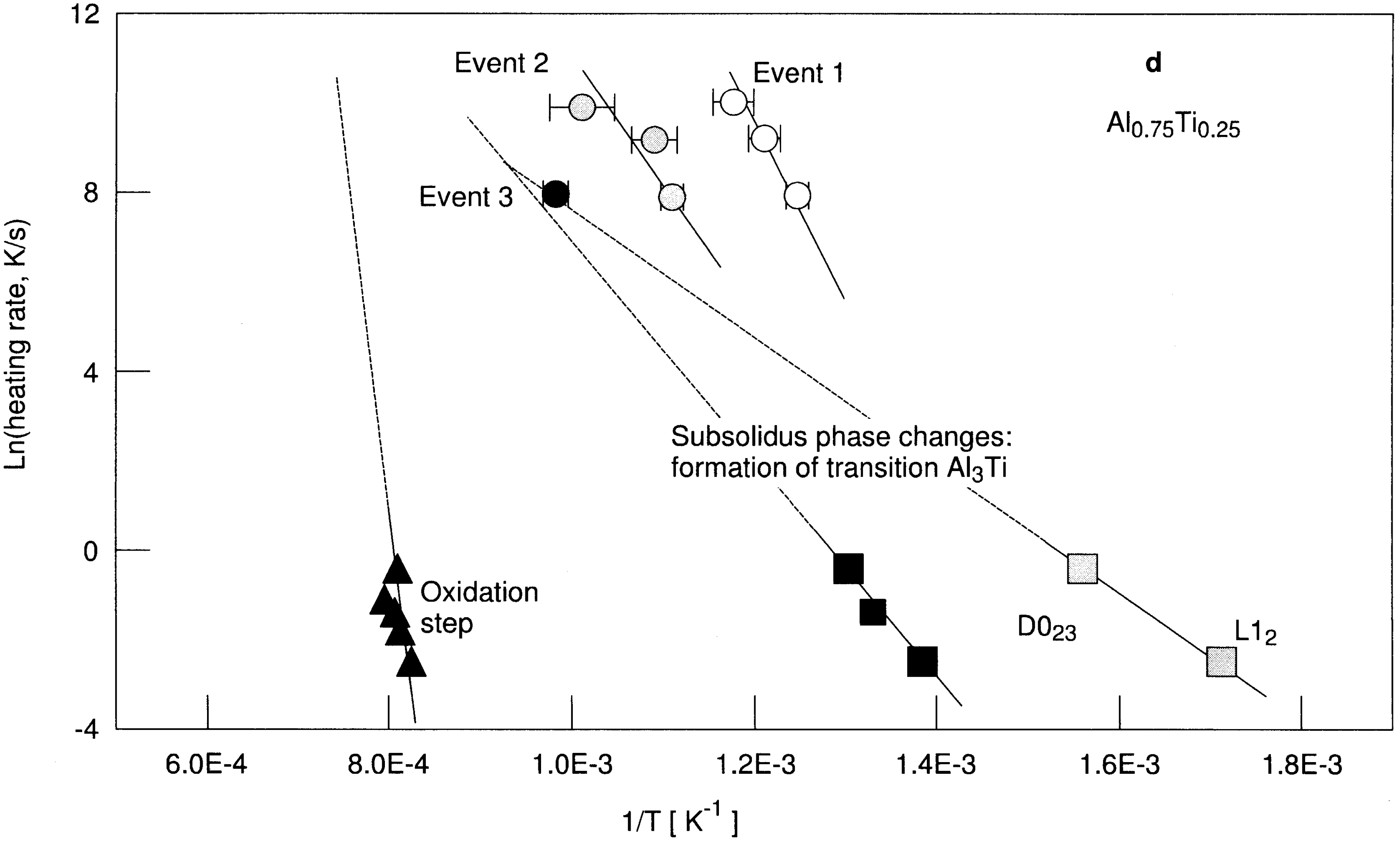

Figure 6.11d Arrhenius plots for thermal analysis data and for events in ignition experiments for different Al–Ti mechanical alloys. ($Al_{0.75}Ti_{0.25}$)

The crucial role of the phase changes resulting in the formation of metastable Al_3Ti phases as an ignition trigger for the Al–Ti mechanical alloys is further supported by the experiments with annealed powders. When the metastable Al_3Ti phases are formed prior to the ignition experiments, the events observed in the radiation traces and associated with the low-temperature ignition disappear.

Note that the assignment of the events 1 and 3 observed in the ignition experiments is not straightforward. Event 1 corresponds to a process occurring at even lower temperature than the first detected subsolidus phase change producing the $L1_2$ phase. However, the DSC peak measured in these experiments is fairly broad and could include several overlapping processes. It is conceivable that these processes could be better resolved at very high heating rates typical for the ignition experiments. Event 3 does not seem to depend on the heating rate, which could indicate that it is associated with melting. However, this assessment is inconsistent with the absence of aluminum melting for the $Al_{0.75}Ti_{0.25}$ alloy, for which event 3 is still occurring. Further experiments would be needed to identify the nature of these two events observed in these ignition experiments.

6.6.3 Ignition Temperatures of Al–Ti Mechanical Alloy Powders in Practical Systems

In practical combustion systems, heating rates can be even higher than those achieved in the present experiments. To predict the respective ignition temperatures, an Arrhenius trend-line can be produced for each alloy using an expanded range of heating rates by connecting the onset temperatures determined at different heating rates for the first peak of the subsolidus Al_3Ti formation and event 2 (the most significant peak) from the ignition experiments. The resulting trends for all alloy compositions are shown in Figure 6.12. This method of data processing is based on the assumption that both event 2 and the subsolidus phase change are associated with the same ignition trigger. The ignition temperatures expected in a practical system can now be evaluated by extrapolating the found trend-line to the heating rates of interest. For example, in a lifted laminar flame burner described in Refs. [33, 37,92], the particle heating rate is estimated to be $10^6\ K/s$. Arrhenius plots for each of the Al–Ti mechanical alloys are extrapolated to high heating rates as shown in Figure 6.12. A filled symbol on each line corresponds to the heating rate of $10^6\ K/s$ and indicates the inverse of the ignition temperature expected for the respective alloy in the lifted flame burner. This result can be used in the analysis of experimental data describing the flames of the Al–Ti mechanical alloy powders.

6.7 Summary

Ignition of metastable Al–Ti mechanical alloys was investigated experimentally using an electrically heated filament. Radiation traces produced by the igniting powders were analyzed. A characteristic peak on the radiation trace corresponding to the powder ignition was identified and the kinetic relations of this and other observed peaks were investigated. Comparison of the characteristic temperatures and kinetics for the characteristic peaks in the radiation traces versus phase changes and oxidation steps determined by thermal analysis, showed that the exothermic formation of the metastable $L1_2$ phase of Al_3Ti triggers ignition in the Al–Ti mechanical alloys. This conclusion was confirmed by additional ignition experiments in which annealed mechanical alloys already containing the transition Al_3Ti phase did not ignite in the same temperature range as fresh mechanical alloys.

Assuming that the kinetics of the exothermic formation of the $L1_2$ structure of Al_3Ti and of the ignition onset are identical, the ignition temperatures for different Al–Ti mechanical alloys can be predicted for wide ranges of experimental heating rates.

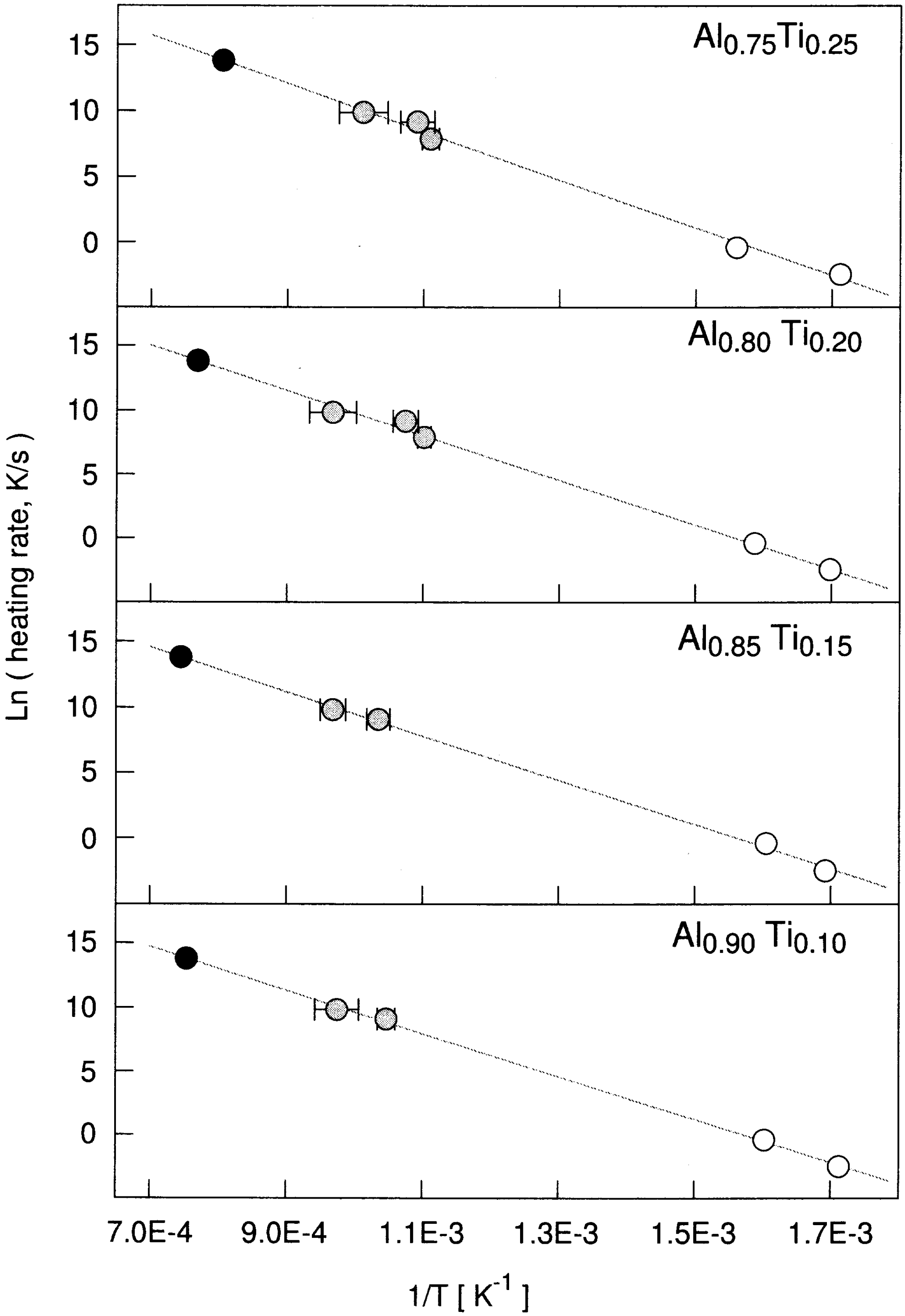

Figure 6.12 Arrhenius plots of ignition kinetics extrapolated to higher heating rates for different Al–Ti mechanical alloys. Open symbols show the results of thermal analysis corresponding to the formation of $L1_2$ phase of Al_3Ti. Grey symbols show the results of the ignition experiments using an electrically heated filament (event 2). Black symbols show estimated ignition temperatures for the laminar lifted flame experiments [33,37,92] for which the heating rate is estimated to be $10^6\ K/s$.

CHAPTER 7

SCALE UP PRODUCTION OF ALUMINUM–TITANIUM POWDERS BY MECHANICAL ALLOYING

7.1 Introduction

Al–Ti reactive alloys are of interest for a number of specific applications, including thermobaric explosives and reactive structural materials [93–95]. Because of the discovered effect of phase change on the ignition kinetics, it was suggested that materials with higher concentrations of Ti would be advantageous. In addition, higher concentrations of Ti lead to higher densities, which are of interest for applications in reactive fragments and related weapons components [96–98]. Therefore, the bulk composition of $2Al + Ti$ was selected for this specific study. Based on the previous results, the exothermic formation of intermetallic phases from the mechanically alloyed metastable solid solutions leads to ignition. Thus, the practical goal of this effort was to prepare kilogram quantities of mechanically alloyed powders in which the exothermic formation of intermetallic phases readily occurs. The approach was to use a higher throughput process and establish the shortest milling time necessary for preparation of a metastable material undergoing an exothermic relaxation process leading to its ignition while being heated.

7.2 Experimental

7.2.1 Initial Setup for Synthesis

Pure Al (Alfa Aesar, 98 %, $10-14\,\mu$m) and Ti (Alfa Aesar, 99 %, -325 mesh) powders were used as starting materials. These materials are the same as those used earlier. Instead of a shaker mill, a planetary ball mill, Retsch PM400, was used to provide a higher throughput. The batch size could be increased by a factor of about 20. Steel vials and steel balls were used; batches of 100 g materials were milled under Ar atmosphere. Balls were 12 mm in diameter, with a ball-to-powder mass ratio of 3. These milling parameters were selected to maintain the maximum of 300 g of balls loaded per milling vial in addition to 100 g of powder. It was noticed in preliminary tests that the ball mill does not operate adequately with the larger loads. When the per-vial loads exceed 400 g, the rate of vial rotations is no longer maintained and the mill occasionally stops indicating an operational error. Two weight percent of stearic acid ($(CH_3 - (CH_2)_{16} - COOH)$ were added as PCA during milling.

7.2.2 Sampling during Milling Process and Ignition Testing

All the samples described in the previous chapters (Chapter 3, 4, 5, and 6), were made using a shaker mill. In many experiments, samples were observed to cake during milling. An overall trend noticed was that the samples with the higher Ti concentrations tend to cake more readily. Clearly, caking reduces the milling efficiency and results in the annealing of the partially milled powders. Therefore, it should be avoided when metastable reactive materials are produced.

As noted above, the composition of $Al_{0.67}Ti_{0.33}(Al_2Ti)$ was chosen for these larger scale material manufacturing experiments. The concentration of Ti for this composition is higher than was ever used in our earlier experiments. Therefore, it was expected that caking would become a significant issue that would need to be dealt with. The milling experiments were set up so that the samples were examined every three hours. The milling was interrupted and the vials were opened and inspected inside the glove box, under protective Ar atmosphere. Small samples for the subsequent analyses were also collected when the vials were opened. Two vials were opened at a time. No caking was observed for the vials opened after 3, 6, 9,

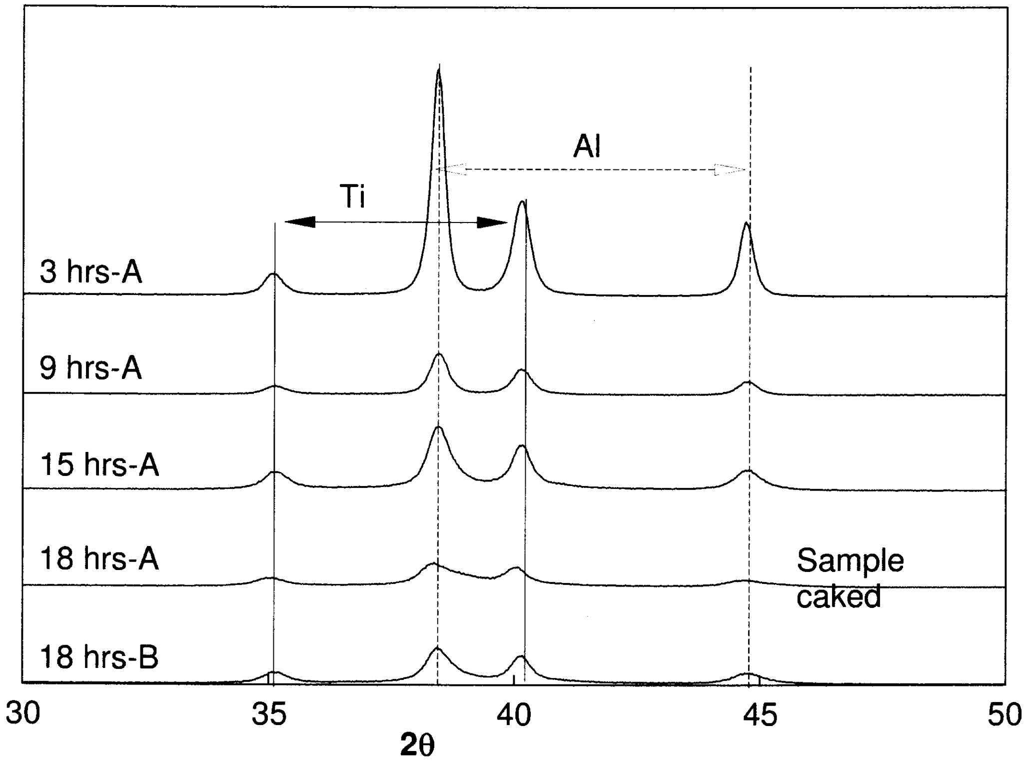

Figure 7.1 XRD patterns for the samples milled for different times. The labels indicate which vials were opened (A or B) and the milling times

12, and 15 hours of milling. The experiment was stopped after 18 hours of milling, when the samples in two vials were found to be heavily caked. At the same time, no caking was observed in the other two vials after the same milling time.

XRD patterns were collected for all the recovered samples. Ignition experiments using a heated filament were performed according to the methodology described in Chapter 6. The results are presented and discussed below.

7.3 Results

7.3.1 Collected XRD Patterns

XRD patterns for the samples collected at different milling times are shown in Figure 7.1. Titanium and aluminum peaks are clearly observed for all the samples.

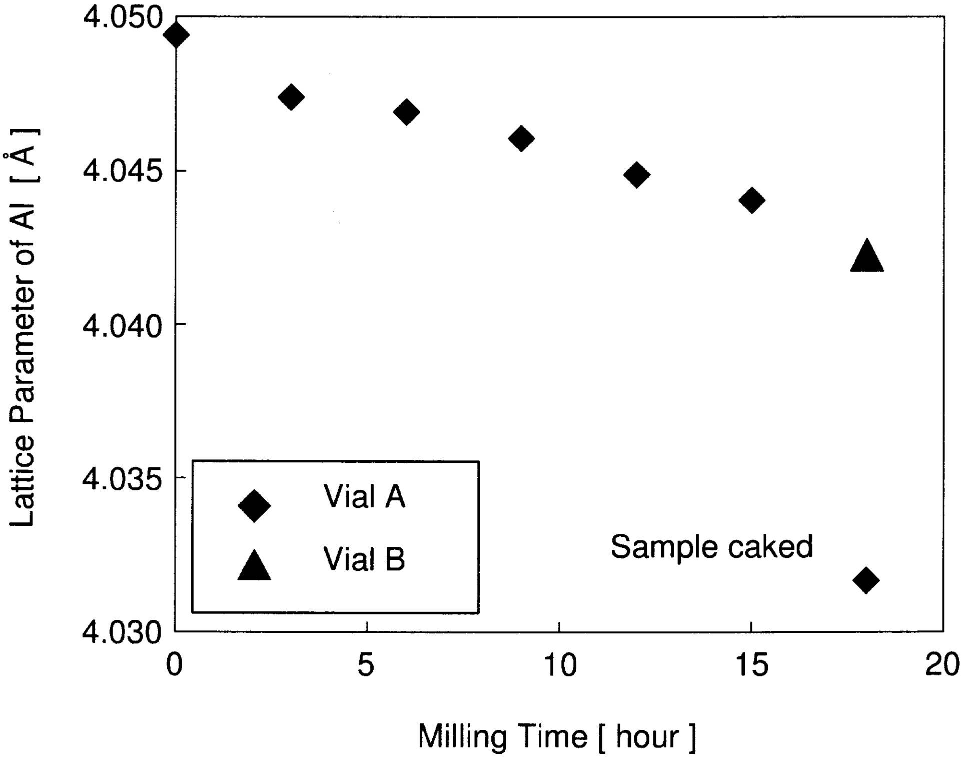

Figure 7.2 Lattice parameters of Al phase with milling time.

The peaks broaden and their intensity generally decreases with the increased milling times. The peak positions also shift, indicating a change in the crystal lattice parameter. Such a change is usually occurring when solid solutions form. The collected patterns were processed using a whole pattern refinement software (GSAS, introduced in Chapter 5). The changes in the lattice parameter of aluminum as a function of milling time are plotted in Figure 7.2. The lattice parameter continuously decreases with milling time. However, for the sample that was caked, the inferred lattice parameter decreases abruptly. This most likely indicates the formation of an intermetallic phase that affects the data processing in which only the two original phases (Al and Ti) are considered.

7.3.2 Ignition Results

The methodology used in the ignition experiments was described in detail earlier (Chapter 6). The experiments were performed at the heating rate close to 5000 K/s. The experiments were performed with the powders collected after different milling times. In addition, experiments were performed with the pure Ti powders used as a starting material for the milling. The characteristic ignition traces measured for mechanically alloyed powders are shown in Figure 7.3. To better distinguish exothermic events, the time derivative of the photodiode signal is shown, as discussed in detail above (*cf.* Chapter 6) For reference, a trace measured for a blank wire (with no powder coating) is also shown. This trace served as the baseline enabling one to better identify and detect events leading to ignition. For the sample milled for 3 hours, the first exothermic event detectable from the recorded trace occurs at about 1303 K. This temperature is very close to the measured ignition temperature of pure Ti powder. No effects of the exothermic relaxation processes on the measured ignition trace are detected. These measurements indicate that after 3 hours of milling, the material generally remains unalloyed and behaves as the intimately mixed elemental Al and Ti powders.

For the sample milled during 15 hours, the first exothermic event is observed to occur at a substantially lower temperature of about 1188 K. This event is followed by a broader peak occurring at about 1273 K. The recorded trace for the caked sample shows a generally similar behavior, while the exothermic events are broader and somewhat hard to resolve. The peak observed in the ignition trace around 1173 K is likely to be due to the expected exothermic formation of intermetallic phases. Thus, the measured ignition trace for the sample milled for 15 hours shows that mechanical alloying was sufficiently long to produce the amount of metastable solution necessary for accelerated ignition triggering. This milling time was, therefore, selected as

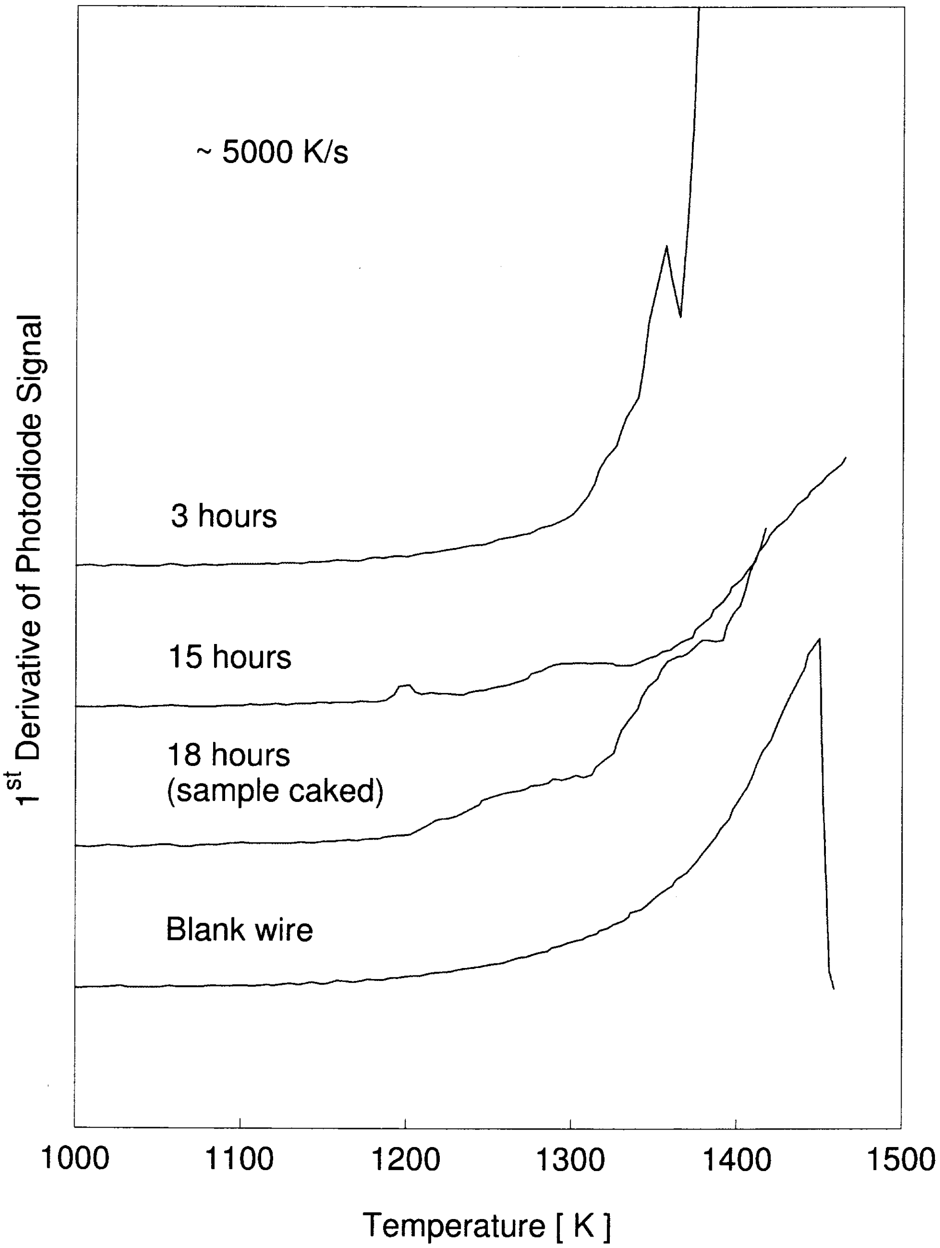

Figure 7.3 Derivative of the photodiode signal focused on the powder igniting on top of a heated filament. The results are shown for mechanically alloyed Al_2Ti powders collected after different milling times.

appropriate for preparation of initial samples suitable for testing as high-density reactive energetic materials.

7.4 Summary

It has been experimentally verified that a planetary mill can be used as well as a shaker mill to produce metastable, mechanically alloyed powders in the Al-Ti system. Powders with the bulk composition $Al_{0.67}Ti_{0.33}$(Al_2Ti) have been synthesized with the batch size of 100 g (per vial). The XRD analysis showed that the material structure was being continuously refined at increased milling times. The decrease in the aluminum lattice parameter at increased milling times was interpreted to show a continuous formation of a metastable solid solution. The maximum milling time at which the caking does not occur was found to be acceptable to produce mechanically alloyed powders for which ignition is triggered by the exothermic relaxation of metastable phases and formation of intermetallics.

CHAPTER 8

MECHANICALLY ALLOYED ALUMINIUM-LITHIUM POWDERS

8.1 Introduction

Al–Li cast alloys have been extensively used in structural applications due to their good mechanical properties and low density [99,100]. Mechanical alloying (MA) has been used to improve the ductility of ternary Al–Li alloys [101,102]. Typically, low concentrations of lithium in the structural alloys are maintained to ensure stability during exposure to air. However, powders of Al-based alloys with increased concentrations of Li are attractive as high energy density fuels or additives to metallized propellants [103,104]. Such materials are expected to be more reactive than pure Al, which is most commonly added to energetic materials. Several related Al-based alloys were recently prepared by MA [36,56], a low temperature process that is well suited for the production of reactive powders on a practical scale. In this work, mechanically alloyed Al–Li powders were produced with 30 at-% (10 wt-%) of lithium. The progress of mechanical alloying was assessed by collection and characterization of powders at different milling times.

8.2 Experimental

8.2.1 Synthesis

The mechanical alloys were prepared in a Retsch PM 400 MA planetary mill which has been modified for these experiments. An air conditioner was used to maintain the temperature in the milling chamber at about 288 K and custom-made finned aluminum heat sinks were mounted on the milling vials to enhance the rate of convective heat transfer. Temperature sensors were mounted on top of the milling vials (Point Sensor Thermistor including 418 MHz transmitters by Point Six Wireless, Inc.). The maximum vial temperature during the synthesis did not exceed 313 K with the heat sinks installed, compared to about 333 K without the heat sinks. Batches of 30 g were prepared in steel milling jars using steel milling media (10 mm diameter balls). The ball-to-powder weight ratio was 10, and 4 mass % of stearic acid was added as a process control agent. Sample caking was observed in some cases. To increase the milling effectiveness, the sample vials were opened periodically, and any caked samples were manually broken apart. All sample handling was performed in a glove box under protective argon atmosphere.

Starting materials were Al powder, 99.8 % pure, −40 +325 mesh by Alfa Aesar, and a 0.75 mm thick, 45 mm wide, 99.9 % pure lithium ribbon by Sigma–Aldrich. The milling process was monitored by taking samples at certain intervals and collecting X-ray diffraction patterns. Two synthesis runs were performed, for 102 and 68 hours, respectively.

8.2.2 Characterization

Powder morphology and compositional homogeneity was analyzed using scanning electron microscopy. A LEO 1530 Field Emission Scanning Electron Microscope (SEM) equipped with an integrated Energy Dispersive X-ray (EDX) spectrometer was used.

Compositional and phase analyses of the materials were based on the results of powder x-ray diffraction (XRD) measurements performed using a Philips X'pert MRD X-ray Diffractometer operated at 45 kV and 40 mA, using Cu-Kα radiation ($\lambda = 1.5438$ Å). To avoid exposing the mechanically alloyed powders to air, samples were mounted as a suspension in vacuum oil on a low-background single crystal quartz plate. The XRD patterns were processed using a PDF-4 Materials database and analyzed quantitatively using the GSAS whole pattern refinement software [76].

Particle size distributions were measured by low angle laser light scattering using a Beckman-Coulter LS230 Enhanced Particle Analyzer. Suspensions for the measurements were prepared in kerosene to avoid reaction of the alloy particles with the fluid.

The thermal stability was studied by Differential Scanning Calorimetry (DSC) and Thermo-Gravimetric Analysis (TGA) using a Netzsch Simultaneous Thermal Analyzer STA409 PC. The measurements were performed in inert atmosphere (Ar) in order to characterize the relaxation of the metastable, mechanically alloyed powder to form equilibrium phases. The air-sensitive samples were transferred from storage vials to the open DSC sample pans as a suspension in hexane. After closing the calorimeter, the protective fluid was evaporated under Ar before starting the heating program.

8.3 Results

8.3.1 SEM/EDX and Particle Size Distribution

A typical SEM image of the mechanically alloyed powder is shown in Figure 8.1. The particle morphology is characteristic of other mechanically alloyed powders, while the sizes of individual particles are fairly small. Elemental analysis performed using EDX showed the presence of about 5 at-% contamination by iron, likely introduced by the steel milling balls and milling containers.

The results of the particle size distribution measurements for the mechanically alloyed powder (processing time 102 hours) are illustrated in Figure 8.2. The volumetric mean size is 11.25 μm. To invert the light scattering data to the size distribution, a Mie type optical model was constructed, using the complex refractive

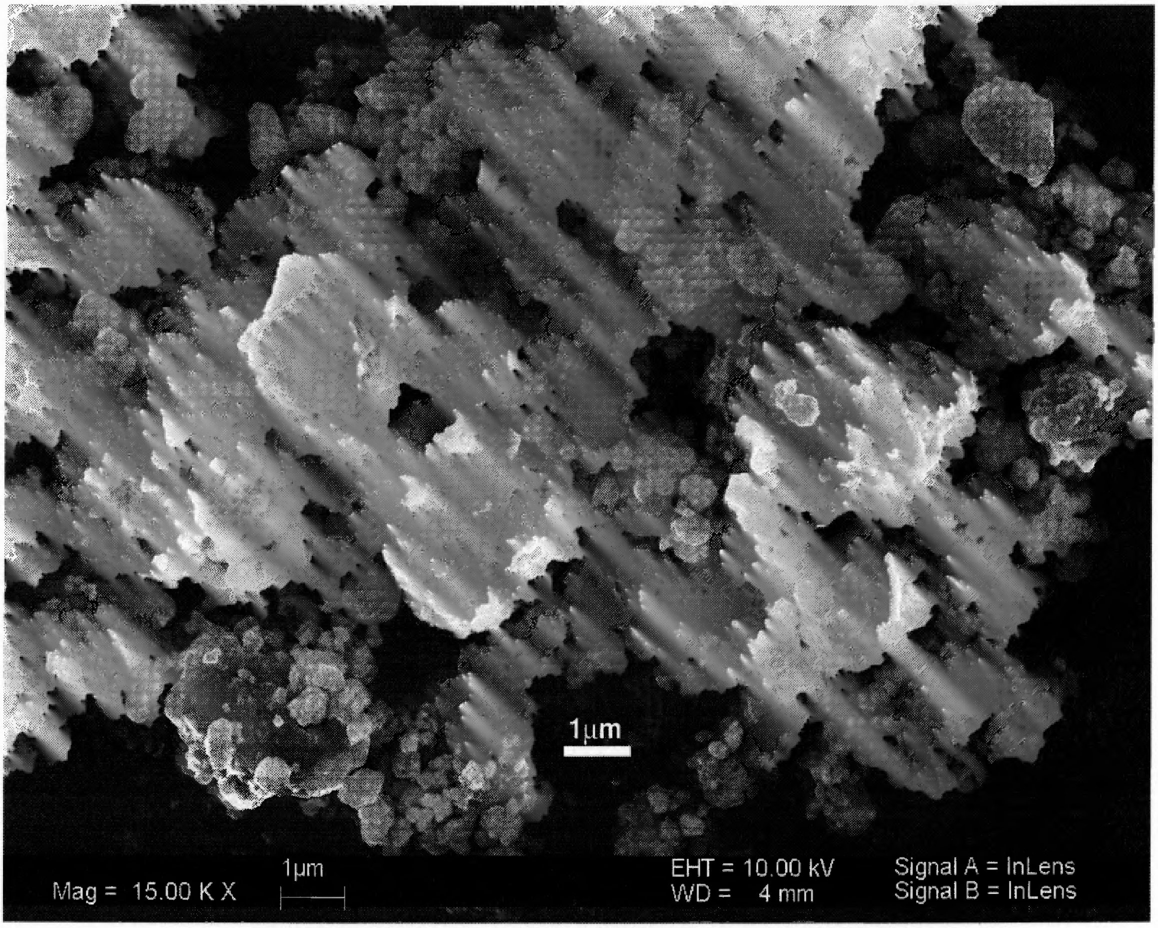

Figure 8.1 A typical SEM image of the $Al_{0.7}Li_{0.3}$ mechanically alloyed powder (milling time 102 hours).

index of aluminum. The particular shape of the size distribution was found to be reproducible over several repeat measurements.

8.3.2 X-ray Diffraction

Comparison of XRD patterns for different samples prepared in this project indicated that the milling progress was very sensitive to subtle differences in the milling conditions, such as small variation of the amounts of the process control agent added to the samples. Caking could occur and cause significant reduction in the milling efficiency, so that different phases could be observed in different runs at the same

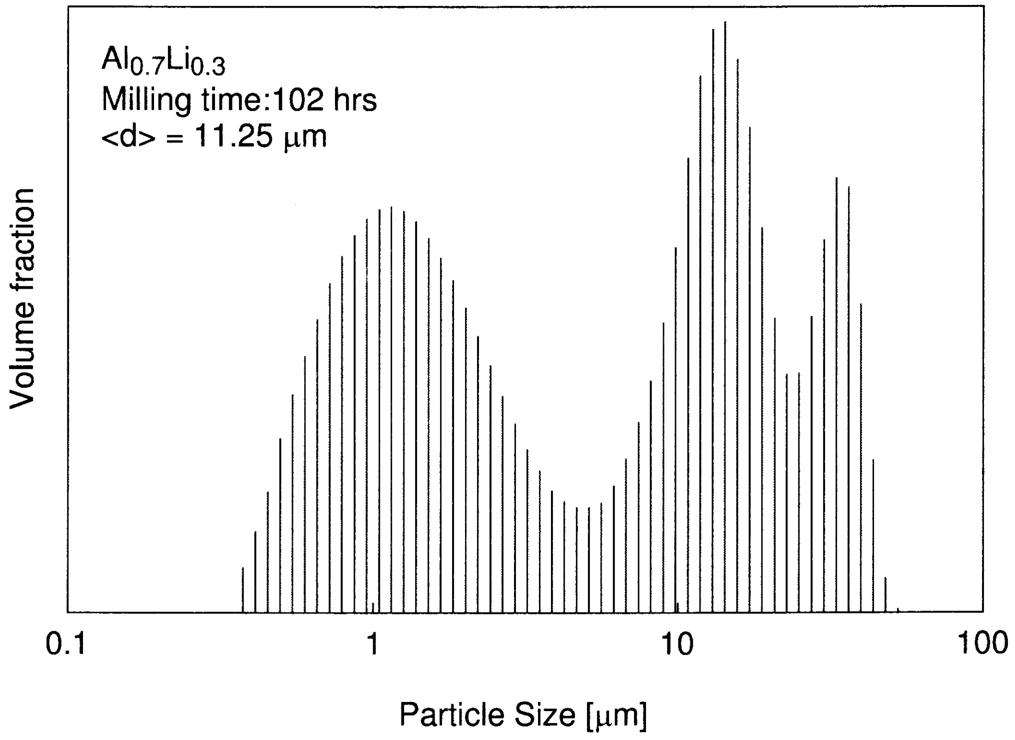

Figure 8.2 Particle size distributions for the mechanically alloyed $Al_{0.7}Li_{0.3}$ powder.

milling times and under nominally the same milling conditions. Runs for which the sample phase evolution was substantially slowed down by the caking were aborted and will not be discussed below.

XRD patterns of the product after milling for 102 hours, as well as for samples recovered at intermediate milling times, are shown in Figure 8.3. The two main crystalline phases identified in the powders were: α (*fcc*-Al) and δ (nominally LiAl intermetallic) [105]. The peaks for the δ phase appear after several minutes of milling and disappear at extended milling times (around 39 hours.) The overall peak intensity for the crystalline phases decreased as a function of the milling time indicating the increased presence of an amorphous phase that could not be identified from XRD. The peaks also became broader, indicating a reduction in the crystallite size. Finally, the peak positions shifted slightly, indicative of a change in the lattice

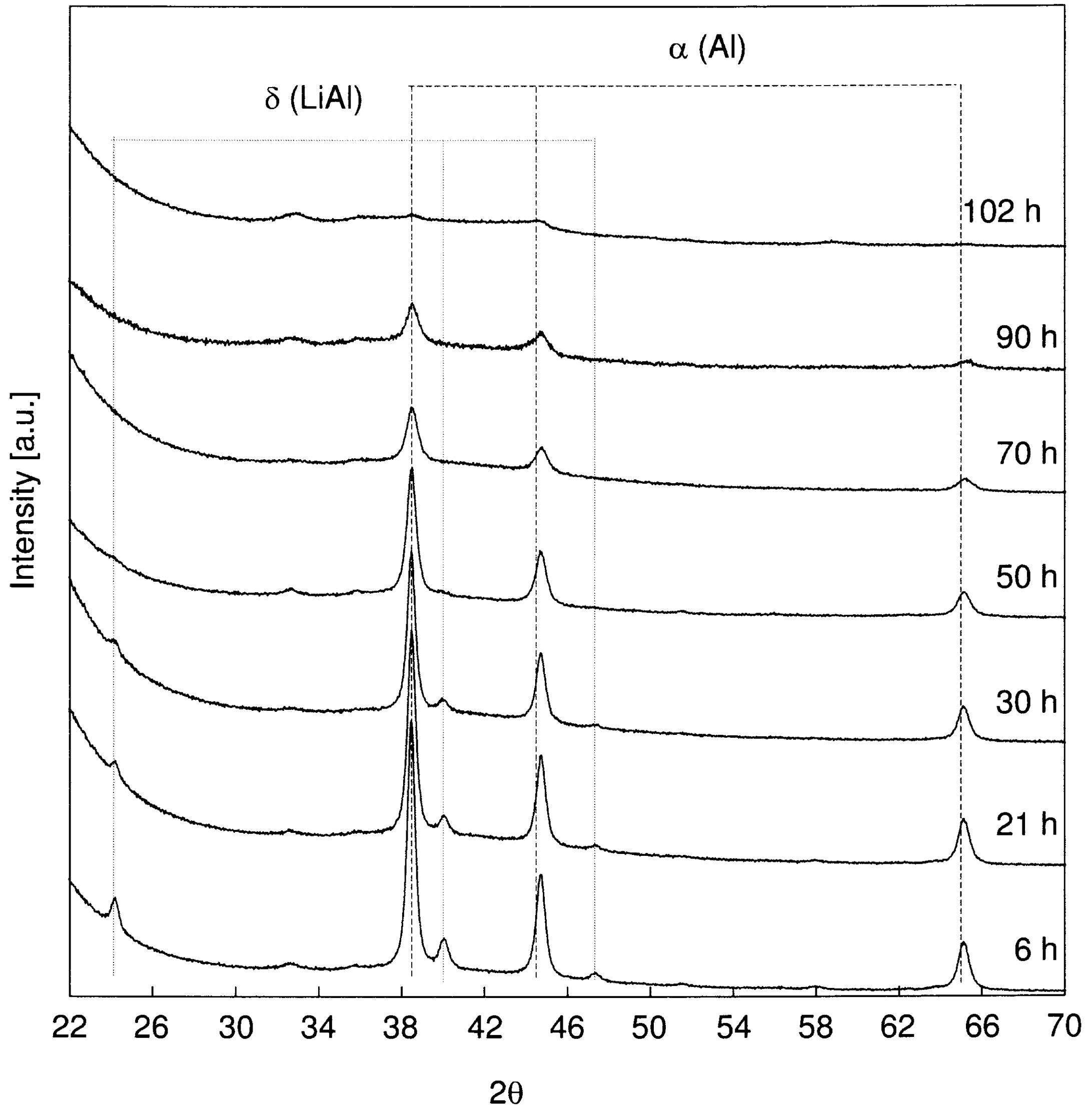

Figure 8.3 XRD patterns of mechanically alloyed $Al_{0.7}Li_{0.3}$ powders at varying milling times.

parameters as a result of the formation of solid solutions with variable Al/Li ratios. The lattice parameters were determined for intermediate samples and are shown in Figure 8.4. The overall trends of decreasing lattice parameter for the α-phase and increasing lattice parameter for the δ-phase indicate that Li concentrations increase somewhat for both phases.

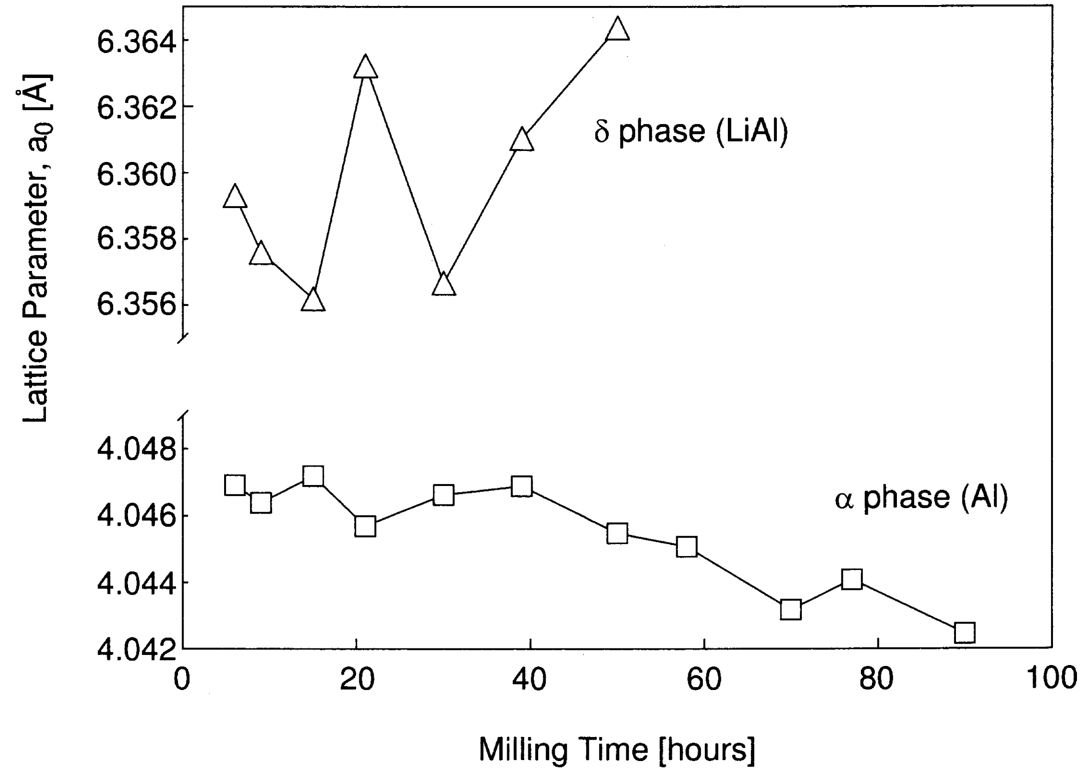

Figure 8.4 Lattice parameters of the α and δ phases at different milling times.

To quantify the observed trends, the XRD patterns were processed using the GSAS whole pattern refinement software [76]. The composition of the prepared powders was determined based on the detailed analysis of the XRD measurements, considering information available in the literature describing alloys and solid solutions in the Al–Li binary system. Specifically, it was reported that the lattice parameters for the α- and δ- phases change as a function of their respective elemental compositions [106–109]. Thus, the experimental changes of the lattice parameter for both α and δ phases were processed to determine their respective elemental compositions for the mechanically alloyed powders recovered at different milling times. In addition, the concentration and bulk composition of the x-ray amorphous phase were quantified as described below.

All crystalline phases were treated as solid solutions with variable Li concentrations. Similarly, any undetected amorphous phases were also treated as one solid solution with variable Al and Li concentrations. The concentration of Li in the a phase, $x_{Li}(\alpha)$ was determined from the relation, derived from data given in Ref. [109]:

$$x_{Li}(\alpha) = -1.467 \cdot (\frac{a_\alpha}{a_{Al}} - 1) \tag{8.1}$$

Where a is the lattice parameter and the subscripts refer to the specific phases: α refers to the Al-Li solid solution and Al to the Li-free Al phase. Similarly, the Li concentration in the d phase was determined from the relation [107]:

$$x_{Li}(\delta) = 0.5 + 19.78 \cdot (\frac{a_\delta}{a_{LiAl}} - 1) \tag{8.2}$$

where δ refers to the solid solution and LiAl to the ideal intermetallic with 50 at-% Li. For quantitative processing of the XRD patterns, the presence of any amorphous phases that are not detected by XRD is necessary to take into account. To approximately quantify the amount of the amorphous phase present at different milling times, the XRD patterns were calibrated based on the absolute intensity of the peaks corresponding to the detected crystalline phases. The total diffracted intensity corresponding to the a and d phases decreased with increasing milling time, and since the amount of sample used in the XRD measurements was held constant, it could be concluded that the amount of x-ray amorphous material in the sample increased with milling time. The amount of undifferentiated x-ray amorphous phase was estimated from the difference of total observed diffracted intensity (α and δ phases) at a given milling time, and the intensity for an identically mounted sample before milling. This procedure is sensitive to incidental variations in the sample preparation for XRD measurements, but still provides a rough estimate of the amount of amorphous

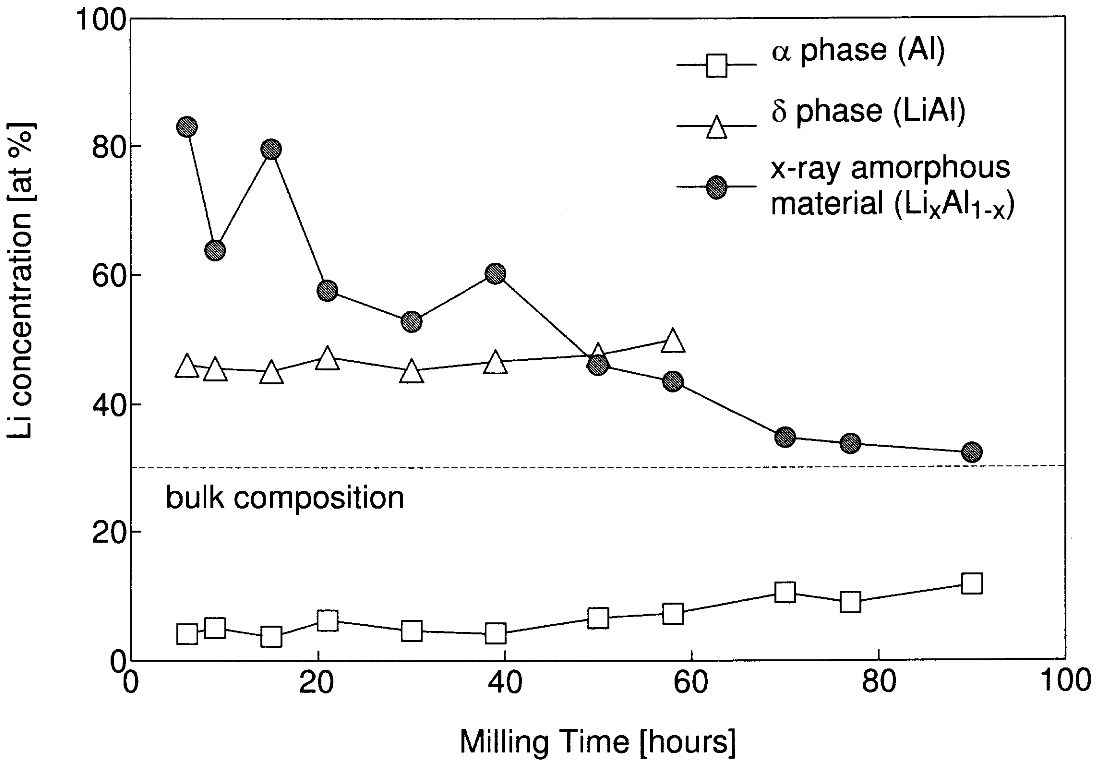

Figure 8.5 Evolution of the elemental compositions in the α and δ phases in mechanically alloyed powders recovered at different milling times.

phase present. The composition of the amorphous phase was estimated from the Li balance.

The results of the data processing showing the evolution of the elemental compositions in the α and δ phases at different milling times, as well as the corresponding fractions of the crystalline and amorphous phases are shown in Figures 8.5 and 8.6 for the 102-hr run. The results are also shown in Table 8.1. Figure 8.5 shows that the concentration of lithium dissolved in the crystalline (or nanocrystalline) α-Al structure exceeded 10 at-%, which is higher than previously reported. It follows from Figure 8.6 that the final mechanically alloyed powder after 102 hours of milling consists nearly entirely of x-ray amorphous phases.

Table 8.1 Lithium Concentrations and Phase Fractions of α, δ, and Amorphous Phases at Varying Milling Times (a 102-Hour Run)

Time [h]	Li concentrations [at-%]			Phase fractions [at-%]		
	α	δ	am.	α	δ	am.
6	4.2	46.1	83.0	61.5	12.2	26.3
9	5.1	45.6	63.8	53.7	12.2	34.1
15	3.7	45.2	79.5	62.2	6.9	30.9
21	6.2	47.4	57.5	52.3	7.2	40.5
30	4.7	45.3	52.8	46.6	4.5	48.8
39	4.2	46.7	60.2	53.4	2.0	44.6
50	6.6	47.7	46.1	40.8	1.0	58.2
58	7.3	50.0	43.6	37.4	0.2	62.4
70	10.5		34.8	19.6		80.4
77	8.9		33.7	15.0		85.0
90	11.7		32.2	10.8		89.2

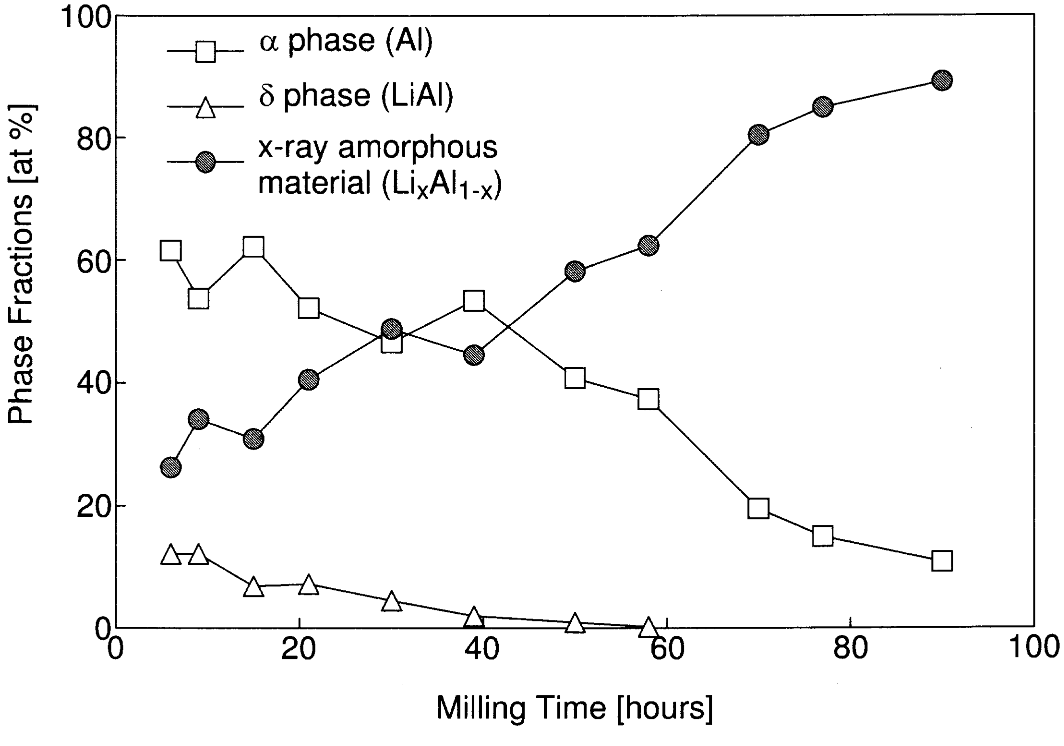

Figure 8.6 Relative concentrations of the crystalline and amorphous phases in mechanically alloyed powders recovered at different milling times.

8.3.3 Thermal Analysis

DSC traces collected for the mechanically alloyed powders recovered at different milling times are shown in Figure 8.7. For shorter milling times, three exothermic transitions were observed, starting at a very low temperature ($< 420\,K$). The assignment of the detected peaks to specific phase transformation is not straightforward; a number of phase relaxation processes were observed to occur in this temperature range in Al–Li alloys [95, 110–112]. Endothermic peaks corresponding to eutectic melting in the Al–LiAl subsystem and to Al melting were also observed.

8.4 Discussion

8.4.1 Phases in Mechanically Alloyed $Al_{0.7}Li_{0.3}$

A number of slightly diverging reports for the dependence of the lattice parameter of the a phase exist [106–108]. Podloucky et al. [109] compiled experimental results and compared them to a theoretical trend based on lattice dynamic calculations. The latter relation, the solid line in Figure 8.8, was used for the determination of the Li concentration of the a phase in this work (see Eq. 8.1 above). Figure 8.7. Only one literature source was found reporting lattice parameter changes of for δ phase with varying lithium concentrations (Ref. [107], Eq. 8.2).

The trends observed for the phase fractions follow previously observed trends for other Al-based mechanically alloyed powders. In the system Al–Mg, for example, the stoichiometric intermetallic $Al_{12}Mg_{17}$ forms readily after short periods of milling, but disproportionates after prolonged milling into the increasingly supersaturated α-Al phase and amorphous material [36]. It is stipulated that a similar process causes the amount of crystalline d phase to decrease with prolonged milling. The mechanical properties of α-Al on one hand and intermetallic phases on the other are different. The more brittle behavior of the intermetallic causes continued diminution

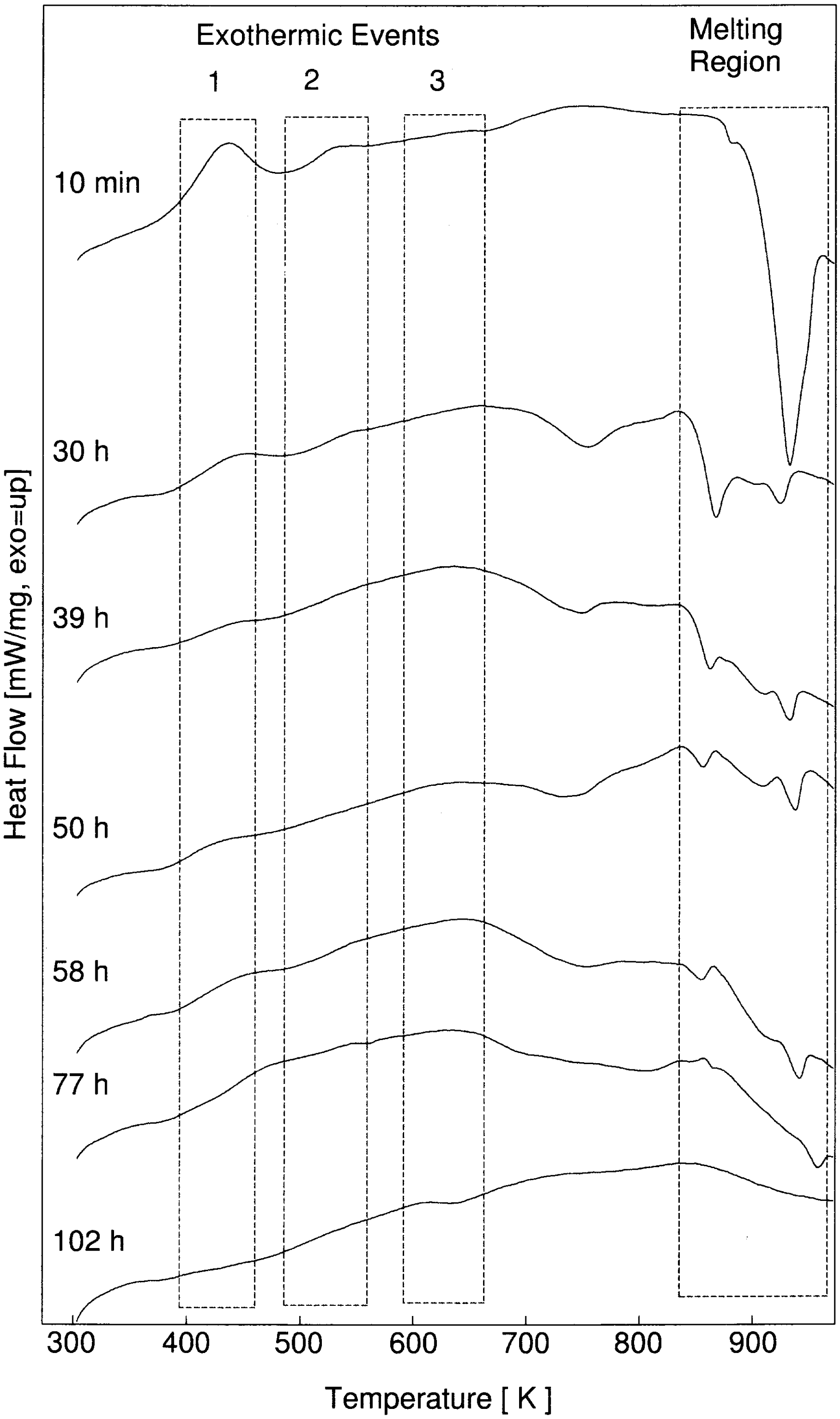

Figure 8.7 DSC traces of mechanically alloyed $Al_{0.7}Li_{0.3}$ powders at varying milling times.

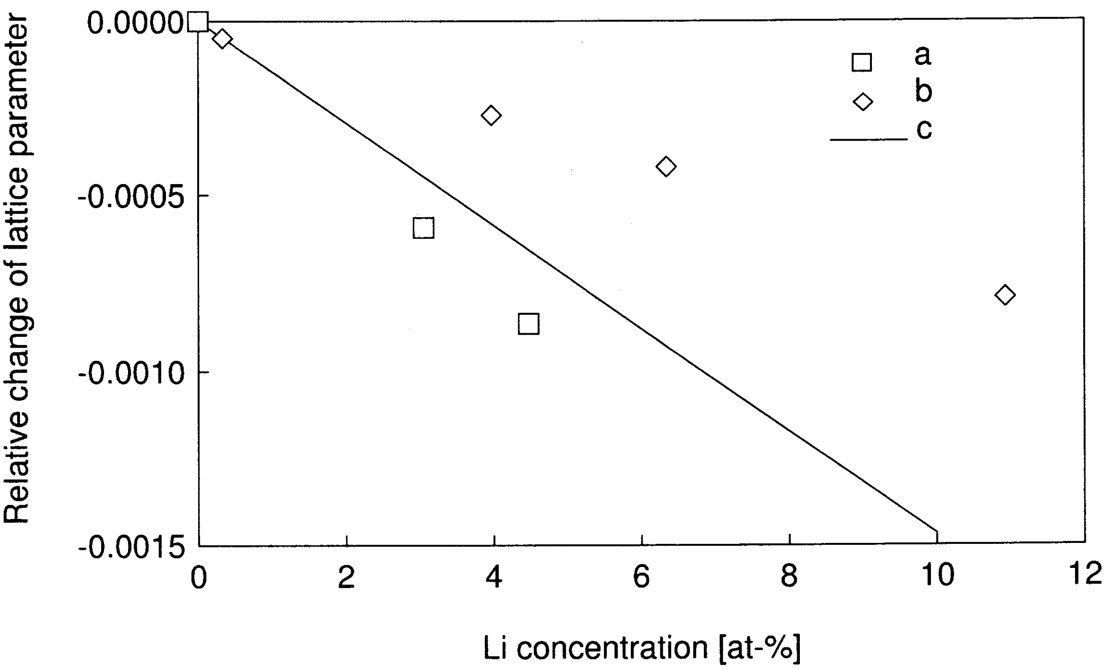

Figure 8.8 Comparison of literature references for the change of the lattice parameter of α-Al with the Li concentration. (a) results in Ref [108]; (b) results in Ref [107]; (c) results in Ref [109].

of the crystalline domains until the material effectively becomes amorphous. The a phase with its simpler *fcc* lattice is more ductile, and continues to incorporate Li until it becomes x-ray amorphous as well.

8.4.2 Thermal Analysis

According to the Al–Li phase diagram two stable phases exist in the range 0–50 at-% Li, α-Al and δ-AlLi [105]. Previously it has been reported that the decomposition of a supersaturated a phase proceeds by first precipitating a metastable δ' phase which later transitions to the d phase [111]. The energy associated with these transitions is not known, but likely to be small. Exothermic events 1, 2, and 3 observed at low temperatures (cf. Figure 8.7) are likely to be associated with these subsolidus relaxation processes; a more specific assignment would require more detailed measurements which were outside the scope of this project.

An endothermic peak was observed near 750 K. It could conceivably be associated with the peritectic melting of a Li-rich phase (e.g. Al_2Li_3), although no direct evidence for such a phase can be found in the XRD patterns.

It was further observed that the amorphous material after a milling time of 102 hours showed no discernible transitions, but instead a slow, spread-out exothermic bias of the baseline. This behavior is unusual and could indicate that most of the phase relaxation processes are suppressed. In other words, the relaxation of this material, typically accompanied by coarsening of the crystallites, cannot occur at a usual rate. This is likely associated with the highly developed network of grain boundaries in the x-ray amorphous material. This can significantly affect the kinetics of oxidation and ignition of such a material. It is also likely that this material will age differently (more slowly) as compared to the regular intermetallic phases.

8.5 Summary

Reactive binary Al–Li powders have been synthesized by mechanically alloying, and the product of milling for 102 hours is an amorphous phase. The products obtained at shorter milling times are α- and δ- phases, which are a solid *fcc* solution of Li in Al and the LiAl intermetallic. The lattice parameters of these two phases change as a function of the milling time due to continuing dissolution of Li in the Al matrix. A solid solution of Li in Al (α-phase) is formed with as much as 10 at-% of dissolved Li. Both DSC trace and XRD pattern of the final product show a decrease in the concentration of crystalline phases and an increase in the concentration of x-ray amorphous phase at longer milling times. No distinct transitions were observed by thermal analysis associated with the relaxation of the amorphous material. It is suggested that equilibration is kinetically hindered by a relatively stable network of grain boundaries.

CHAPTER 9

IGNITION OF MECHANICALLY ALLOYED ALUMINIUM-LITHIUM POWDERS IN AIR

9.1 Introduction

Combustion of metallic fuels has been of interest for many years because of their high energy densities [4, 11, 113]. Burning of powders of pure metals, such as Al, Mg, Zr, and others was studied by many researchers [7–9, 22, 32, 43], while ignition and combustion of alloys received considerably less attention [114–116]. At the same time, it was indicated that some alloys exhibit many practical attributes that warrant their fundamental study as potential additives to propellants, explosives, and pyrotechnics [34, 35]. In particular, using different alloys helps to shorten ignition delays for metallic fuel particles [57] and thus significantly increase the efficiency of their combustion in many practical devices, in which the overall time of reaction must be limited by the residence time of particles in the combustion chamber. The ignition delays represent a specifically severe problem for aluminum [16, 17], which otherwise has the most attractive properties as a fuel additive, including a high reaction enthalpy, high combustion temperature, low density, and low cost [19, 20]. The long ignition delays are due to the impervious layer of aluminum oxide that slows down the heterogeneous oxidation leading to ignition [79, 117]. Thus, aluminum-based alloys are of interest, which maintain the high reaction enthalpy of aluminum but could be ignited easier than pure aluminum. The choice of an alloying element is typically made to advance a specific application and use of Li is especially attractive for underwater propulsion systems. Lithium is well known to be extremely reactive with water. Lithium-water reaction chemistry at elevated temperatures was systematically investigated by Klanchar et al. [118] Lee and Ford [119] investigated reactivity of

Al-2.5% Li alloy with water using an exploding wire technique. They concluded that the high reactivity of the alloy is due to the presence of Li which facilitates the rate of the mixing of the molten metal with water and increases the oxide formation rate. Also a number of researchers studied the surface oxidation mechanism of Al–Li alloys [120–122]. Recently, Moore el at. [104] reported a detailed investigation on combustion of pre-heated lithium-aluminum alloys in a relatively narrow range of flame temperatures. Expanded flame temperature ranges or the heterogeneous processes leading to ignition were not considered.

Despite substantial interest in Al–Li alloys as additives to energetic materials, relatively little is known about the mechanisms of their ignition and combustion. One of the principal reasons for this is that Al–Li alloys with the lithium concentrations exceeding several percents, which would be of practical interest to combustion applications, are not readily available.

In Chapter 8, we report preparation and characterization of Al–Li alloys using mechanical alloying. This chapter is focused on an investigation of reactivity and ignition kinetics of such alloys. The technical approach is based on experimental characterization of reaction kinetics of the produced alloys for a broad range of heating rates. The results are interpreted considering changes in the structure and phase make-up occurring in the alloys upon their heating.

9.2 Materials

A detailed description of synthesis of the Al–Li alloys was given in Chapter 8. One bulk composition of $Al_{0.7}Li_{0.3}$ of the mechanically alloyed powder was prepared and used in this project. In addition to the sample milled for 102 hours and described in detail in Chapter 8, a sample milled for 40 hours was prepared and used in this study. Despite the same bulk compositions, the two samples differ

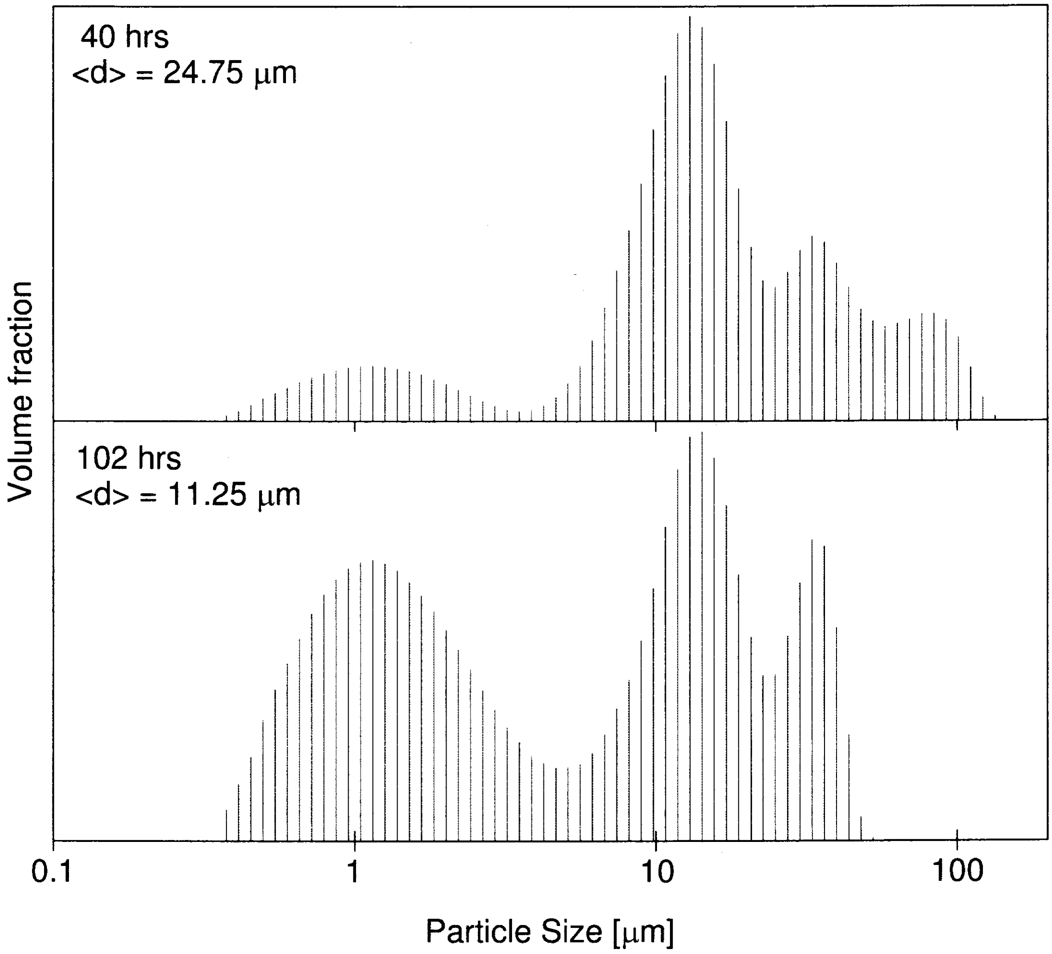

Figure 9.1 Particle size distributions measured by LS230 for two $Al_{0.7}Li_{0.3}$ mechanically alloyed powders.

in crystallinity and exhibit different relaxation reactions upon heating. Thus, the structures, morphologies, and reaction behaviors for both materials are described and compared to each other in this chapter.

The particle sizes of mechanically alloyed powders were measured using a low angle laser light scattering particle size analyzer LS230 (cf. § 8.2.2 for details). The particle size distributions for both samples milled for 40 hrs and 102 hrs are shown in Figure 9.1. While the calculated volumetric average particle sizes appear to be different (around 25 and 11 μm for the 40 and 102 hrs samples, respectively), the particle size distributions look similar to each other. For both

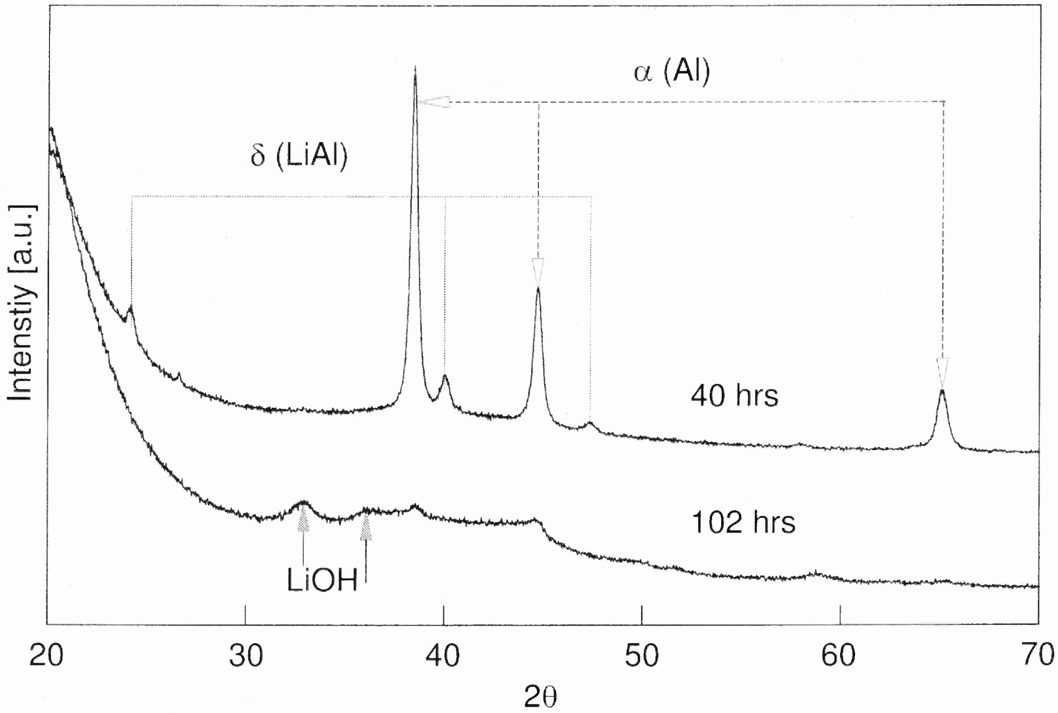

Figure 9.2 XRD patterns $Al_{0.7}Li_{0.3}$ powders mechanically alloyed during 40 and 102 hours.

size distributions, a peak around 1 μm is observed in addition to several peaks for the particle sizes exceeding 10 μm. An SEM image shown in Figure 8.1 illustrates the characteristic particle morphology. For both powders, the fine particles of around 1 μm represent the bulk of the sample. These particles also form larger, 10 – 20 μm agglomerates, which are responsible for the respective measured peaks in the particle size distributions. Additional measurements showed that the number of particle agglomerates could be reduced dramatically by an additional wet milling step.

The structures of the two powders were compared using XRD analysis (cf. § 8.2.2 for details). The acquired XRD patterns for both samples are shown in Figure 9.2. The pattern for the sample milled during 40 hours contains well resolved peaks of α-aluminum (starting material) and the peaks of an intermetallic phase δ-LiAl. The pattern of the sample milled during 102 hours is very different and

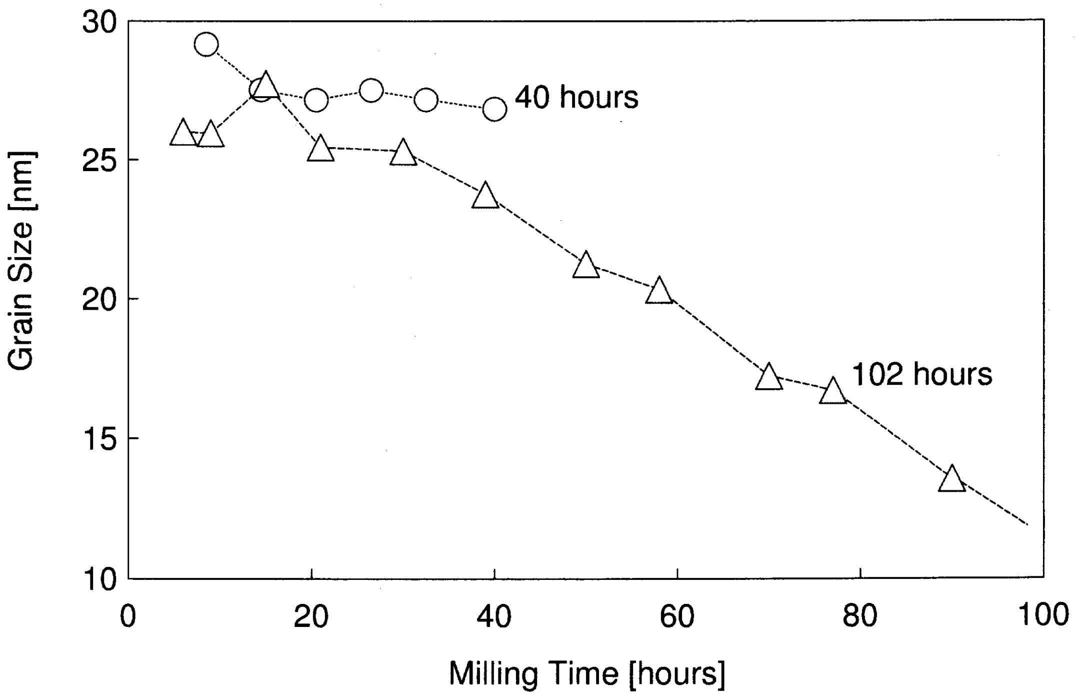

Figure 9.3 Aluminum grain size calculated using collected XRD patterns as a function of the milling time for two mechanically alloying experiments using the bulk composition $Al_{0.7}Li_{0.3}$.

hardly any crystalline phases can be detected. Weak peaks of LiOH are observed, which most likely indicate that the sample started to oxidize in room air during its handling for the XRD analysis. Extremely broad and weak peaks representing α-aluminum can also be detected over a generally flat XRD pattern.

The XRD patterns for the prepared samples as well as for the powders collected after intermediate milling times were processed to determine the evolution of grain sizes using the integral breadths method [123, 124]. Five peaks of α-Al phase, (111), (200), (220), (311) and (222), were considered for calculation. The results are shown in Figure 9.3, where the grain size is plotted as a function of the milling time. No data points are shown for the final sample milled for 102 hours because the peaks in the obtained XRD pattern were too weak to be processed. The data presented should be treated as an indicator of the change in the grain sizes, but cannot be relied upon for the quantitative assessment of the actual grain size of aluminum. At short milling times, both samples show similar aluminum grain sizes, which are considerably smaller than that of the starting aluminum. However, the grain size for the sample milled during 40 hours does not change appreciably as a function of the milling time. This indicates an inefficient milling that could be caused, for example, by caking in the sample. On the other hand, the grain size for the sample milled during 102 hours decreases continuously as the milling time increases. This behavior is consistent with the literature reports for mechanically alloyed Al-based materials, in which the grain sizes were shown to decrease down to a few nanometers [125].

9.3 Thermal Analysis

Differential scanning calorimetry measurements were performed for both samples using a Netzsch Simultaneous Thermal Analyzer STA409 PC, as described in detail in § 8.2.2. Both materials were initially heated in Ar with a fixed rate of 15 K/min. The resulting DSC traces are shown in Figure 9.4. For the sample milled for 40 hours, a number of subsolidus exothermic events were observed followed by several fairly weak endothermic peaks. A number of investigators [111, 112, 126] reported similar, low temperature exothermic peaks in the DSC traces for Al–Li system, which are tentatively assigned to describe the following sequence of metastable phase relaxation changes: $\delta'' \rightarrow \delta' \rightarrow \delta$, where δ is the LiAl phase, δ' is the Al_3Li phase and δ'' is the precursor modification of the δ'-phase. The three observed endothermic events could be assigned based on the Al–Li phase diagram [105] as eutectic melting in AlLi–Al_2Li_3 and Al–LiAl systems followed by the Al melting, as labeled in Figure 9.4. Note that the first mentioned eutectic could not be expected for a homogeneous $Al_{0.7}Li_{0.3}$. Therefore, it indicates that the material included both lithium-rich and aluminum-rich regions. Of particular interest in this study were the subsolidus exothermic peaks which could serve as ignition triggers at the higher heating rates. Therefore,

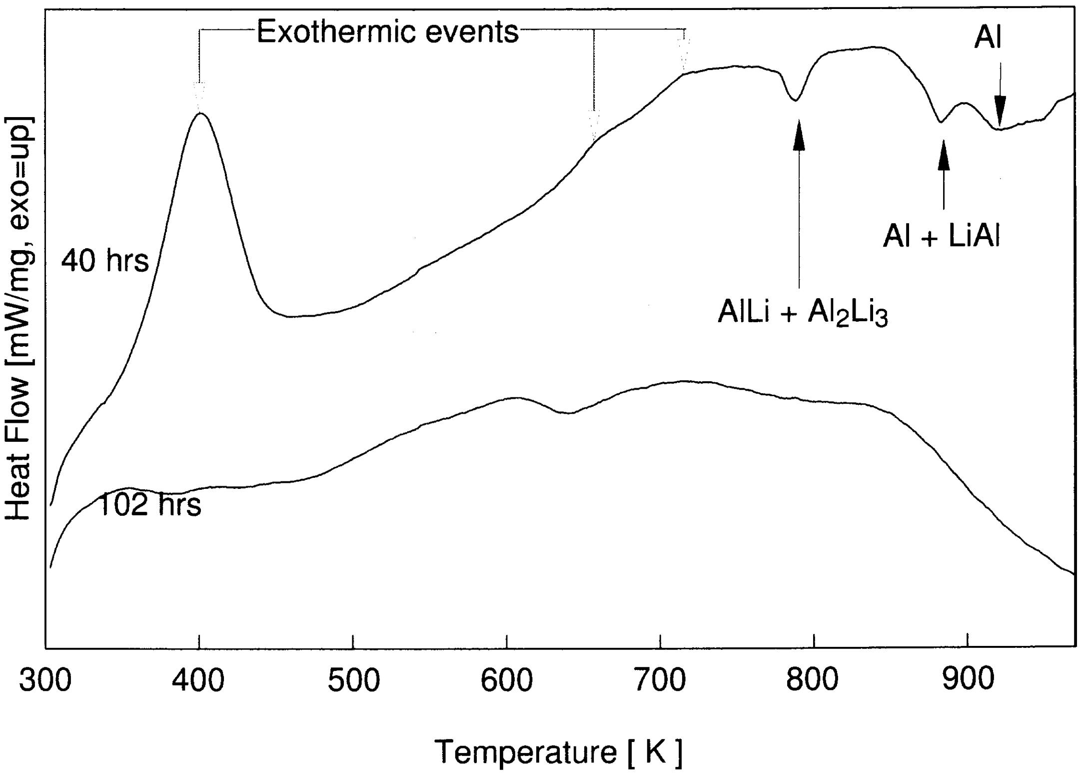

Figure 9.4 DSC traces for mechanically alloyed $Al_{0.7}Li_{0.3}$ samples heated in Ar at 15 K/min.

DSC measurements for the sample milled for 40 hours were repeated at four different heating rates, for 5, 10, 20, and 40 K/min and the shifts in the peak positions were recorded. The results of these measurements are shown in Figure 9.5 and Figure 9.6, also Table 9.1 gave the positions of all observed exothermic peaks and calculated activation energies.

The DSC trace recorded at 15 K/min for the sample milled for 102 hours (Figure 9.4) does not show any clearly distinguished events. Therefore, this measurement was not repeated at different heating rates. The reason for suppression of the exothermic metastable phase relaxation processes and ensuing melting of the intermetallic phases is unclear. It can be hypothesized that this behavior is associated with the lack of visible long range ordering in this sample, as implied by the respective

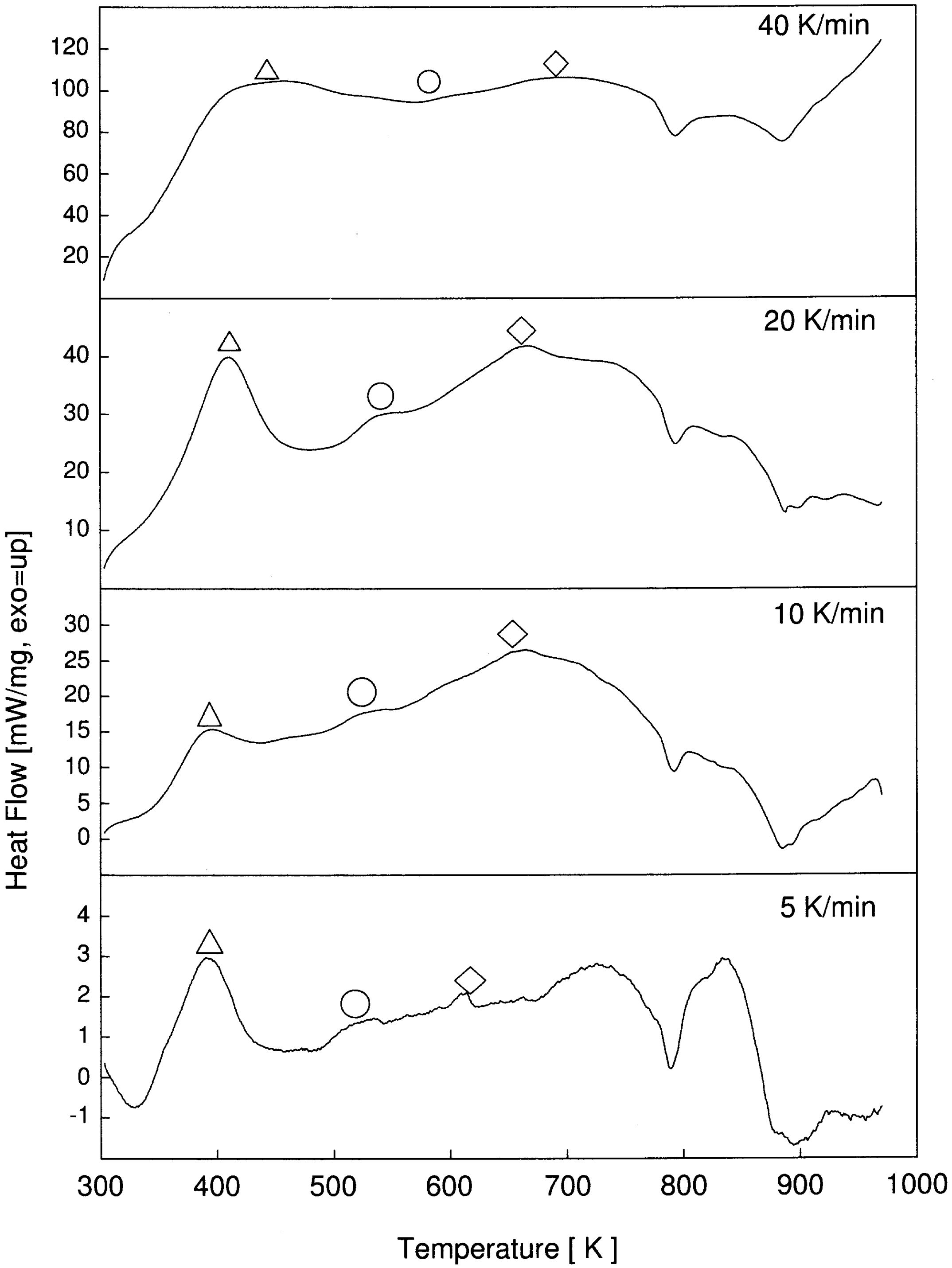

Figure 9.5 DSC traces with different heating rates. Positions of the first, second, and third exothermic peaks identified during the signal processing are shown as triangles, circles, and diamonds, respectively. The experiments are performed in Ar.

Table 9.1 Peak Positions and Related Activation Energies

	Exothermic Peak Positions [K]		
HR [K/min]	1st	2nd	3rd
5	389	507	645
10	399	521	653
20	413	527	669
40	421	547	675

	Related Activation Energies [kJ/mol]		
	1st	2nd	3rd
E_a	78.23 ± 0.78	113.63 ± 1.99	218.82 ± 3.45

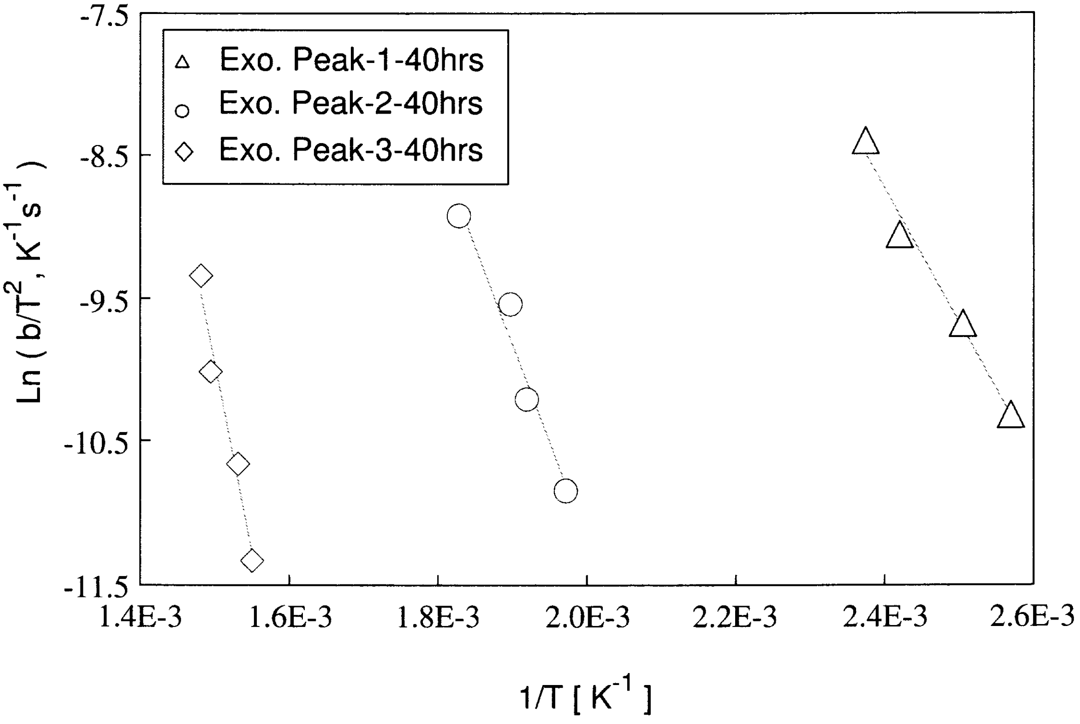

Figure 9.6 Arrhenius plot of logarithm of heating rate versus inverse temperature indicating the shifts in the positions of exothermic peaks observed in the DSC traces for a mechanically alloyed $Al_{0.7}Li_{0.3}$ sample milled for 40 hours. The experiments are performed in Ar.

XRD patterns (cf. Figure 9.2). This material could comprise of imperfect nanosized crystallites, which are not sufficiently large to produce detectible x-ray reflexes. At the same time, the highly developed network of dislocations existing in this material could suppress the mass transfer, e.g., migration of lithium atoms from one aluminum nano-crystallite to another. This reduced mobility could explain the suppression of the metastable phase relaxation processes.

9.4 Ignition of Mechanically Alloyed $Al_{0.7}Li_{0.3}$ Powders

9.4.1 Experimental

The experimental setup used an electrically heated filament, as described in Chapter 6 (Al–Ti ignition in air).

The lithium containing alloys are generally known to be unstable in air and have been stored and handled under a protective layer of hexane. Ignition experiments are performed in room air and, according to the experimental methodology described above, they involve an uncontrolled period of time when the powder coated on top of the filament is exposed to air before the filament is heated. Therefore, a series of preliminary experiments was carried out in which the powder was coated on the filament and remained exposed to air during two measured time intervals prior to heating the filament. The two exposure times used in these experiments were 2 and 10 minutes, after which the ignition tests were performed and ignition temperatures were measured. We used a mechanically alloyed powder milled for 40 hours and each individual experiment was repeated 5 times. The results of these preliminary experiments are shown in Figure 9.7. No meaningful difference was detected in the measured ignition temperatures for the powders held in air for 2 and 10 minutes. Therefore the experiments continued without a strict control of the time while the coating was exposed to air prior to the test. It should be noted that generally, this exposure time was close to two minutes.

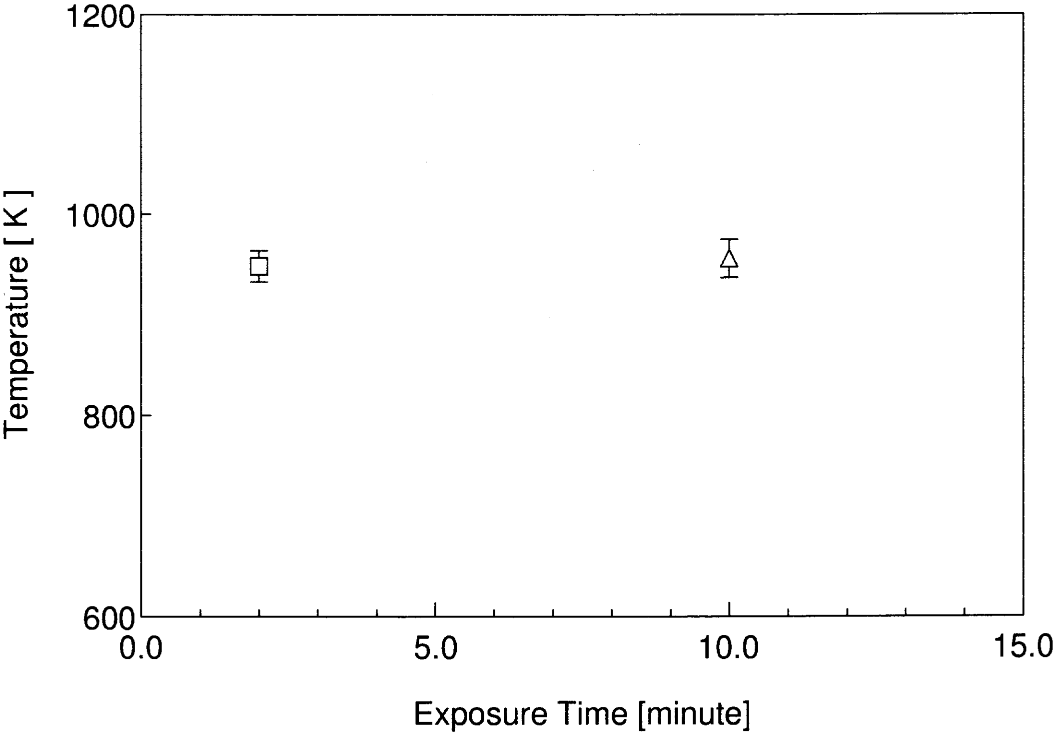

Figure 9.7 Preliminary ignition temperature measurements for the mechanically alloyed $Al_{0.7}Li_{0.3}$ sample milled for 40 hours after its exposure to room air for 2 and 10 minutes.

9.4.2 Results

The photodiode traces recorded in the ignition experiments exhibited several features that could be associated with exothermic events leading to ignition. This situation was similar to that observed earlier with Al–Ti alloys, as discussed in § 6.5. To illustrate these measurements, a typical recorded photodiode trace for an ignition experiment is plotted in Figure 9.8 together with a reference trace recorded in a similar run but without the powder coating on the filament.

As shown in Figure 9.8, for the reference run with a heated filament, the photodiode signal increases continuously, as is expected when the filament is heated by electric current. For the case of an igniting powder coating, the photodiode signal shows stepwise features indicative of exothermic processes occurring in the powder

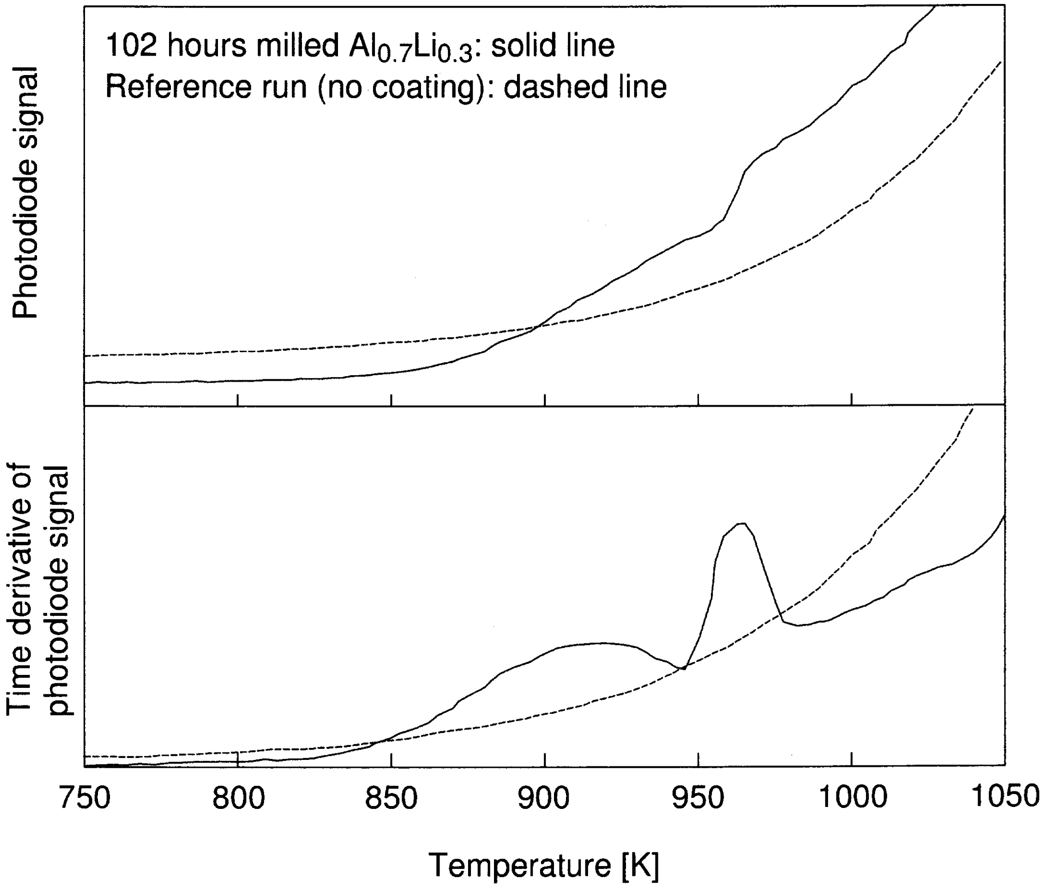

Figure 9.8 Recorded photodiode traces and their time derivatives for a typical ignition experiment. In addition, reference traces and trace derivatives are shown for a reference experiment performed at the same heating rate but without the powder coating on the heated filament.

at different temperatures. As was the case for the Al–Ti alloys (cf. § 6.2), these exothermic processes are easier identified from time derivatives of the photodiode signal, also shown in Figure 9.8. The time derivative of the reference filament trace does not show any noticeable features, whereas clearly identifiable peaks can be seen on the time derivative of the signal representing the $Al_{0.7}Li_{0.3}$ powder coating.

The temperature traces measured by the infrared pyrometer and recorded for both experiments presented in Figure 9.8 are shown in Figure 9.9. The measured filament temperatures are consistent with each other, indicating that the experiments

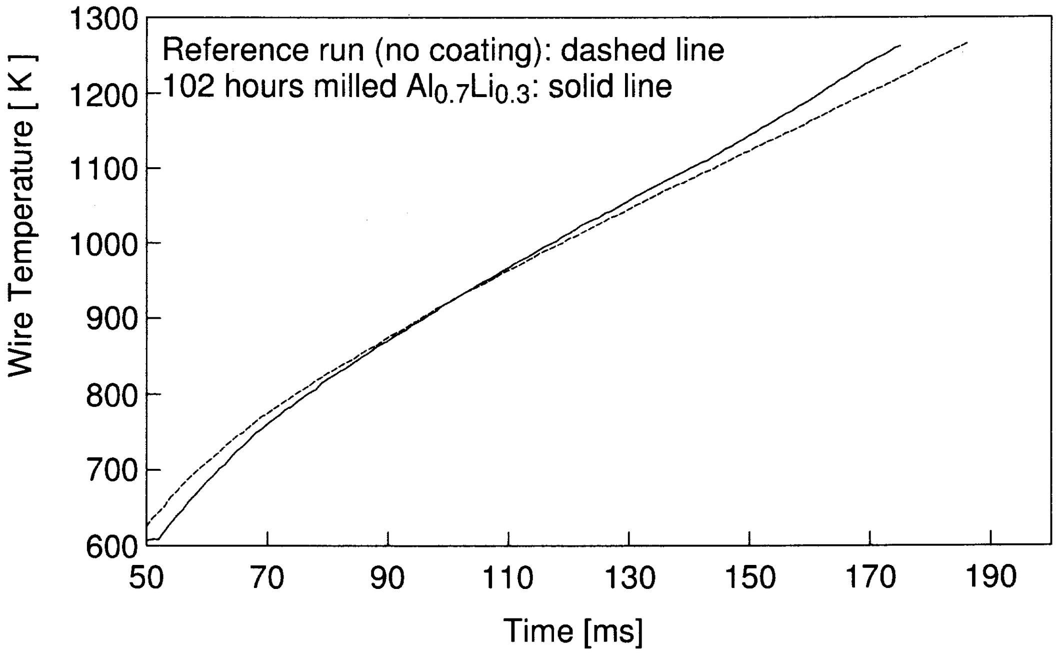

Figure 9.9 Filament temperature as function of heating moment for an ignition experiment with mechanically alloyed $Al_{0.7}Li_{0.3}$ powder coating and for a reference test with an uncoated filament (respective photodiode traces are shown in Figure 9.8).

were indeed well reproducible and that the coating did not affect the filament temperature.

Figure 9.10 shows two sets of characteristic photodiode traces recoded at different heating rates in ignition experiments with the two mechanically alloyed $Al_{0.7}Li_{0.3}$ powders milled during 40 and 102 hours, respectively. The target heating rates adjusted by the applied voltage and resistance included into the ignition circuit (cf. § 6.4) were 300, 1000, 3000, and 5000 K/s. Generally, higher heating rates resulted in somewhat better resolved peaks in the photodiode signal time derivative. Each peak or a stepwise, sharp increase in the photodiode signal derivative was considered as an "ignition event", while it was often unclear which specific event actually led to ignition.

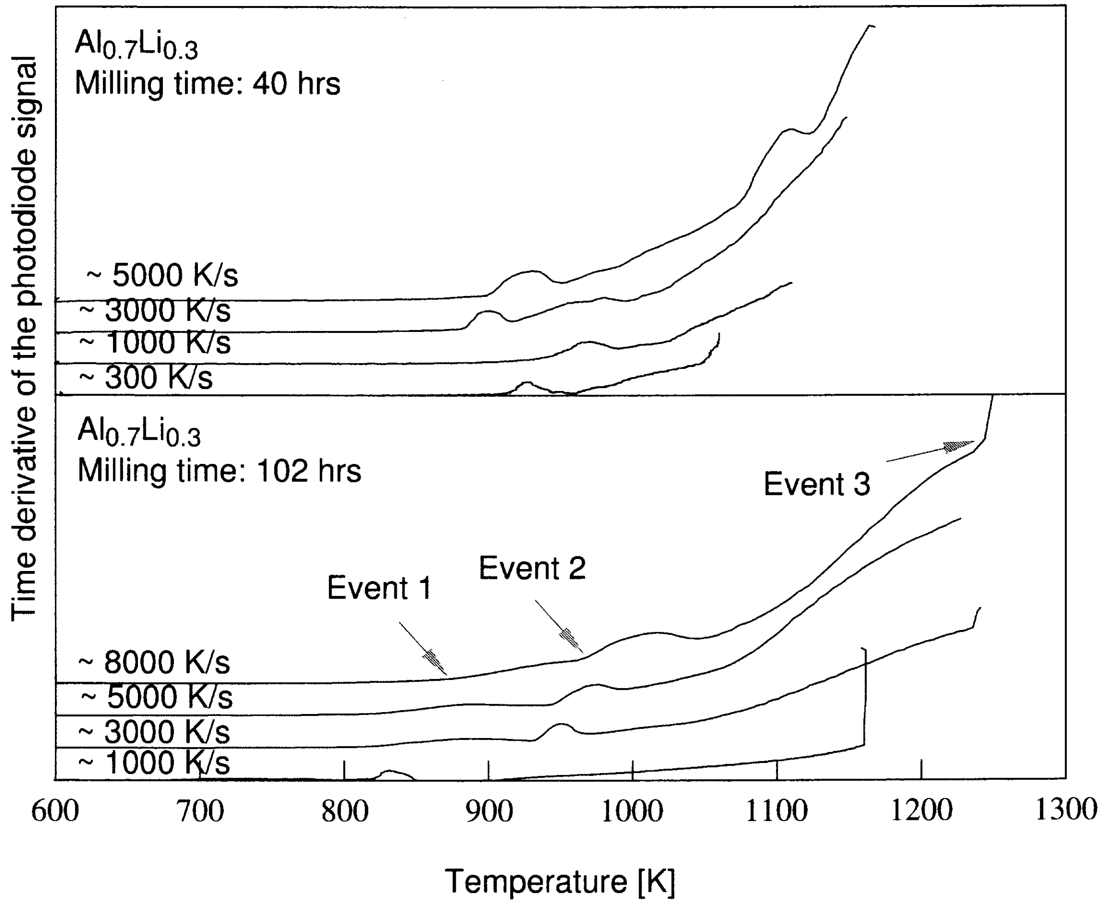

Figure 9.10 Time derivatives of the photodiode signal traces recoded at different heating rates as functions of the wire temperature for two mechanically $Al_{0.7}Li_{0.3}$ powders coated on an electrically heated filament.

As many as three ignition events (as labeled in Figure 9.10) could be resolved in a single ignition trace. However, some traces only showed two distinguishable events. In most experiments with the $Al_{0.7}Li_{0.3}$ powder milled for 102 hours, the third (and last) ignition event was observed as a sharp increase in the signal occurring in vicinity of 1200 K, which could clearly be assigned to the ignition of this material. For the powder milled for 40 hours, the last event occurring at similar temperatures appeared as one of the peaks in the photodiode derivative and assignment of ignition to either of the observed peaks was somewhat ambiguous.

The shapes of the features representing ignition events were not well reproducible for different heating rates. Therefore, tracking the same ignition event (e.g., feature number 1, 2 or 3 as labeled in Figure 9.10) in the photodiode derivative traces recorded at different heating rates was not always possible. All the events that could be traced from one heating rate to another, shifted to higher temperatures at the higher heating rates, as is expected for the thermally controlled processes.

In order to analyze the results of these measurements, all recorded photodiode derivative traces were processed to determine the onset temperatures for all the events that could be identified. These onset temperatures are plotted in the Arrhenius coordinates in Figure 9.11.

For the sample milled for 40 hours, the Arrhenius plot shows three well distinguishable groups of events, which are illustrated by shaded shapes in Figure 9.11.

The grouping of events for the material milled for 102 hours is unambiguous only for the high-temperature signal feature, assigned as "event 3" in Figure 9.10. Respectively, only one shaded shape in shown Figure 9.11 for the sample milled for 102 hours, highlighting the third event, which was most clearly associated with ignition for this powder, as noted above.

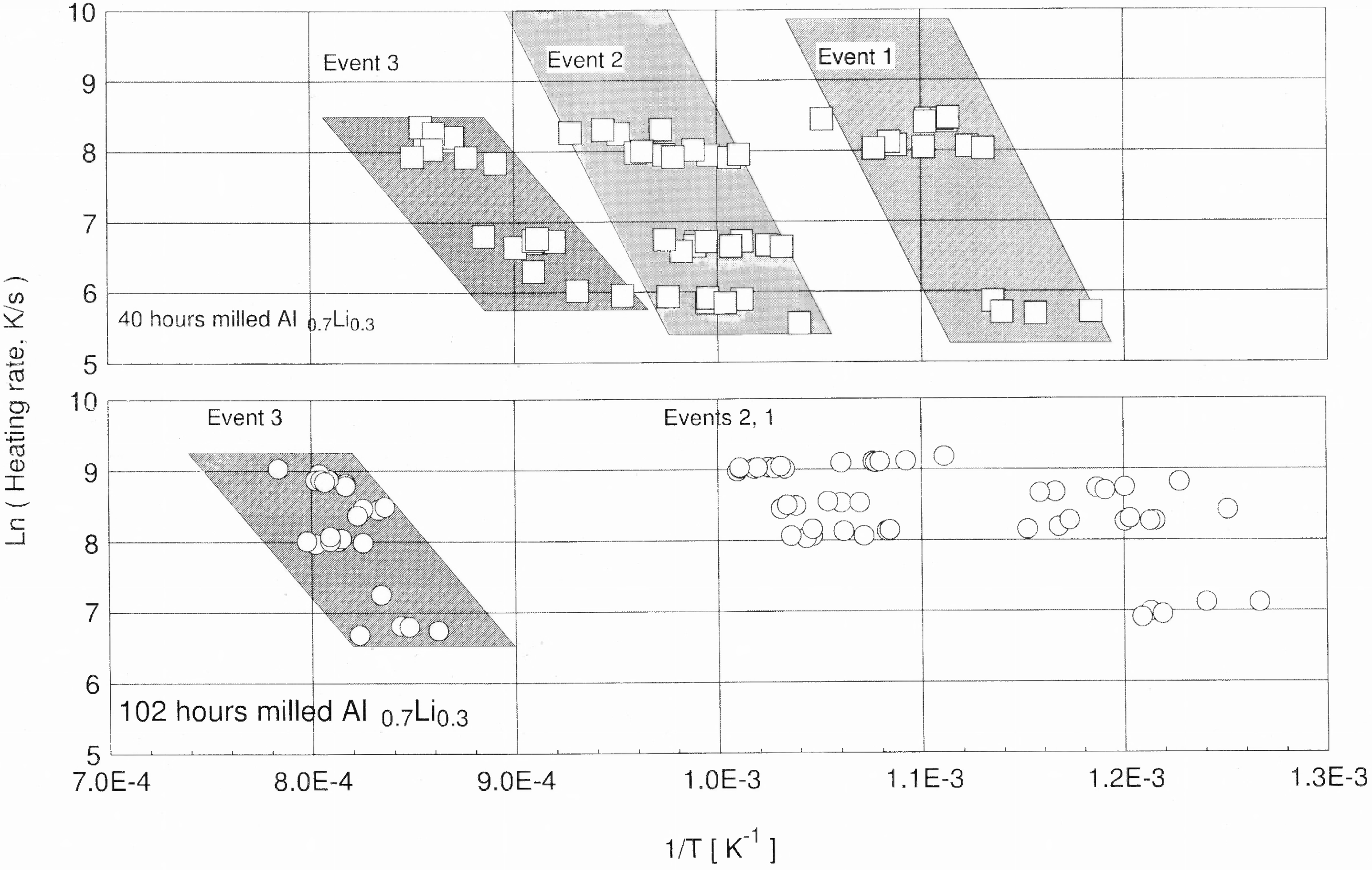

Figure 9.11 Arrhenius plot showing the onsets of ignition events detected from the time derivatives of the photodiode signal traces.

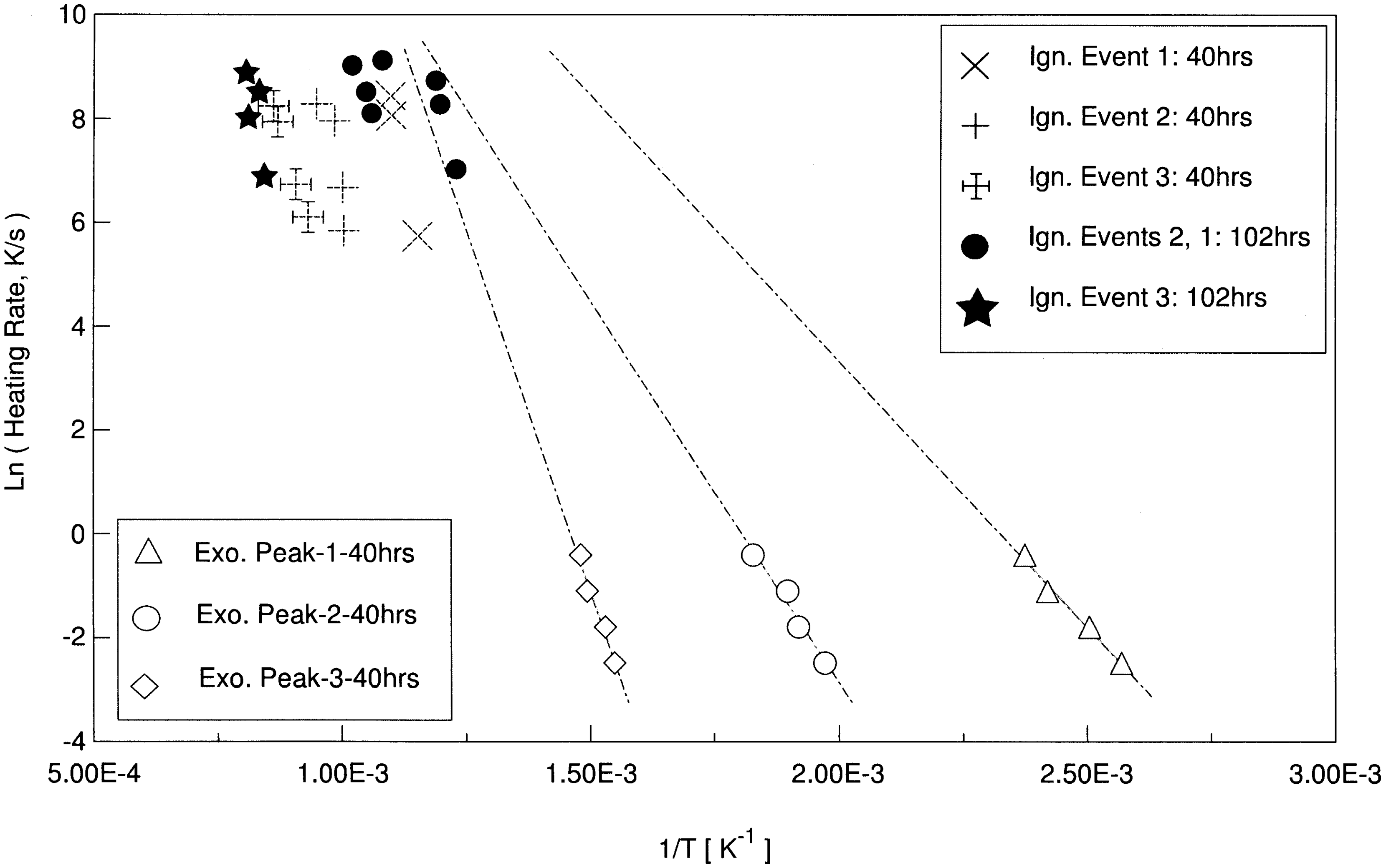

Figure 9.12 Arrhenius plots combining the DSC and ignition measurements (shown in Figures 9.6 and 9.11).

9.4.3 Discussion

The ignition temperatures observed for the prepared mechanically alloyed powders have been reduced, compared to those of pure aluminum. This is the expected effect that warrants practical interest in these materials. In addition to the experimental validation of this effect directly following from the results of ignition tests described above, it is of interest to establish which specific processes cause ignition of these materials. Two generic types of processes need to be considered: heterogeneous oxidation occurring on the surface of the igniting particle and exothermic phase relaxation processes that could boost the particle temperature and accelerate ignition.

The correlation between the ignition events and exothermic peaks observed in the DSC traces for mechanically alloyed $Al_{0.7}Li_{0.3}$ powders is of interest in order to evaluate the role of exothermic phase relaxation processes in accelerating ignition. This correlation can be investigated considering the Arrhenius plot shown in Figure 9.12, where the data shown in Figure 9.6 and 9.11 are combined together.

The trend lines show extrapolations of the trends implied from the DSC measurements. Note that the comparison is only meaningful for the $Al_{0.7}Li_{0.3}$ powders milled for 40 hours because the DSC traces did not show exothermic peaks for the powders milled for 102 hours (cf. Figure 9.4). The ignition events are mostly seen to occur at higher temperatures than implied by the kinetics of the exothermic peaks measured by DSC. The temperature range of ignition events 1 and 2 for both samples loosely correlates with the melting point of aluminum. However, the shift of the onset for these events as a function of heating rates shows that melting could not be the only process affecting ignition. The event three, occurring for both powders in vicinity of 1200 K, does not appear to correlate with the DSC measurements. It occurs after the powder is expected to be completely molten and, therefore, it is most likely associated with selective oxidation of molten lithium or accelerated bulk oxidation rate due to the disruption of the protective Al_2O_3 layer as a result of formation of Li_2O and $LiAlO_2$ [127–129]. It has been reported that when Al–Li alloys are heated to 860 – 905 K, Li diffusion rate increases substantially due to preceding structural transformations and lithium diffuses to the alloy surface, increasing the surface concentration of elemental Li so that the surface oxide becomes predominantly Li_2O [120]. This and similar processes could cause accelerated ignition but could be hardly noticed in the DSC analyses.

A somewhat more violent ignition at slightly higher temperatures observed for the material milled for 102 hours can be explained based on the hypothesis introduced earlier to interpret the suppression of the metastable phase relaxation processes for this material. Indeed, for the sample milled for 40 hours, a number of intermetallic phases are produced at low temperatures. As the temperature increases, the eutectic melting events produce a melt in which lithium becomes more mobile and thus more reactive. The molten lithium is selectively oxidized by the ambient air destroying the protective Al_2O_3 layer, which could explain the events 1 and 2 observed in the ignition experiments. However, for the sample milled for 102 hours, the suppressed phase relaxations prevent formation of Al–Li intermetallic phases and thus suppress respective eutectic melting. Respectively, the lithium diffusion is impeded and events 1 and 2 are less pronounced. The bulk of lithium remains trapped within nanocrystalline grains of aluminum until aluminum melting. As the temperature continues to increase and aluminum melts, liquid lithium is also produced and is readily oxidized. This could explain a somewhat delayed but stronger third ignition event observed for this material. In addition, consideration must be given to the possibility of the difference in the initial degree of oxidation for the two samples, which could affect the rates of oxidation processes occurring upon the sample heating.

The activation energies that are implied by processing the ignition measurements corresponding to the event 3 for the samples milled for 40 and 102 hours were around 236 and 275 kJ/mol, respectively. These values are substantially higher than activation energies around 65 kJ/mol reported for oxidation of pure Li [130]. Respective activation energies for the diffusion of Li ions through different Al_2O_3 polymorphs are still lower, of the order of $20 - 40\, kJ/mol$ [131,132]. Therefore, the rate of oxidation for the alloyed powders is most likely limited by the rates of phase relaxation (cf. activation energy for the peak 3 in Table 9.1) and diffusion of oxygen ions through alumina. Such diffusion processes typically have relatively high activation energies, comparable to the measured in this work [133,134]

9.5 Summary

Thermal stability and ignition behavior of mechanically alloyed $Al_{0.7}Li_{0.3}$ powders were investigated experimentally. Two mechanically alloyed samples were compared. One of the samples contained substantial concentration of the intermetallic LiAl and crystalline aluminum. The second sample was x-ray amorphous. It was observed that the metastable relaxation processes were suppressed for the x-ray amorphous sample. Both samples ignited at the temperatures around 1200 K, which are substantially lower than the ignition temperatures for pure aluminum powders. The x-ray amorphous sample ignited at a slightly higher temperature, but its ignition was characterized by a sharper peak in the photodiode signal compared to the other sample. Kinetics of the exothermic processes of metastable relaxation in Al–Li alloys observed in thermal analysis was not found to directly correlate with the ignition kinetics. It was proposed that ignition in the prepared alloys was driven by selective oxidation of Li, with its rate being affected by the phase transformations occurring in the alloy upon its heating and diffusion of oxygen through Al_2O_3 films.

CHAPTER 10

CONCLUSIONS

Mechanically alloyed powders in the Al-rich parts of the Al–Ti and Al–Li binary systems were produced for potential applications as additives to energetic materials.

The mechanically alloyed Al–Ti powders were chemically homogeneous on a scale of $\sim$ 10 nm. At small concentrations of Ti, the bulk of the Al–Ti alloys is a metastable solid solution of Ti in α-Al. The maximum degree of metastability is observed at 15 at-% Ti and the maximum Ti concentration in α-Al under the used milling conditions was found to be 1.6 at-%. The $L1_2$ phase of Al_3Ti, energetically less stable than the DO_{23} or DO_{22} phases, is likely to be present in mechanical alloys with 20 and 25 at-% Ti based on the observed XRD patterns and trends in enthalpies of exothermic transitions. No such Al_3Ti precursor phases are present in mechanically alloyed powders with compositions up to 15 at-%. For alloys with 20 at-% or less of Ti, an endothermic transition was observed around 1173 K, which was assigned to the formation of aluminum and titanium carbides with carbon impurities available from stearic acid added to the mechanically alloyed powders as process control agent.

It has been experimentally verified that a planetary mill can be used as well as a shaker mill to produce metastable, mechanically alloyed powders in the Al–Ti system. Powders with the bulk composition $Al_{0.67}Ti_{0.33}$ (Al_2Ti) have been synthesized with the batch size of 100 g (per vial). The XRD analysis showed that the material structure was being continuously refined at increased milling times. The decrease in the aluminum lattice parameter at increased milling times was interpreted to show a continuous formation of a metastable solid solution.

The oxidation of synthesized Al–Ti powders was investigated by thermal analysis. Oxidation proceeds in three distinct steps, similar to the oxidation steps observed for pure Al. These oxidation steps are relatively sharp, but become more and more diffuse with increasing Ti concentration. Apparent activation energies have been determined for the more reproducible first and second oxidation steps for each alloy composition. For both first and second oxidation steps, the apparent activation energies are close to $400\,kJ/mol$. Partially oxidized powders were obtained and quantitative x-ray analysis was performed, confirming that Al_2O_3 and TiO_2 were the main reaction products. At higher temperatures, the ternary oxide Al_2TiO_5 forms, however, not as a product of direct oxidation. The presence of $\gamma - Al_2O_3$ in the samples after the first oxidation step was inferred from observed deviations of the calculated Al–Ti balance and confirmed by processing of selected XRD patterns. Based on the experimental results, it is proposed that overall oxidation mechanism of the Al-rich Al–Ti alloys prepared by MA is qualitatively similar to that of pure aluminum and is most notably affected by the polymorphic phase changes in the produced Al_2O_3 layers. Such phase changes affect the rates of diffusion through protective Al_2O_3 layers which, in turn, control the oxidation rates. The ranges of stability of different Al_2O_3 polymorphs produced on the surface of alloys are changed compared to those for pure aluminum: specifically, the amorphous alumina is stabilized to the temperatures exceeding the melting point of aluminum. The oxidation rates are also affected by the intermetallic phase changes and formation of ternary Al_2TiO_5 oxides at elevated temperatures. Aluminum melting is not observed to affect the oxidation rate of the mechanically alloyed Al–Ti powders.

Ignition of metastable Al–Ti mechanical alloys was investigated experimentally using an electrically heated filament. Radiation traces produced by the igniting powders were analyzed. A characteristic peak on the radiation trace corresponding to the powder ignition was identified and the kinetic relations of this and other observed peaks were investigated. Comparison of the characteristic temperatures and kinetics for the characteristic peaks in the radiation traces versus phase changes and oxidation steps was determined by thermal analysis showing that the exothermic formation of the metastable $L1_2$ phase of Al_3Ti triggers ignition in the Al–Ti mechanical alloys. This conclusion was confirmed by additional ignition experiments in which annealed mechanical alloys already containing the transition Al_3Ti phase did not ignite in the same temperature range as fresh mechanical alloys.

Assuming that the kinetics of the exothermic formation of the $L1_2$ structure of Al_3Ti and of the ignition onset are identical, the ignition temperatures for different Al–Ti mechanical alloys can be predicted for wide ranges of experimental heating rates.

Al–Li alloys were synthesized with a fixed bulk composition of $Al_{0.7}Li_{0.3}$. The products obtained at shorter milling times are α- and δ- phases, which are a solid fcc solution of Li in Al and the LiAl intermetallic. The lattice parameters of these two phases change as a function of the milling time due to continuing dissolution of Li in the Al matrix. A solid solution of Li in Al (α-phase) is formed with as much as 10 at-% of dissolved Li. Both DSC trace and XRD pattern of the final product show a decrease in the concentration of crystalline phases and an increase in the concentration of x-ray amorphous phase at longer milling times. No distinct transitions were observed by thermal analysis associated with the relaxation of the amorphous material. It is suggested that equilibration is kinetically hindered by a relatively stable network of grain boundaries.

Thermal stability and ignition behavior of mechanically alloyed $Al_{0.7}Li_{0.3}$ powders were compared experimentally for two powder samples. One of the samples contained substantial concentration of the intermetallic LiAl and crystalline aluminum. The second sample was x-ray amorphous. Both samples ignited at the temperatures around 1200 K, which are substantially lower than the ignition temperatures for pure aluminum powders. The x-ray amorphous sample ignited at a slightly higher temperature, but its ignition was more violent as compared to the other sample. Kinetics of the exothermic processes of metastable relaxation in Al–Li alloys observed in thermal analysis was not found to directly correlate with the ignition kinetics. It was proposed that ignition in the prepared alloys was driven by selective oxidation of Li, with its rate being affected by the phase transformations occurring in the alloy upon its heating and diffusion of oxygen through Al_2O_3 films.

In summary, it was shown that mechanical alloying offers an attractive avenue for modifying aluminum powders used as additives in propellants, explosives, and pyrotechnics. The ignition delays can be substantially reduced as a result of several processes, including exothermic phase relaxation processes occurring in the metastable mechanically alloyed powders, modification of protective aluminum oxide layers, or selective oxidation of the alloying element. Detailed characterization of the stability, structure, and oxidation kinetics of the new materials is needed for quantitative modeling of their ignition and combustion behavior. Further research needs to be directed at expanding the range of the respective metastable Al-based alloys, development of a commercially viable powder manufacturing technology, and detailed studies of combustion mechanisms of the novel mechanically alloyed powders.

REFERENCES

[1] M. L. Chan, R. Reed, and D. A. Ciaramitaro, *Advances in Solid Propellant Formulations*, in *Progress in Astronautics Aeronautic*, T. B. Brill, W.-Z. Ren, and V. Yang, Eds., July 2000, vol. 185, no. 1, pp. 185–206.

[2] T. A. Brzustowski and I. Glassman, "Vapor-Phase Diffusion Flames in the Combustion of Magnesium and Aluminum I: Analytical Development." *Progress in Astronautics Aeronautic*, vol. 15, pp. 75–115, 1964.

[3] T. A. Brzustowski and I. Glassman, "Vapor-Phase Diffusion Flames in the Combustion of Magnesium and Aluminum I: Experimental Observation in Oxygen Atmosphere." *Progress in Astronautics Aeronautic*, vol. 15, pp. 117–158, 1964.

[4] E. W. Price, "Combustion of Metallized Propellants," *Progress in Astronautics Aeronautic*, vol. 90, pp. 479–513, 1984.

[5] I. Glassman and P. Papas, "Combustion Thermodynamics of Metal-Complex Oxidizer Mixtures," *Journal of Propulsion and Powers*, vol. 15, no. 6, pp. 801–805, 1999.

[6] D. J. Knecht, C. P. Pike, E. Murad, and D. L. A. Rall, "Interaction of Solid-Rocket Exhaust with the Atmosphere," *Journal of Spacecraft and Rockets*, vol. 33, no. 5, pp. 677–685, 1996.

[7] A. Macek and J. M. Semple, "Combustion of Boron Particles at Atmospheric Pressure," *Combustion Science and Technology*, vol. 1, no. 3, pp. 181–191, 1969.

[8] J. Prentice, "Combustion of Pulse-Heated Single Particles of Aluminum and Beryllium," in *Combustion Inst (Western States Sec)-Paper 2 for Spring meeting*, 1969.

[9] L. S. Nelson and H. S. Lvine, "Correlation between Conservation of Metal and Luminosity of a Zirconium Droplet during Free-Fall Combustion in Oxygen," in *Combustion Inst (Western States Sec)-Paper 1 for Spring meeting*, 1969.

[10] E. L. Dreizin, A. V. Suslov, and M. A. Trunov, "Temperature Jumps in Free Metal Particle Combustion," *Combustion Science and Technology*, vol. 87, pp. 45–58, 1993.

[11] E. L. Dreizin, "Experimental Study of Stages in Aluminum Particle Combustion in Air," *Combustion and Flame*, vol. 105, pp. 541–556, 1996.

[12] E. L. Dreizin, "On the Mechanism of Asymmetric Aluminum Particle Combustion," *Combustion and Flame*, vol. 117, pp. 841–850, 1999.

[13] E. L. Dreizin, "Phase Changes in Metal Combustion," *Progress in Energy and Combustion Science*, vol. 26, no. 1, pp. 57–78, Feb. 2000.

[14] A. Rahmel, W. J. Quadakkers, and M. Schuetze, "Fundamental of TiAl Oxidation. Critical Review," *Materials and Corrosion*, vol. 46, no. 5, pp. 271–285, 1995.

[15] Y. V. Levinskiy, *Al–O Phase Diagrams*, in *P-T-X Phase Diagrams of Metal Systems.* Moscow: Metallurgia, 1990.

[16] R. L. Geisler, "A Global View of the Use of Aluminum Fuel in Solid Rocket Motors," in *Proc. 38th AIAA/ASME/SAE/ASEE Joint Propulsion Conference and Exhibit*, 7-10 July 2002.

[17] A. Ingenito and C. Bruno, "Using Aluminum for Space Propulsion," *Journal of Propulsion and Powers*, vol. 20, no. 6, pp. 1056–1063, 2004.

[18] H. Singh, "Current Trend of R&D in the Field of High Energy Materials (HEMs) - An Overview," *Explosion*, vol. 15, no. 3, pp. 120–133, 2005.

[19] L. T. DeLuca, L. Galfetti, F. Severini, L. Meda, G. Marra, A. B. Vorozhtsov, V. S. Sedoi, and V. A. Babuk, "Burning of Nano-Aluminized Composite Rocket Propellants," *Combustion, Explosion, and Shock Waves*, vol. 41, no. 6, pp. 680–692, 2005.

[20] V. A. Babuk, I. N. Dolotkazin, and A. A. Glebov, "Burning Mechanism of Aluminized Solid Rocket Propellants Based on Energetic Binders," *Propellants, Explosives, Pyrotechnics*, vol. 30, no. 4, pp. 281–290, 2005.

[21] A. W. Blackman and D. K. Kuehl, "Use of Binary Light Mixtures and Alloys as Additives for Solid Propellants," *ARS J.*, pp. 1265–1271, 1961.

[22] K. Miyata and N. Kubota, "Combustion of Ti and Zr Particles with KNO_3," *Propellants, Explosives, Pyrotechnics*, vol. 21, no. 1, pp. 29–35, 1996.

[23] I. Lee, R. R. Reed, V. L. Brady, and S. A. Finnegan, "Energy Release in the Reaction of Metal Powders with Fluorine Containing Polymers," vol. 749, pp. 1699–1705, 1997.

[24] T. D. Fedotova, O. G. Glotov, and V. E. Zarko, "Chemical Analysis of Aluminum as a Propellant Ingredient and Determination of Aluminum and Aluminum Nitride in Condensed Combustion Products," *Propellants, Explosives, Pyrotechnics*, vol. 25, no. 6, pp. 325–332, 2000.

[25] G. I. Ksandopulo, O. Y. Isaikina, and A. N. Baidel'dinova, "Combustion of a Mixture of Aluminum and a Titanium-Containing Raw Material in the Presence of Additives," *Combustion, Explosion, and Shock Waves*, vol. 40, no. 3, pp. 295–301, 2004.

[26] A. Gany and L. H. Caveny, "Agglomeration and Ignition Mechanism of Aluminum Particles in Solid Propellants," in *Proc. Symposium (international) on Combustion*, E. L. De Luca, Ed., 1979, pp. 1453–1461.

[27] T. Mitani and M. Izumikawa, "Combustion Efficiencies of Aluminum and Boron in Solid Propellants," *Journal of Spacecraft and Rockets*, vol. 28, no. 1, pp. 79–84, 1991.

[28] V. Rosenband and A. Gany, "A Microscopic and Analytic Study of Aluminum Particles Agglomeration," *Journal of Materials Research*, vol. 166, no. 1, pp. 91–108, 2001.

[29] V. A. Babuk, V. A. Vassiliev, and V. V. Sviridov, "Propellant Formulation Factors and Metal Agglomeration in Combustion of Aluminized Solid Rocket Propellant," *Combustion Science and Technology*, vol. 163, no. 1-6, pp. 261–289, 2001.

[30] O. G. Glotov, V. E. Zarko, V. V. Karasev, T. D. Fedotova, and A. D. Rychkov, "Macrokinetics of Combustion of Monodisperse Agglomerates in the Flame of a Model Solid Propellant," *Combustion, Explosion, and Shock Waves*, vol. 39, no. 5, pp. 552–562, 2003.

[31] S. A. Rashkovsky, "Ultra-Fine Aluminum Behavior in Composite Solid Propellants Combustion," in *Proceedings of the European Combustion Meeting*, 2003.

[32] T. A. Roberts, R. L. Burton, and H. Krier, "Ignition and Combustion of Aluminum/Magnesium Alloy Particles in O_2 at High Pressures," *Combustion and Flame*, vol. 92, no. 1-2, pp. 125–143, Jan. 1993.

[33] Y. L. Shoshin and E. L. Dreizin, "Laminar Lifted Flame Speed Measurements for Aerosols of Metals and Mechanical Alloys," *AIAA Journal*, vol. 42, no. 7, pp. 688–697, 2004.

[34] M. Schoenitz, E. L. Dreizin, and E. Shtessel, "Constant Volume Explosions of Aerosols of Metallic Mechanical Alloys and Powder Blends," *Journal of Propulsion and Power*, vol. 19, no. 3, pp. 405–412, 2003.

[35] Y. L. Shoshin, R. Mudryy, and E. L. Dreizin, "Preparation and Characterization of Energetic Al–Mg Mechanical Alloy Powders," *Combustion and Flame*, vol. 128, no. 3, pp. 259–269, Feb. 2002.

[36] M. Schoenitz and E. L. Dreizin, "Structure and Properties of Al–Mg Mechanical Alloys," *Journal of Materials Research*, vol. 18, no. 8, pp. 1827–1836, Aug. 2003.

[37] E. L. Dreizin, M. Schoenitz, Y. Shoshin, and E. Shtessel, *Metal-Based Metastable Solid Solutions as a New Type of High Energy Density Materials*, in *Rocket Propulsion: Present and Future*, E. L. DeLuca, Ed., 2003.

[38] M. A. Trunov, M. Schoenitz, and E. L. Dreizin, "Ignition of Metastable Metal Based High Energy Density Fuels," in *Proc. 9th Int'l Workshop on Combustion and Propulsion*, Sept. 2003, pp. 36–40.

[39] A. Calka, W. Kaczmarek, and J. S. Williams, "Extended Solid Solubility in Ball-Milled Al-Mg Alloys," *Journal of Materials Science*, vol. 28, no. 1, pp. 15–18, Jan. 1993.

[40] D. L. Zhang, T. B. Massalski, and M. R. Paruchuri, "Formation of Metastable and Equilibrium Phases during Mechanical Alloying of Al and Mg Powders," *Metallurgical and Materials Transactions*, vol. 25A, no. 1, pp. 73–79, Jan. 1994.

[41] C. E. Ellwood, "Factors Affecting Equilibrium in Certain Aluminium Alloys," *Journal of the Institute of Metals*, vol. 80, no. 11, pp. 605–608, 1952.

[42] C. Suryanarayana, "Mechanical Alloy and Milling," *Progress in Materials Science*, vol. 46, pp. 1–184, 2001.

[43] A. Gany and D. W. Netzer, "Fuel Performance Evaluation for the Solid-Fueled Ramjet," *International Journal of Turbo and Jet Engines*, vol. 2, pp. 157–168, 1985.

[44] J. Braun and M. Ellner, "Phase Equilibria Investigations on the Aluminum-Rich Part of the Binary System Ti-Al," *Metallurgical and Materials Transactions*, vol. 32A, no. 5, pp. 1037–1047, May 2001.

[45] A. E. Carlsson and P. J. Meschter, "Relative Stability of $L1_2$, DO_{22}, and DO_{23} structures in MAl_3 compounds," *Journal of Materials Research*, vol. 4, no. 5, pp. 1060–1063, Sept. 1989.

[46] T. Klassen, M. Oehring, and R. Bormann, "Microscopic Mechanisms of Metastable Phase Formation during Ball Milling of Intermetallic TiAl Phases," *Acta Mater.*, vol. 45, no. 9, pp. 3935–3948, Sept. 1997.

[47] F. Zhang, L. Lu, and M. O. Lai, "Study of Thermal Stability of Mechanically Alloyed Ti-75% Al Powders," *J. Alloys and Compounds*, vol. 297, no. 1-2, pp. 211–218, Feb. 2000.

[48] H.-S. Kim, G. H. Kim, and D.-W. Kum, *Formation and Stability of Al_3Ti in the Hyper-Peritectic Al-Ti Alloys After Mechanical Alloying*, in *Design Fundamentals of High Temperature Composites, Intermetallics, and Metal-Ceramics Systems*, (A Collection of Papers from the 1996 TMS Annual Meeting). Feb. 1996, pp. 223–234.

[49] W. Gropp, E. Lusk, and A. Skkjellum, *Powder Diffraction File PDF-2 1998.* Newton Square, PA: JCPDS International Center for Diffraction Data, 1998.

[50] I. Ohnuma, Y. Fujita, H. M. nad K. Ishikawa, R. Kainuma, and K. Ishid, *Al–Ti Phase Diagrams*, in *Desk Handbook: Phase Diagrams for Binary Alloys*, (from Acta Material.). E. H. Okamoto, Ed. Metals Park, OH: ASM International, Nov. 2000, p. 46.

[51] A. Tonejec and A. Bondfacic, "Al-rich Metastable Al–Ti Solid Solutions," *Scripta Metall.*, vol. 3, no. 3, pp. 145–147, March 1969.

[52] G. H. Kim, H.-S. Kim, and D.-W. Kum, "Determination of Titanium Solubility in alpha-Aluminum during High Energy Milling," *Scripta Mater*, vol. 34, no. 3, pp. 421–428, Feb. 1996.

[53] M. Nassik, F. Z. Chrifi-Alaoui, K. Mahdouk, and J. C. Gachon, "Calorimetric Study of the Aluminium-Titanium System," *J. Alloys and Compounds*, vol. 350, pp. 151–154, Feb. 2003.

[54] R. A. Robie, B. S. Hemingway, and J. R. Fisher, *Thermodynamic Properties of Aluminum*, in *Thermodynamic Properties of Minerals and Related Substances at 298.15 K and 1 bar (105 pascals) Pressure and at Higher Temperatures*, Geology Survey Bulletin report number 1452. 1978.

[55] M. Schoenitz and E. L. Dreizin, "Oxidation Processes and Phase Changes in Metastable Al–Mg Alloys," *Journal of Propulsion and Power*, vol. 20, no. 6, pp. 1064–1068, 2004.

[56] M. Schoenitz, X. Zhu, and E. L. Dreizin, "Mechanical Alloys in the Al-rich Part of the Al–Ti Binary System," *Journal of Metastable and Nanocrystalline Materials*, vol. 20-21, pp. 455–461, 2004.

[57] Y. L. Shoshin, M. A. Trunov, X. Zhu, M. Schoenitz, and E. L. Dreizin, "Ignition of Aluminum-rich Al–Ti Mechanicl Alloys in Air," *Combustion and Flame*, vol. 144, no. 4, pp. 688–697, 2006.

[58] T. Nukami and M. C. Flemings, "In Situ Synthesis of TiC Particulate-Reinforced Aluminum Matrix Composites," *Metallurgical and Materials Transactions*, vol. 26A, no. 7, pp. 1877–1884, July 1995.

[59] N. Frage, N. Frumin, L. Levin, M. Polak, and M. P. Dariel, "High-Temperature Phase Equilibria in the Al-Rich Corner of the Al–Ti–C System," *Metallurgical and Materials Transactions*, vol. 29A, no. 4, pp. 1341–1345, April 1998.

[60] A. R. Kennedy, D. P. Weston, M. I. Jones, and C. Enel, "Reaction in Al–Ti–C Powders and Its Relation to the Formation and Stability of TiC in Al at High Temperatures," *Scripta Metallurgica et Materialia*, vol. 42, no. 12, pp. 1187–1192, June 2000.

[61] E. J. Mittemeijer, "Analysis of the Kinetics of Phase Transformations," *Journal of Materials Science*, vol. 27, no. 15, pp. 3977–3987, Aug. 1992.

[62] M. Yamaguchi, Y. Umakoshi, and T. Yamane, "Deformation of the Intermetallic Compound Al_3Ti and Some Alloys with an Al_3Ti Base," in *High-temperature ordered intermetallic alloys II–Mat. Res. Soc. Symp. Proc.*, vol. 81, Dec. 1987, pp. 275–286.

[63] S. Zhang, J. P. Nic, and D. E. Mikkola, "New Cubic Phases Formed by Alloying Al_3Ti with Mn and Cr," *Scripta Metallurgica et Materialia*, vol. 24, no. 1, pp. 57–62, Jan. 1990.

[64] Y. Umakoshi, M. Yamaguchi, T. Sakagami, and T. Yamane, "Oxidation Resistance of Intermetallic Compounds Al_3Ti and TiAl," *Journal of Materials Science*, vol. 24, no. 4, pp. 1599–1603, May 1989.

[65] L. J. Parfitt, J. L. Smialek, J. P. Nic, and D. E. Mikkola, "Oxidation Behavior of Cubic Phases Formed by Alloying Al_3Ti with Cr and Mn," *Scripta Metallurgica et Materialia*, vol. 25, no. 3, pp. 727–731, Apr. 1991.

[66] Y. L. Shoshin and E. L. Dreizin, "Particle Combustion Rates for Mechanically Alloyed Al–Ti and Aluminum Powders Burning in Air," *Combustion and Flame*, available online 9 March 2006(in press).

[67] E. W. Price and R. K. Sigman, *Combustion of Aluminized Solid Propellants*, in *Progress in Astronautics Aeronautic*, T. B. Brill, W.-Z. Ren, and V. Yang, Eds., July 2000, vol. 185, no. 1, p. 663.

[68] N. Claussen, S. Wu, and D. Holz, "Reaction Bonding of Aluminium Oxide(RBAO) composites: Processing, Reaction Mechanisms and Properties," *Journal of the European Ceramic Society*, vol. 14, no. 2, pp. 97–109, Feb. 1994.

[69] S. Lathabai, D. G. Hay, F. Wagner, and N. Claussen, "Reaction-Bonded Mullite/Zirconia Composites," *Journal of the American Ceramic Society*, vol. 79, no. 1, pp. 248–256, Jan. 1996.

[70] N. Birks, G. H. Meier, and F. S. Pettit, "Forming Continuous Alumina Scales to Protect Superalloys," *JOM*, vol. 46, no. 12, pp. 42–46, Dec. 1994.

[71] I. C. I. Okafor and R. G. Reddy, "The Oxidation Behavior of High-Temperature Aluminides," *JOM*, vol. 51, no. 6, pp. 35–39, June 1999.

[72] J. L. Smialek and D. L. Humphrey, "Oxidation Kinetics of Cast $TiAl_3$," *Scripta Metallurgica et Materialia*, vol. 26, no. 11, pp. 1763–1768, June 1992.

[73] R. G. Reddy, X. Wen, and I. C. I. Okafor, "Diffusion of Oxygen in the Al_2O_3 Oxidation Product of $TiAl_3$," *Metallurgical and Materials Transactions A: Physical Metallurgy and Materials Science*, vol. 31A, no. 12, pp. 3023–3028, Dec. 2000.

[74] J. S. Myung, H. J. Lim, and S. G. Kang, "Oxidation Behavior of Nanocrystalline Al Alloys Containing 5 and 10 at.% Ti," *Oxidation of Metals*, vol. 51, no. 1-2, pp. 79–95, Feb. 1999.

[75] M. Schoenitz, X. Zhu, and E. L. Dreizin, "Carbide Formation in Al–Ti Mechanical Alloys," *Scripta Metallurgica et Materialia*, vol. 53, no. 9, pp. 1095–1099, Sept. 2005.

[76] A. C. Larson and R. B. V. Dreele, "General Structure Analysis System," Los Alamos National Laboratory, Tech. Rep. LAUR 86-748, 2000.

[77] Y. S. Kwon, J. S. Moon, A. P. Ilyin, A. A. Gromov, and E. M. Popenko, "Estimation of the Reactivity of Aluminum Superfine Powders for Energetic Applications," *Combustion Science and Technology*, vol. 176, no. 2, pp. 277–288, Feb. 2004.

[78] A. S. Tompa, R. F. Boswell, P. Skahan, and C. Gotzmer, "Low/High Temperature Relationships in Dinitramide Salts by DEA/DSC and Study of Oxidation of Aluminum Powders by DSC/TG," *Journal of Thermal Analysis and Calorimetry*, vol. 49, no. 3, pp. 1161–1170, Aug. 1997.

[79] M. A. Trunov, M. Schoenitz, X. Zhu, and E. L. Dreizin, "Effect of Polymorphic Phase Transformations in Al_2O_3 Film on Oxidation Kinetics of Aluminum Powders," *Combustion and Flame*, vol. 140, no. 4, pp. 310–318, Apr. 2005.

[80] F. Motte, C. Coddet, P. Sarrazin, M. Azzopardi, and J. Besson, "A Comparative Study of the Oxidation with Water Vapor of Pure Titanium and of Ti-6Al-4V," *Oxidation of Metals*, vol. 10, no. 2, pp. 113–126, Apr. 1976.

[81] N. Saunders, "Phase Diagram Calculations for Commercial Al-Alloys," in *Aluminium Alloys (Proc. 5th Int'l Conf. on Aluminium Alloys) – Their Physical and Mechanical Properties (Part 2)*, J. Driver, B. Dubost, F. Durand, R. Fougeres, P. Guyot, P. Sainfort, and M. Suery, Eds., vol. 217-222, Nov. 1996, pp. 667–672.

[82] H. Kissinger, "Variation of Peak Temperature with Heating Rate in Differential Thermal Analysis," *Journal of Research of National. Bureau. Standard*, vol. 57, no. 4, pp. 217–221, Oct. 1956.

[83] W. Gropp, E. Lusk, and A. Skkjellum, *PDF-4/Full File 2003*. Newton Square, PA: JCPDS International Center for Diffraction Data, 2003.

[84] F. Dettenwanger, E. Schumann, M. Ruble, J. Rakowski, and G. H. Meier, "Microstructural Study of Oxidized γ-TiAl," *Oxidation of Metals*, vol. 50, no. 3-4, pp. 269–307, Oct. 1998.

[85] L. Porte, M. Demosthenous, and T. M. Duc, "ESCA Study of the Oxygen–Titanium Interaction," *Journal of the Less Common Metal*, vol. 56, no. 2, pp. 183–191, Dec. 1977.

[86] C. Oviedo, "Oxidation Kinetics of Pure Titanium at Low Pressures," *Journal of Physics: Condens Matter*, vol. 5, no. 33A, p. A153, Aug. 1993.

[87] H. J. Seifert, A. Kussmaul, and F. Aldinger, "Phase Equilibria and Diffusion Paths in the Ti–Al–O–N System," *Journal of Alloys and Compounds*, vol. 317–318, pp. 19–25, Apr. 2001.

[88] L. P. H. Jeurgens, W. G. Sloof, F. D. Tichelaar, and E. J. Mittemeijer, "Thermodynamic Stability of Amorphous Oxide Films on Metals: Application to Aluminum Oxide Films on Aluminum Substrates," *Physical Review B*, vol. 62, no. 7, pp. 4707–4719, Aug. 2000.

[89] X. Zhu, M. Schoenitz, and E. L. Dreizin, "Oxidation Processes and Phase Changes in Metastable Al–Ti Mechanical Alloys," in *Proc. Materials Research Society*, vol. 800, Dec. 2003, pp. AA3.4.1–AA3.4.6.

[90] X. Zhu, M. Schoenitz, and E. L. Dreizin, "Oxidation Behavior of Mechanical Alloyed Al Rich Al–Ti Powders," *Oxidation of Metals*, (under review 2005-2006).

[91] I. Micron Instrument Company. Table of emissivity of various surfaces. [Online]. Available: http://www.transmetra.ch/pdf/publikationen/emissivity.pdf (Accessed on June 2005)

[92] Y. L. Shoshin and E. L. Dreizin, "Production of Well-Controlled Laminar Aerosol Jets and Their Application for Studying Aerosol Combustion Processes," *Aerosol Science and Technology*, vol. 36, no. 9, pp. 953–962, Sept. 2002.

[93] H. W. S. Lauer, Z. Guan and T. H. Wichert, "The Phase Formation at Mechanically Alloyed Ti-Al Compounds," in *Materials Science Forum*, vol. 269, no. 11, 1997, pp. 485–490.

[94] J.-C. Gachon, "Advanced Materials for High Temperature Applications. New Ways of Elaboration," *Pure & Appl. Chem.*, vol. 66, no. 9, pp. 1823–1830, 1994.

[95] S. Ozbilen, "Thermal Analysis of Aged Binary Al-Li Alloys," in *Proc. of Metals and Advanced Materials: Modeling, Design and Properties*, Feb. 1998, pp. 217–224.

[96] W. Davis, *Introduction to Explosives*, in *Explosive Effects and Applications*, Nov. 2002, pp. 1–22.

[97] R. H. Guirguis, "Fragmentation Explosives with Ignition or Initiation Depending on Level of Shock Wave Stimulus," Patent, 2005, u.S. Patent Disclosure (2005), US 6846372 B1 20050125, Application: US 2003-401890 20030331.

[98] R. Ames, "Vented Chamber Calorimetry for Impact-Initiated Energetic Materials," in *Meeting Papers of 43rd AIAA Aerospace Sciences Meeting and Exhibit*, 2005, pp. 15 391–15 403.

[99] B. O'Brien and A. Pradier, "Aluminium-Lithium Alloys: a Review and Assessment," in *Proc. of ESA Symp., ESTEC*, Mar. 1990, pp. 293–300.

[100] V. V. Zakharov, "Some Problems of the Use of Aluminum–Lithium Alloys," *Metal Science and Heat Treatment*, vol. 45, no. 1-2, pp. 49–54, Jan. 2003.

[101] P. S. Gilman, J. Brooks, and P. J. Bridges, *High Temperature Tensile Properties of Mechanically Alloyed Al–Mg–Li Alloys*, in *Aluminum-Lithium Alloys (III)*, C. Baker, P. J. Gregson, S. J. Harris, and C. J. Peel, Eds., Mar., pp. 112–120.

[102] W. Ruch and E. A. S. Jr., *Fatigue Crack Propagation in Mechanically Alloyed Al–Mg–Li Alloys*, in *Aluminum-Lithium Alloys (III)*, C. Baker, P. J. Gregson, S. J. Harris, and C. J. Peel, Eds., Mar., pp. 121–130.

[103] W. T. Tack and D. K. McNamara, "Liquid Oxygen Compatibility of Aluminium-Lithium Alloys Using the Impact Sensitivity Test Method," in *Proc. 6th Int'l Aluminum–Lithium Conf.*, 1992, pp. 403–408.

[104] J. T. Moore, S. R. Turns, and R. A. Yetter, "Combustion of Lithium-Aluminum Alloys," *Combustion Science and Technology*, vol. 177, no. 4, pp. 627–669, Apr. 2005.

[105] A. J. McAlister, *Al–Li Phase Diagrams*, in *Desk Handbook: Phase Diagrams for Binary Alloys*, (from Bull. Alloy Phase Diagrams). E. H. Okamoto, Ed. Metals Park, OH: ASM International, Nov. 2000, p. 35.

[106] H. J. Axon and W. Hume-Rothery, "The Lattice Spacings of Solid Solutions of Different Elements in Aluminium," *Proc. of the Royal Society of London. Series A, Mathematical and Physical Sciences*, vol. 193, no. 1032, pp. 1–24, Apr. 1948.

[107] E. D. Levine and E. J. Rapperport, "A Study of the Aluminum-Lithium System between Aluminum and Al-Li," *Trans. Metall. Soc. AIME*, vol. 227, pp. 1204–1208, Oct. 1963.

[108] S. H. Kellington, D. Loveridge, and J. M. Titman, "The Lattice Parameters of the Aluminum–Lithium," *Brit. J. Appl. Phys. (J. Phys. D)*, vol. 2, pp. 1162–1163, 1969.

[109] R. Podloucky, H. J. F. Jansen, X. Q. Guo, and A. J. Freeman, "First-Principles Electronic-Structure Approach for Phase Diagrams of Binary Alloys," *Physical Review B*, vol. 37, no. 10, pp. 5478–5482, Apr. 1988.

[110] S. Abis, R. Caciuffo, F. Carsughi, R. Coppola, M. Magnani, F. Rustichelli, and M. Stefanon, "Late Stages of δ' Precipitation in an Al–Li Alloy by Small–Angle Neutron Scattering," *Physical Review B*, vol. 42, no. 4, pp. 2275–2281, Aug. 1990.

[111] G. L. Shneider, "Stability of Supersaturated Solid Solution of Aluminum–Lithium Alloy 1470," *Metal Science and Heat Treatment*, vol. 40, no. 1-2, pp. 27–33, July 1998.

[112] J. M. Papazian, *Different Scanning Calorimetry for Precipitate Characterization in Aluminum–Lithium Alloys*, in *Thermal Analysis in Metallurgy*, R. D. Shull and A. Joshi, Eds., 1992, pp. 259–278.

[113] K. Brooks and M. Beckstead, "Dynamics of Aluminum Combustion." *Journal of Propulsion and Powers*, vol. 11, no. 4, pp. 769–780, 1995.

[114] B. L. Bobryshev and Y. P. Aleksandrova, "Ignition of Magnesium and its Alloys," *Metal Science and Heat Treatment*, vol. 30, no. 3, pp. 219–222, 1988.

[115] T. A. Steinberg, D. B. Wilson, and F. Benz, "The Burning of Metals and Alloys in Microgravity," *Combustion and Flame*, vol. 33, no. 2, pp. 309–320, 1992.

[116] T. S. Shih, J. H. Wang, and K. Z. Chong, "Combustion of Magnesium Alloys in Air," *Materials Chemistry and Physics*, vol. 85, no. 2–3, pp. 302–309, 2004.

[117] M. A. Trunov, M. Schoenitz, and E. L. Dreizin, "Ignition of Aluminum Powders under Different Experimental Conditions," *Propellants, Explosives and Pyrotechnics.*

[118] M. Klanchar, B. D. Wintrode, and J. A. Phillips, "Lithium-Water Reaction Chemistry at Elevated Temperature," *Energy & Fuels*, vol. 11, pp. 931–935, 1997.

[119] W. M. Lee and R. D. Ford, "Reactivity of Al-2.5 pct Li Alloy with Water as Studied by the Exploding Wire Technique," *Metallurgical Transactions B*, vol. 19B, pp. 255–259, 1988.

[120] D. J. Bottomley, H. M. van Driel, and R. S.Timsit, "Structural Transformations in Thin Oxide Layers on the (211) Surface of an Aluminum - Lithium Alloy," *Journal of Vacuum Science & Technology, A: Vacuum, Surfaces, and Films*, vol. 11, no. 4, Pt. 2, pp. 2193–2199, Dec. 1993.

[121] K. K. Soni, *Characterization of Surface Oxides on Aluminum - Lithium Alloys*, in *Microstructural Science, 19(Structure-Property Relationships and Correlations with the Environmental Degradation of Engineering Materials)*, 1992, pp. 535–551.

[122] D. Fink, V. Hnatowicz, J. Kvitek, V. Havranek, and J. T. Zhou, "External Oxidation of Aluminum - Lithium Alloys," *Surface and Coatings Technology*, vol. 51, no. 1-3, pp. 57–64, 1992.

[123] H. P. Klug and L. Alexander, *Formation and Stability of Al_3Ti in the Hyper-Peritectic Al-Ti Alloys After Mechanical Alloying*, in *X-ray Diffraction*

Procedures for Ploycrystalline and Amorphous Materials, (A Collection of Papers from the 1996 TMS Annual Meeting). New York: John Wiley and Sons, 1974, p. 661.

[124] S. K. Pradhan, T. Chakraborty, S. P. S. Gupta, C. Suryanarayana, A. Frefer, and F. H. Froes, "X-Ray Powder Profile Analyses on Nanostructured Niobium Metal Powders," *Nanostructured Materials*, vol. 5, no. 1, pp. 53–61, 1995.

[125] R. A. Varin, D. Wexler, A. Calka, and L. Zbroniec, "Formation of Nanocrystalline Cubic ($L1_2$) Titanium Trialuminide by Controlled Ball Milling," *Intermetallics*, vol. 6, pp. 547–557, 1998.

[126] M. H. F. Sluiter, Y. Watanabe, D. de Fontaine, and Y. Kawazoe, "First-Principles Calculation of the Pressure Dependence of Phase Equilibria in the Al–Li System," *Physical Review B*, vol. 53, no. 10, pp. 6137–6151, 1996.

[127] K. K. Soni, D. B. Williams, J. M. Chabala, R. Levi-Setti, and D. E. Newbury, "Morphological and Microchemical Phenomena in the High-Temperature Oxidation of Binary Al–Li Alloys," *Oxidation of Metals*, vol. 36, pp. 361–378, 1991.

[128] P. G. Partridge, "Oxidation of Aluminium–Lithium Alloys in the Solid and Liquid States," *Int. Mater. Rev.*, vol. 35, no. 1, pp. 37–58, 1990.

[129] D. J. Field, G. M. Scamans, and E. P. Butler, "The High Temperature Oxidation of Al–Li Aalloys," in *Aluminum-Lithium Alloys II; Proceedings of the Second International Aluminum–Lithium Conference*, 12-14 Apr. 1983, pp. 657–666.

[130] V. I. Cheburkov and A. N. Rozanov, "Reaction Kinetics of Molten Lithium with Oxygen and Nitrogen," *Metallurgiya i Metallovedenie Chistykh Metallov (in Russian)*, vol. 7, pp. 168–173, 1968.

[131] R. W. Chung, J. M. H. Foen, and S. W. deLeeuw, "Ion Transport in Nanocrystalline Materials: a Computer Simulation Study," *Journal of Electroanalytical Chemistry*, vol. 584, no. 1, pp. 44–53, 2005.

[132] M. Wilkening, S. Indris, and P. Heitjans, "Heterogeneous Lithium Diffusion in Nanocrystalline $Li_2O : Al_2O_3$ Composites," *Physical Chemistry Chemical Physics*, vol. 5, no. 11, pp. 2225–2231, 2003.

[133] T. Nabatame, T. Yasuda, M. Nishizawa, M. Ikeda, T. Horikawa, and A. Toriumi, "Comparative Studies on Oxygen Diffusion Coefficients for Amorphous and $\gamma-Al_2O_3$ Films Using 18o Isotope," *Japanese Journal of Applied Physics, Part 1: Regular Papers, Short Notes & Review Papers*, vol. 42, no. 12, pp. 7205–7208, 2003.

[134] A. F. Beck, M. A. Heine, E. J. Caule, and M. J. Pryor, "Kinetics of the Oxidation of Al in Oxygen at High Temperature," *Corrosion Science*, vol. 7, no. 1, pp. 1–22, 1967.